Thèse

Présentée et soutenue publiquement pour l'obtention du grade de

Docteur de l'Université de Lorraine

Mention : Science des Matériaux

présentée par

Frederic HABIYAREMYE

Mechanisms of plastic deformation near grain boundaries in CrCoNi medium entropy alloy

Soutenue le 08 Mars 2022 devant le jury composé de :

Rapporteur	Prof. Anna FRACZKIEWICZ	Ecoles de Mines de St-Etienne, France
Rapporteur	Prof. Christian MOTZ	Universät des saarlandes, Germany
Examinateur	Dr. Stéphane BERBENNI	Université de Lorraine, France
Examinateur	Prof. Jean-Philippe COUZINIÉ	Université Paris Est, France
Examinateur	Dr. Guillaume LAPLANCHE	Ruhr-Universität Bochum, Germany
Directeur	Dr. Nabila MALOUFI	Université de Lorraine, France
Co-directeur	Dr. Antoine GUITTON	Université de Lorraine, France

Président du Jury : Dr. Stéphane BERBENNI

LEM3 UMR 7239 CNRS, 7 Rue Felix Savart, 57070 Metz, France

Thesis

Presented and publicly defended to obtain the degree of

Ph.D. of « Université de Lorraine »

Mention: Materials Science

presented by

Frederic HABIYAREMYE

Mechanisms of plastic deformation near grain boundaries in CrCoNi medium entropy

Defended on March 08th, 2022, in front of the jury composed of:

Reviewer	Prof. Anna FRACZKIEWICZ	Ecoles de Mines de St-Etienne, France
Reviewer	Prof. Christian MOTZ	Universät des Saarlandes, Germany
Examiner	Dr. Stéphane BERBENNI	Université de Lorraine, France
Examiner	Prof. Jean-Philippe COUZINIÉ	Université Paris Est, France
Examiner	Dr. Guillaume LAPLANCHE	Ruhr-Universität Bochum, Germany
Director	Dr. Nabila MALOUFI	Université de Lorraine, France
Co-director	Dr. Antoine GUITTON	Université de Lorraine, France

President of the Jury : Dr. Stéphane BERBENNI

LEM3 UMR 7239 CNRS, 7 Rue Felix Savart, 57070 Metz, France

“First-principles is a physical way of looking at the world. You boil things down to the most fundamental truths and then reason up from there”

Elon Musk

Acknowledgments

This thesis was carried out at LEM3 (Laboratoire d'Études des Microstructures et de Mécanique des Matériaux) of C2MP doctoral school of "Université de Lorraine". Thus, I would like to thank Pr. Daya El Mostafa, the director of LEM3, Pr. Dominique Daloz, the director of C2MP, and Pr. Pierre Mutzenhardt, the president of the "Universite de Lorraine" for allowing me to do my thesis in this prestigious institution. I would like also to thank « Ministère français de l'Education nationale et de l'enseignement supérieur et de la Recherche » for financing my thesis's project.

I would especially like to thank my thesis directors Nabila Maloufi and Antoine Guitton who have given me tremendous scientific, technical, and personal support over the last three years. I am thankful for the opportunity they gave me to pursue my Ph.D. degree at the Université de Lorraine. The fruitful discussions around numerous meetings and presentations were essential for the realization of this manuscript. I would like to thank Pr. Sidi Hamady and Dr. Vincent Taupin, who were members of the monitoring committee "Comité de Suivi" for their annual feedback and encouragement.

I want to thank Prof. Christian Motz and Prof. Anna Fraczkiewicz for the honor of being reviewers for my thesis. I would like also to thank Dr. Stéphane Berbenni, Dr. Jean-Philippe Couzinié, and Dr. Guillaume Laplanche for the honor of being the examiners for my thesis.

I want to thank the various research groups in LEM3 that have provided technical and scientific support that made writing this manuscript possible. There are members of the LEM3's experimental platform Julien Guyon, Jérôme Slowensky, Auriane Mandrelli, and Jean Sebastien Lecomte. I would like to thank Julien Guenolé for his support on atomistic simulations and the team of Xiaolei Chen, Thiebaud Richeton, and Stéphane Berbenni for their support on numerical calculations. I am also thankful to Florian Schäfer in the Department of Materials Science and Engineering, Saarland University (Germany), for his help with instrumented nanoindentation coupled with an atomic force microscope.

I want to thank my colleagues, Ph.D. students with whom we share frustrations and struggles caused by the Covid-19 pandemic. I am grateful for the many professional and personal discussions and continued encouragement. Among them, there are Thomas Martinez, Layal, Mediateur, Oscar, etc. I cannot forget the technical support provided by postdoctoral fellows,

Kaustubh, Hana, and Mariem, to whom I have asked questions and answered them with pleasure.

I would like to thank the administrative team in LEM3 who have been there for all the administration procedures: Laura, Aurore, Elvire, and others.

I want to thank my family, to which I am indebted. You are always there for every stage of my journey. I am also grateful to all my friends for their support and encouragement.

Table of contents

List of abbreviations and symbols

A	Area of an electron channeling contrast micrograph
A_c	Contact area at the peak load
A-ECCI	Accurate electron channeling contrast imaging
A_{TB}	Area of the twin boundary
ATOMSK	Atom, Molecule, and Material Software Kit
b	Burgers vector
$\mathbf{b_i}$	Burgers vector of the incoming dislocation
$\mathbf{b_o}$	Burgers vector of the outgoing dislocation
BCC	Body-centered cubic
$\mathbf{b_r}$	Residual burgers vector
BSE	Backscattering electrons
CJ	Conjugate gradient
CNA	Common neighbor analysis
CRSS	Critical resolved shear stress
CSL	Coincidence site lattice
CTB	Coherent twin boundary
D	Dislocation spacing
d_α^A	Orientation of the slip direction in grain A
d_β^B	Orientation of the slip direction in grain B
D_k	Search direction
DXA	Dislocation Extraction Algorithm
EAM	Embedded Atom Method
EBSD	Electron backscatter diffraction
E_c	Energy of a dislocation core
E_{coh}	Cohesive energy
ECP	Electron channeling pattern
EDS	Energy dispersive x-ray spectroscopy
E_e	Energy of a dislocation
E_i	Young's modulus of the nanoindenter

E_r	Reduced modulus
E_s	Young's modulus of the sample
E_{stop}	Energy stopping criterion
E_T	Total energy
E_{TB}	Energy of the twin boundary
F_α	Embedding energy
FCC	Face-centered cubic
FEM	Finite element method
FIB	Focused ion beam
G	Shear modulus
g	Diffraction vector
H_2O_2	Hydrogen peroxide
HAGB	High angle grain boundary
h_c	Depth of contact
HCP	Hexagonal closed packed
HEA	High entropy alloy
HetND	Heterogeneous nucleation of dislocation
HomND	Homogeneous nucleation of dislocation
h_p	Depth at the initial pop-in
HR-SACP	High resolution-channeling selected area channeling pattern
ITB	Incoherent twin boundary
L^{-1}	Mean free path
L	Length of dislocations in a given volume
LAGB	Low angle grain boundary
LAMMPS	Large-scale Atomic/Molecular Massively Parallel Simulator
MD	Molecular dynamics
MEA	Medium entropy alloy
N	N-factor
n_α^A	Orientation of the slip plane normal in grain A
n_β^B	Orientation of the slip plane normal in grain B
n_p	Number of dislocations in the pile-up
N_{hkl}	Number of induced dislocations emitted below the nanoindenter linked in grain with hkl orientation

n_i	Major element
NID	Nanoindentation induced dislocation
n_j	Minor element
PED	Pre-existing dislocation
P-h	Load-displacement curve
P_{max}	Peak load during nanoindentation
Pp	Load at the initial pop-in
R	Fault vector
$\dot{\mathbf{r}}(t)$	Atomic velocity
$\ddot{\mathbf{r}}(t)$	Atomic acceleration
$\mathbf{r}(t)$	Atomic position
r_0	Dislocation core radius
r_c	Critical dislocation loop radius
R_d	Ratio between the distance to the LAGB and the nanoindent size
Rg	Perfect gas constant
R	Radius of the nanoindenter
r_{ij}	Distance between i and j
R_k	System configuration at iteration k
S	Stiffness
SACP	Selected area channeling pattern
SE	Secondary electron
SEM	Scanning electron microscope
SFE	Stacking fault energy
SiC	Silicon carbide
STEM-EDS	Scanning transmission electron microscope-energy dispersive x-ray spectroscopy
TB	Twin boundary
TD	Threading dislocation
TEM	Transmission electron microscope
X_i	Atomic weight percentage of the major element
X_j	Atomic weight percentage of the minor element
XRD	X-ray diffraction
XRF	X-ray fluorescence

α_k	Step size
β	Constant that expresses non-axisymmetry of the nanoindenter
γ_{GB}	Energy of a grain boundary
Δh_{hkl}	Projection of the pop-in width along with the slip system
Δh_p	Width of the initial pop-in
ΔS_{conf}	Configuration entropy
Δt	Timestep
θ	Misorientation angle in degrees
ρ	Global dislocation density
ρ_{loc}	Local dislocation density
ρ_α	Local electron density
τ_e	Applied shear stress contributing to the dislocation pile-up
τ_c	Critical shear stress
τ_α^A	Shear stress at the head of the accumulated dislocations in their slip plane
τ_β^B	Shear acting on the incoming slip system
τ_{th}	Theoretical shear stress
ν	Poisson's ratio
ν_i	Poisson's ratio of the nanoindenter
ν_s	Poisson's ratio of the sample
$\phi_{\alpha\beta}$	Pair potential between element type α and β

General introduction

This thesis was mainly carried out at LEM3 (Laboratoire d'Etude des microstructures et de Mécanique des matériaux) of the Université de Lorraine, CNRS, Arts et Métiers (Metz, France). Some of the experiments of nanoindentation have been conducted at the University of Saarbrucken (Germany). The monocrystalline and polycrystalline samples of a CrCoNi medium entropy alloy (MEA) were provided by Guyaume Laplanche and his colleagues from the University of Bochum, Germany.

The interactions between dislocations and various defects are essential in plastic deformation and are responsible for superior mechanical properties of metallic materials [1]–[6]. The interactions between dislocations and grain boundaries (GB), among other interactions, have a significant influence on yield strength, as evidenced by the Hall-Petch relationship [7]–[14]. Although the latter is effective for quantifying two microstructures with different grain sizes, it assumes that all grain boundaries are of the same type and have the same strength, which is not the case in polycrystalline materials. For example, diverse hardening effects have been observed for different GBs in deformed aluminium [15]. Moreover, some special GBs provide additional properties. For example, maximizing annealing twins, which are special boundaries with low index planes, has been used to improve resistance to various forms of intergranular degradation such as corrosion, cracking, or embrittlement [16], [17].

The CrCoNi MEA is a promising alloy for room and cryogenic applications because it has outstanding mechanical properties superior to most high entropy alloys (HEAs) and conventional alloys. The origins of these mechanical properties have been well documented in the literature. They were initially associated with solid solution strengthening [18]. However, the CrCoNi MEA exhibits higher mechanical properties (yield stress of 560±10 MPa, ultimate tensile strength of 1230 MPa, ductility of ~45% at 77 K [19]) than CrMnFeCoNi HEA (yield stress of 460±30 MPa, ultimate tensile strength of 1060±70 MPa, ductility of ~67% at 77 K [20]), which contradicts such correlation. It was found that low stacking fault energy (SFE) of $22 \pm 4\,\mathrm{mJ \cdot m^{-2}}$ [19] is one of the main factors responsible for outstanding mechanical properties. The low SFE favors the formation of mechanical twins, which are coherent interfaces that block the motion of dislocations (dynamic Hall-Petch effect). Moreover, the CrCoNi MEA exhibits a high Hall-Petch strengthening with a Hall-Petch slope of $600\,\mathrm{MPa \cdot \mu m^{-1/2}}$[21]. Schneider *et al.* [21] also revealed annealing TBs contribute as much as the general GBs. Therefore, understanding of interactions between dislocations and different microstructural features such as other dislocations and GBs is fundamental for

understanding the reasons for the outstanding mechanical properties of the CrCoNi MEA. Moreover, such information would help design high-performance CrCoNi alloy and can be interpolated in the design of other structural engineering alloys.

Deformation was conducted by instrumented nanoindentation and microstructure was obtained using electron channeling contrast imaging (ECCI). On one hand, nanoindentation was used because it offers incontestable abilities to probe the mechanical response at specific locations of the sample from very small volumes of materials [22]. On the other hand, the ECCI technique to obtain micrographs and characterize defects on a bulk sample inside a scanning electron microscope (SEM) [23]–[27]. Moreover, mechanisms of plastic deformation have been investigated using atomistic simulations. The combination of the experiment and atomistic simulations allows us to answer two fundamental questions:

- How do dislocations nucleate during mechanical testing in the CrCoNi MEA?
- How do these dislocations interact with different GBs (assessment of the micromechanical behavior of the GBs) in the CrCoNi MEA?

This thesis has been organized into five chapters:

- **Chapter 1** discusses the fundamentals of plastic deformation of face-centered cubic (FCC) materials and CrCoNi MEA in particular. It also explores the mechanisms of dislocation-GB interactions in both FCC materials and CrCoNi MEA.
- **Chapter 2** looks at the techniques employed in this thesis. These include imaging and characterization techniques such as electron backscatter diffraction (EBSD), ECCI, energy dispersive x-rays (EDS), and so forth. It also looks at instrumented nanoindentation used for localized plastic deformation. Furthermore, it also briefly describe atomistic simulations performed using molecular dynamics.
- **Chapter 3** examines the origin and mechanisms of plastic deformation in the monocrystalline CrCoNi MEA and how various configurations of dislocations affect them.
- **Chapter 4** investigates the dislocation-LAGB interactions and associated micromechanical responses in the monocrystalline CrCoNi MEA.
- **Chapter 5** studies dislocation-TB interactions using microstructural analysis and atomistic simulations in the polycrystalline CrCoNi MEA.

Introduction générale

Cette thèse a été principalement réalisée au LEM3 de l'Université de Lorraine, CNRS, Arts et Métiers (Metz, France). Néanmoins, certaines expériences ont été réalisées à l'Université de Saarbrücken (Allemagne).

Les interactions des dislocations avec différents défauts sont essentielles dans la déformation plastique et sont responsables des propriétés mécaniques supérieures des matériaux [1]-[6]. Les interactions entre les dislocations et les joints de grain, entre autres, ont une influence significative sur la limite d'élasticité, comme en fait preuve la relation Hall-Petch [7]-[14]. Bien que cette dernière soit efficace pour quantifier deux microstructures avec des tailles de grains différentes, elle suppose que tous les joints de grains sont du même type et ont la même résistance, ce qui n'est pas le cas dans les matériaux polycristallins. Par exemple, divers effets de durcissement ont été observés sur différents joints de grain dans l'aluminium déformé [15]. En outre, certains joints de grain spéciaux offrent des propriétés supplémentaires. Par exemple, la maximisation des macles, qui sont des joints spéciaux avec des plans à faible indice, a été utilisée pour améliorer la résistance à diverses formes de dégradation intergranulaire telles que la corrosion, la fissuration ou la fragilisation [16], [17].

L'alliage à entropie moyenne de CrCoNi est un alliage prometteur pour les applications à température ambiante et cryogénique car il présente des propriétés mécaniques exceptionnelles, supérieures à celles de la plupart des alliages à haute entropie et des alliages classiques. Les origines des propriétés mécaniques ont été bien documentées dans la littérature. Ils ont été initialement associées au renforcement de la solution solide [18]. Cependant, le CrCoNi à moyenne entropie présente des propriétés mécaniques plus élevées (limite d'élasticité de 560±10 MPa, résistance ultime de 1230 MPa, ductilité de ~45% à 77 K [19]) que le l'alliage à haute entropie de CrMnFeCoNi (limite d'élasticité de 460±30 MPa, résistance à la traction ultime de 1060±70 MPa, ductilité de ~67% à 77 K [20]), ce qui contredit cette corrélation. Il a été constaté que la faible énergie de défaut d'empilement de 22 ± 4 $mJ \cdot m^{-2}$[19] est l'un des principaux facteurs responsables des propriétés mécaniques exceptionnelles. La faible énergie de faute d'empilement favorise la formation des macles qui sont des interfaces cohérentes qui bloquent le mouvement des dislocations (effet Hall-Petch dynamique). De plus, l'alliage de CrCoNi présente un fort renfort Hall-Petch avec une pente Hall-Petch de 600 $MPa \cdot \mu m^{-1/2}$[21]. Schneider *et al.* [21] ont également révélé que les macles contribuent autant que les autres joints de grain. Par conséquent, la compréhension des interactions des dislocations avec différentes

caractéristiques microstructurelles telles que les autres dislocations et les joints de grain est fondamentale pour comprendre les raisons des propriétés mécaniques exceptionnelles de l'alliage à moyenne entropie de CrCoNi. De plus, de telles informations faciliteraient la conception d'un alliage CrCoNi à haute performance et porraient être interpolées dans la conception d'autres alliages d'ingénierie structurelle.

La déformation a été effectuée par la nanoindentation instrumentée et la microstructure a été obtenue en utilisant contraste de canalisation d'éléctrons. D'une part, la nanoindentation a été utilisée car elle offre des capacités incontestables pour sonder la réponse mécanique à des endroits spécifiques de l'échantillon à partir de très petits volumes de matériaux [22]. En revanche, le permet d'obtenir des micrographies et de caractériser les défauts sur un échantillon massif dans un microscope électronique à balayage [23]-[27]. En outre, des simulations atomiques ont permis d'étudier les mécanismes spécifiques de déformation plastique. La combinaison de l'expérience avec les simulations atomistiques nous permet de répondre à deux questions fondamentales :

- Comment les dislocations se nucléent-elles pendant les essais mécaniques dans l'alliage à moyenne entropie de CrCoNi ?
- Comment ces dislocations interagissent elles avec les différents joints de grain (évaluation du comportement micromécanique des joints de grain) dans l'alliage à moyenne entropie CrCoNi ?

Cette thèse a été organisée en cinq chapitres :

- Le chapitre 1 aborde les principes fondamentaux de la déformation plastique des matériaux cubiques à faces centrées et de l'alliage à moyenne entropie de CrCoNi en particulier. Il explore également les mécanismes des interactions des dislocations et les joints de grain dans les matériaux cubiques à faces centrées et dans l'alliage à moyenne entropie de CrCoNi.
- Le chapitre 2 présente les techniques utilisées dans cette thèse. Celles-ci comprennent des techniques d'imagerie et de caractérisation telles que la diffraction des électrons rétrodiffusés (EBSD), l'ECCI, les rayons X à dispersion d'énergie (EDS), et ainsi de suite. Il examine également la nanoindentation instrumentée utilisée pour la déformation plastique localisée. En outre, il décrit brièvement les simulations atomistiques réalisées à l'aide de la dynamique moléculaire.

- Le chapitre 3 examine l'origine et les mécanismes de la déformation plastique dans l'alliage monocristallin de CrCoNi et la façon dont diverses configurations de dislocations les affectent.
- Le chapitre 4 étudie les interactions des dislocations et le joint de grain à faible désorientation et les réponses micromécaniques associées dans l'alliage monocristallin de CrCoNi.
- Le chapitre 5 étudie les interactions des dislocations et le macle à l'aide d'une analyse microstructurale et de simulations atomiques dans l'alliage polycristallin de CrCoNi.

1. State the art: Fundamentals of plastic deformation in FCC materials and CrCoNi medium entropy alloy

Abstract

Plastic deformation in metallic materials is believed to proceed by nucleating dislocations, followed by the motion of the newly nucleated and pre-existing dislocations, and their interactions with different defects, e.g., vacancies, other dislocations, GBs, and precipitates. Additionally, it may also occur via mechanical twinning, which produces twins providing extra GBs. Among the above interactions, dislocation-GB interactions are crucial because GBs are obstacles to dislocation movement, thus providing the strength of materials. For example, grain refinement through thermomechanical processing relies on GBs to enhance the strength of metals and alloys. This enhancement occurs thanks due to the interactions between dislocations and GBs. Dislocations can be blocked by the GB, can be absorbed in the GB, transmitted across the GB, or reflected into the original grain. These interactions are depended upon the character of the dislocation and the properties of GB.

The CrCoNi medium entropy alloy is a ternary derivative of the CrCoFeNiMn high entropy alloy with a single face-centered cubic (FCC) phase, low stacking fault energy (SFE), and high shear modulus. The low SFE promotes the formation of twins. Thus, strengthening from a combination of GBs and TBs is responsible for a higher Hall-Petch slope exceeding 600 $MPa \cdot \mu m^{-1/2}$. Therefore, it is essential to understand the underlying mechanisms of dislocation-grain boundary interactions in order to better evaluate the contribution of each GB to the overall strength of this CrCoNi alloy.

Résumé

On pense que la déformation plastique dans les matériaux métalliques se déroule par la nucléation de dislocations, suivie du mouvement des dislocations nouvellement nucléées et préexistantes, et de leurs interactions avec différents défauts, par exemple, des lacunes, d'autres dislocations, des joints de grais et des précipités. En outre, il peut également se produire par le maclage mécanique, qui produit des macles fournissant des joints de grain supplémentaires. Parmi les interactions susmentionnées, les intéractions entre les dislocations et les joints de grain sont essentiels, car les joints de grains empêchent le mouvement des dislocations, ce qui procure la résistance mécanique des matériaux. Par exemple, le raffinage des grains par des traitements thermomécaniques repose sur les joints de grain pour améliorer la résistance des métaux et des alliages. Cette amélioration est attribuable aux interactions entre les dislocations et les joints de grains. Les dislocations peuvent être bloquées par le joints de grain, absorbées dans le joint de grain , transmises à travers le joint de grain ou réfléchies dans le grain d'origine. Ces interactions sont liées au caractère de la dislocation et aux propriétés des joints de grain.

L'alliage à entropie moyenne CrCoNi est un dérivé ternaire de l'alliage à entropie élevée CrCoFeNiMn avec une seule phase cubique à faces centrée, une faible énergie de défaut d'empilement et un module de cisaillement élevé. La faible énergie d'empilement favorise la formation des macles. Ainsi, le renfort provenant d'une combinaison de joints de grain et des macles est responsable d'une pente Hall-Petch plus élevée dépassant 600 $MPa \cdot m^{-1/2}$. Par conséquent, il est essentiel de comprendre les mécanismes fondamentaux des interactions dislocation et les joints de grains afin de mieux évaluer leur contribution à la résistance globale de cet alliage CrCoNi.

1.1. Introduction

Dislocations are central in plastic deformation of crystalline materials [28], [29]. They are differently introduced and can move by various mechanisms while interacting with defects such as vacancies [30]–[32], other dislocations [3], stacking faults [33], [34], GBs [2], [13], [14], [35], precipitates [36]–[38], and so forth. Among these interactions, the dislocation-GB interaction has a significant influence on the strength of materials [8], [39]–[41]. It has also been found to be particularly effective in CrCoNi MEA with a Hall-Petch slope greater than 600 $MPa \cdot \mu m^{-0.5}$ [21], [42]. However, the Hall-Petch relation assumes that all GBs are of the same types and respond equally to incoming dislocations, which is not true in polycrystalline materials as revealed by Vachhan *et al.* [15] who observed different hardening effects for different GB in 20% deformed aluminum. Moreover, Schneider *et al.* [21] suggested that annealing TBs contribute as much as general GBs in the strengthening of the CrCoNi MEA. Therefore, understanding interactions of dislocations with individual GB is the first step to obtaining the strength of individual GB.

1.2. Fundamentals of dislocations in FCC materials

The concept of dislocation was proposed to explain the discrepancy between theoretical and experimental values of the applied resolved shear stress necessary to initiate plastic deformation in single crystals. This discrepancy was huge since Frenkel's calculated values were around G/30, where G is the shear modulus, which was far greater than the experimental values in the range 10^{-4} to 10^{-8} G in well-annealed crystals [29]. Dislocation is a linear defect that is geometrically defined by a Burgers vector (**b**) and a line direction (**u**). The **b** is obtained using the Burgers circuit depicted in Fig. 1.1. For a crystal containing a dislocation, the Burgers circuit forms a closed loop as depicted in Fig. 1.1a. If the same Burgers circuit is applied to a perfect crystal, a closure failure is **b** as depicted in Fig. 1.1b. The line sense is positive because Fig. 1.1 is based on a right-hand/finish-start convention [29].

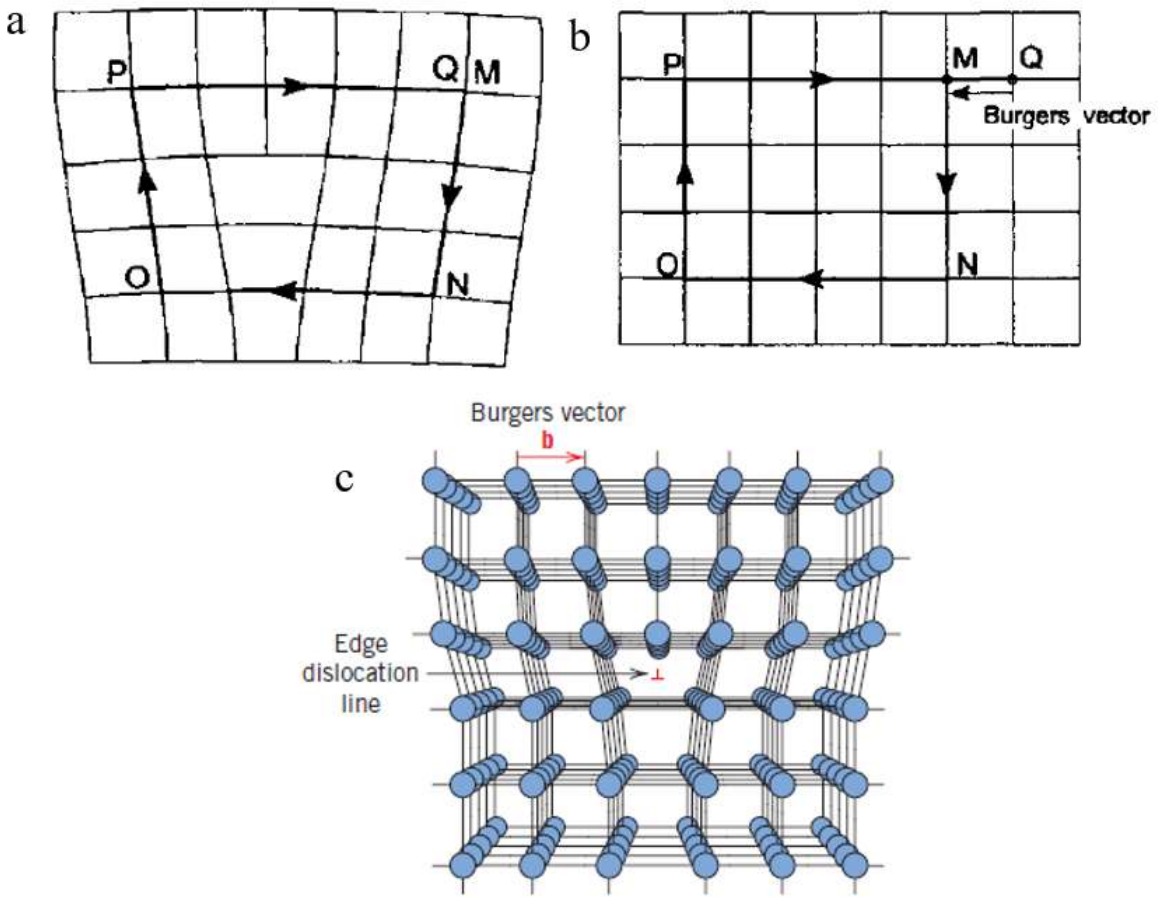

Fig. 1.1. (a) Burgers circuit around a dislocation with positive line sense into the paper, (b) the same Burgers circuit in a perfect crystal (the closure failure is the Burgers vector, **b**) [29], (c) the positions of the atom around an edge dislocation; a supplementary half-plane of atoms is shown in perspective.

The dislocation line, **u**, is the boundary between slipped and unslipped regions of a crystal. Consequently, dislocation cannot end inside a crystal. It must form a closed elliptical or prismatic loop, branch into other dislocations, or end at the free surface, disclinations, and grain boundaries [28].

Based on **b** and **u**, there are three types of dislocations: edge, screw, and mixed dislocations. An edge dislocation has **b** normal to **u**. Fig. 1.1c depicts an extra portion of a plane, whose edge ends within the crystal [43]. The magnitude of the Burgers vector is equal to the atomic spacing and the line sense direction is shown by the red arrow. The unit vector of the direction line, **u,** is perpendicular to the plane of the page. A screw dislocation has **b** parallel to **u.** The edge and screw dislocations represent the extreme cases. Thus, there is a mixed dislocation, *i.e.*, dislocation with edge and screw characters. The vector **b** of mixed dislocations does not change

along the dislocation line even if the character change from edge to screw character. The magnitude of a mixed dislocation depends on the angle between **b** and **u** [29].

1.2.1. Dislocations in FCC materials

The CrCoNi MEA is FCC material [19]. Therefore, it is of utmost interest to look at different types of dislocation in FCC structures. The shortest possible translation vector of the lattice in FF materials or **b** is ½ <110> on {111} planes. The passage of ½ <110> dislocation leaves behind a perfect crystal. Thus, it is called a perfect dislocation. Figure 1.2 represents a passage of a perfect dislocation **b** = ½ [-101] (Fig. 1.2b) on (111) plane that corresponds to displacing an atom at position (a) to a position (c) (atoms are modeled as rigid spheres). In close-packed structures, the passage of a perfect dislocation can occur in two steps that correspond to displacing atom at (a) to (b) and then to (c) (Fig. 1.2a), *i.e.*, dislocation **b** = ½ [-101] passes as two partial dislocations ($\mathbf{b}_1$ = 1/6 [$\bar{2}$11] and $\mathbf{b}_2$ = 1/6 [$\bar{1}\bar{1}$2]) immediately one after the other (Fig. 1.2c). The partial dislocations with the form **b** = 1/6 <112> (Fig. 1.2a) are called Shockley partial dislocations and can freely glide on {111} planes. Under applied stress, the partials move in pairs bounded by a ribbon, with the leading partially creating the fault and the trailing one removing it. Unlike Shockley partial dislocations, Frank partial dislocations have **b** = 1/3 <111> and are normal to the {111} glide planes. Therefore, it is sessile, *i.e.*, it cannot glide.

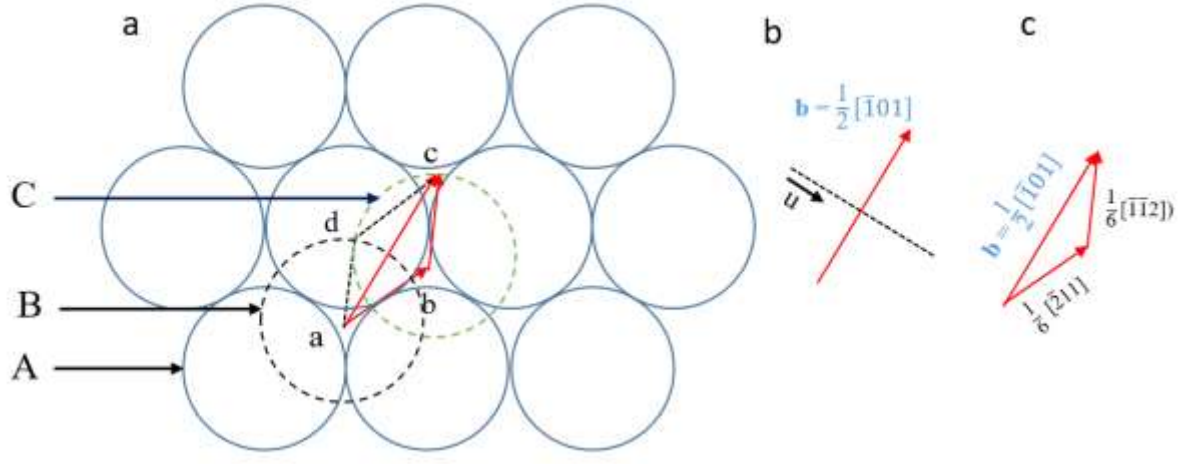

Fig. 1.2. (a) Atoms on the bottom side of a (111) glide plane, (b) a perfect edge dislocation with **b** = $\frac{1}{2}$[-101] and (c) component Shockley partials of the perfect dislocation in (b) [28].

1.2.2. Plastic deformation in FCC materials

Plastic deformation in FCC metallic materials occurs by slip, climb, and twinning [29]. Mechanisms of slip include conservative glide and cross slip. Conservative glide occurs when the glissile dislocation moves in its slip plane, *i.e.*, the plane containing its **u** and **b (**Fig. 1.3a-c**)**. The orientation of slip direction and normal to the slip plane make a slip system. There are 12 slip systems in FCC structures (numbered as they are incorporated in STABIX [44], a Matlab toolbox to analyze slip transfer through grain boundaries), as shown in Table 1.1.

In some cases, a dislocation can encounter an obstacle. Consequently, a dislocation switches from gliding on one slip plane to another different plane (cross slip plane). The two planes must belong in the {111} planes because they must contain the direction of **b**. Thus, only screw dislocation can cross slip [28]. Figures 1.4a-b show a dislocation bypassing an obstacle by cross slip.

Plastic deformation can also occur by a climb mechanism. For this case, dislocation moves out of its slip plane, *i.e.*, to a plane normal to its Burgers vector. This mechanism is assisted by vacancy/atoms diffusion. Figure 1.4c shows a cubic lattice, which contains vacancies. Under the action of temperature, these vacancies can be absorbed, which causes the dislocation to rise or climb, as shown in Fig. 1.4d. Like cross slip, dislocation climb also provides more freedom to dislocation motion [43].

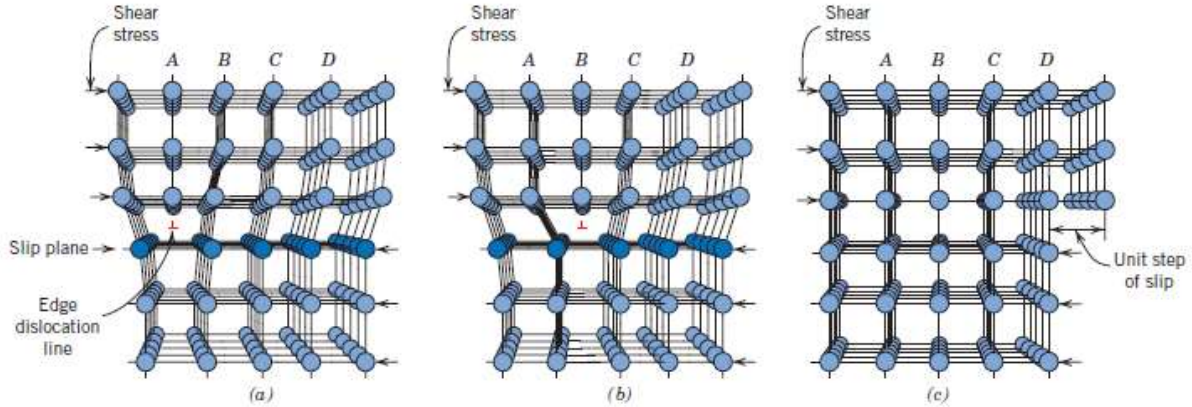

Fig. 1.3. Atomic rearrangements that accompany slip (motion of an edge dislocation on slip plane in response to applied shear stress [43].

Table 1.1. Twelve slip systems for FCC materials [45].

Slip system number	Slip plane normal	Slip direction
1	$[1\bar{1}1]$	[011]
2	$[\bar{1}\bar{1}1]$	[011]
3	[111]	$[0\bar{1}1]$
4	$[\bar{1}11]$	$[0\bar{1}1]$
5	$[\bar{1}11]$	[101]
6	$[\bar{1}\bar{1}1]$	[101]
7	[111]	$[\bar{1}01]$
8	$[1\bar{1}1]$	$[\bar{1}01]$
9	$[\bar{1}11]$	[110]
10	$[\bar{1}1\bar{1}]$	[110]
11	[111]	$[\bar{1}10]$
12	$[11\bar{1}]$	$[\bar{1}10]$

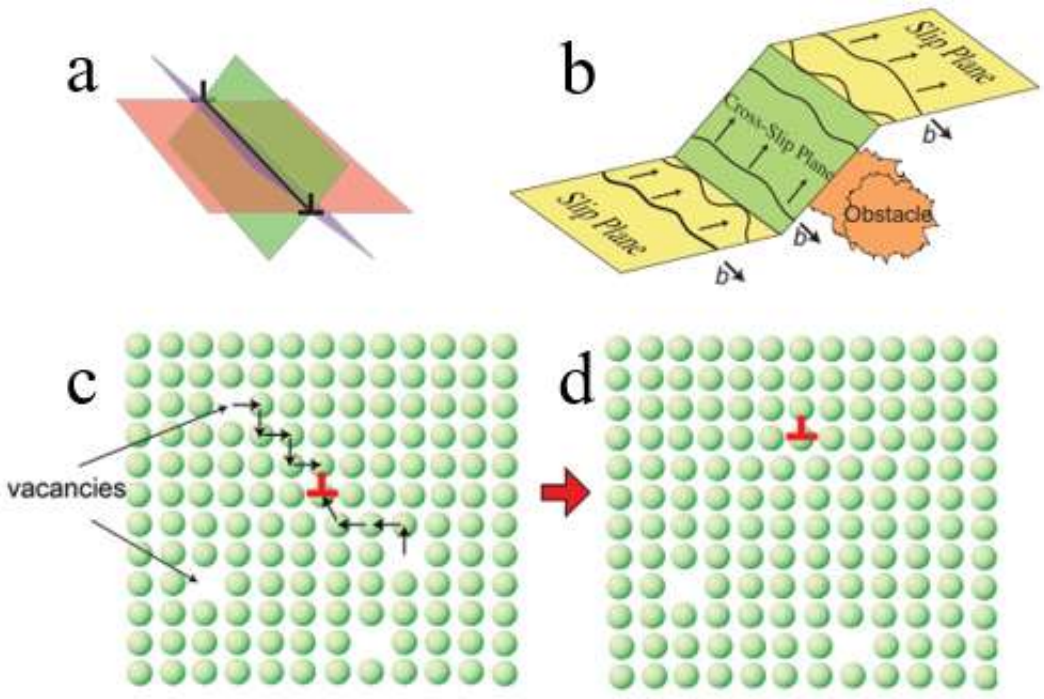

Fig. 1.4. (a) Pure screw dislocations with its available slip planes. (b) Dislocation switches from one slip plane to the other to bypass an obstacle. (c) A simple cubic lattice with vacancies. (d) Climbs by absorption of vacancies at the core of an edge dislocation [43]

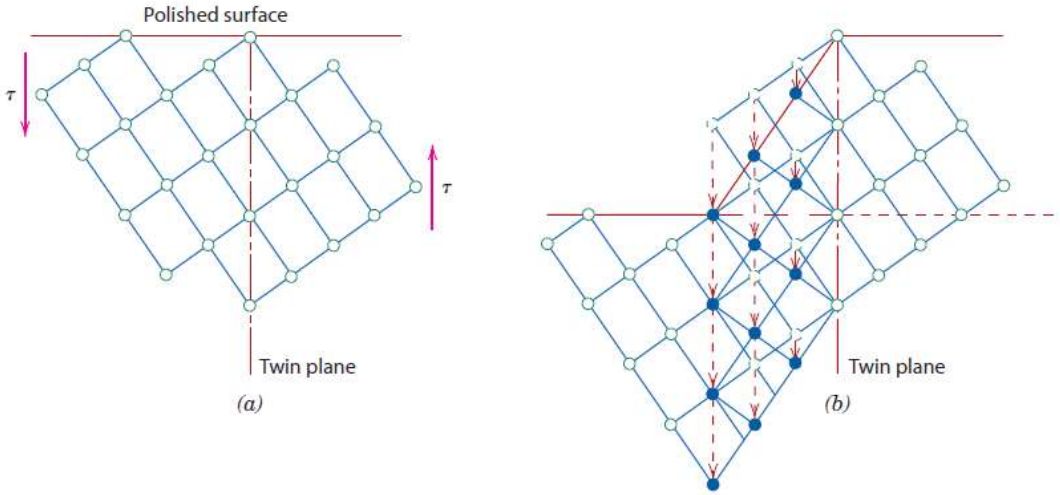

Fig. 1.5. (a) mechanical twinning results from the applied shear stress. (b) Twinning displaces atoms from their initial positions (open circles) to new positions (solid circles) in the twinned regions [43].

Furthermore, plastic deformation can occur by mechanical twinning. In the latter, a shear force can generate the displacement of atoms. Consequently, on one side of a twin boundary plane, atoms are located in mirror-image positions of atoms on the other side. Figures 1.5a-b show that mechanical twinning occurs due to shear stress that displaces the atoms from their original positions to the final positions in the twinned regions [43]. Mechanical twinning occurs on a specific crystallographic plane and direction. For example, the twin boundary plane and direction are {111} and <11-2>, respectively, in FCC structures [29]. The stress required to form a twin is less than that necessary for a slip. Nevertheless, twinning in FCC structures becomes significant when deformation occurs at low temperatures or high strain rates [46]. In addition, twinning reorients the crystals to create additional slips.

1.2.3. Stacking fault and its energy in FCC materials

The passage of perfect dislocation (corresponding to moving an atom from the B position to the next B position) keeps the perfect stacking of FCC structure with an ABCABCABCABCABC sequence intact (see Fig. 1.2a) [28]. The perfect dislocation can be decomposed into two partial dislocations. The passage of one partial dislocation (corresponding to moving an atom from B position to C position) changes the ABCABCABCABCABC sequence to the ABCAB**CACA**BCABC. The four **CACA** planes correspond to the stacking fault and have an HCP structure (higher Gibbs free energy than the FCC structure). The energy associated with the stacking fault determines the separation between the two partial dislocations (d_p) [47]. The

stacking fault energy (SFE) is calculated, assuming isotropic elasticity, based on the following equation:

$$SFE = \frac{Gb_p^2}{8\pi d_p}\left(\frac{2-\nu}{1-\nu}\right)\left(1-\frac{2\nu\cos(2\beta)}{2-\nu}\right) \quad (1.1)$$

Where G is the shear modulus, b_p is the magnitude of the Burgers vector of the two partial dislocations and β is the angle between the line and burger vector direction [47]. Metal such as silver has a low SFE of 22 mJ m^{-2} and d_p of 9 nm while metals such as nickel have a high SFE of 128 mJ m^{-2} and d_p of 2.9 nm [45].

SFE significantly affects the plastic deformation of low SFE FCC metals and alloys. Mechanical twinning is the dominant deformation mechanism due to the decreasing twinning stress (σ_T) with the SFE as quantified by the following relation:

$$\sigma_T = K\left(\frac{SFE}{Gb}\right)^{1/2} \quad (1.2)$$

Where K is a constant, and b is the magnitude of the Burgers vector.

Cross slip is difficult to achieve because the 1/6<112> Shockley partial dislocations cannot do it. The two partial dislocations are constrained to glide on a specific the {111} plane. Cross slip can only occur when the partial dislocations are forced together to re-form a perfect screw dislocation which is difficult if d_p is large [29].

1.3. Fundamentals of grain boundaries in FCC materials

A GB is a planar defect dividing two grains of the same structure but different crystallographic orientations. It is an active structural element with an average thickness of less than two atomic diameters, but it controls a wide range of properties of polycrystalline materials [16], [48], [49].

Five macroscopic and four microscopic parameters define it [50], [51]. Figure 1.6 is a schematic representation of the five macroscopic parameters of the GB. The three macroscopic parameters that define the orientation of the grains are represented either as misorientation angle/axis of rotation (θ/ [u v w]) or as Euler angles (φ1, Φ, φ2) in Bunge definition. They can directly be acquired from, for example, a 2D electron backscatter diffraction (2D-EBSD) map [52].

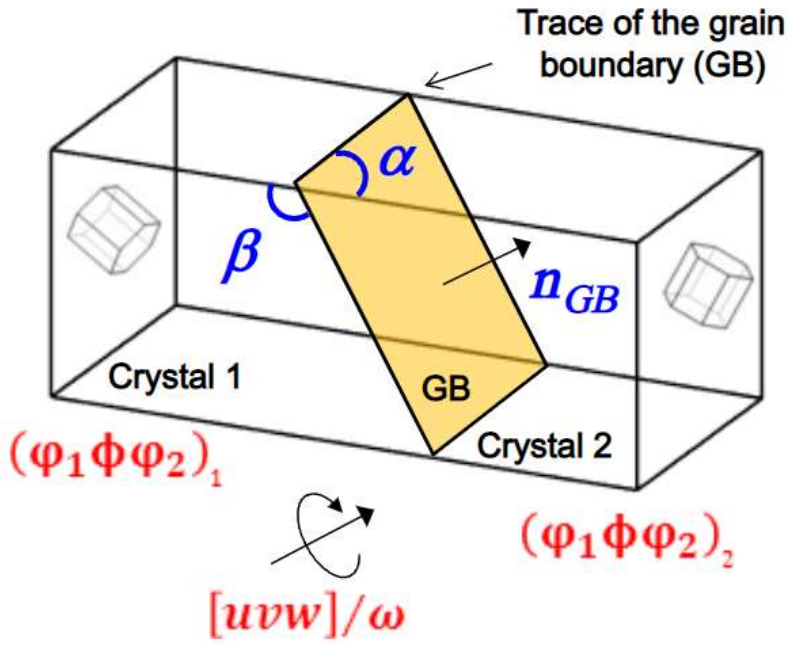

Fig. 1.6. Schematic representation of the five macroscopic parameters of a GB [53].

Based on θ, GB can be categorized into high angle grain boundaries (HAGBs) and low angle grain boundaries (LAGBs). The transition θ from LAGB to HAGB is between 10 and 15° [43]. The two remaining macroscopic parameters that define the orientation of the GB plane are given by its trace angle on the surface and GB normal (n_{GB}) or GB inclination angle (β). The trace angle can be obtained from the EBSD map, whereas n_{GB} and β are obtained from 3D EBSD by serial polishing or focused ion beam sectioning [53].

Based on the relative orientations of the rotation axis [u v w] with respect to the boundary plane {h k l}, different types of boundaries can be obtained. A tilt and twist GB occur when the rotation axis is parallel and perpendicular to the GB plane, respectively. A mixed GB occurs when the rotation axis is inclined with respect to the GB plane [54].

In the four microscopic parameters, two parameters define translations within the GB plane, one parameter defines the expansion perpendicular to the GB plane, and the remaining parameter describes the position of the GB plane along its normal. They are energy parameters that are obtained from the calculated most energetically stable atomic structure [1].

1.3.1. Structure of the grain boundary

A periodic array of dislocations accommodate the low misorientation of the LAGB [55]. Fig. 1.7a shows a low angle symmetrical tilt boundary made of parallel edge dislocations with

the same Burgers vector aligned perpendicular to the slip plane. The spacing between two dislocations (D) is obtained using the relation:

$$D = \frac{|\mathbf{b}|}{2 \sin (\theta/2)} \tag{1.3}$$

When the θ value increases, D becomes very small. At D value equals to few atomic spacing, the dislocation core energy overlaps. Thus, the boundary cannot be defined by simple dislocation arrangements, and the above equation ceases to be valid. Like low angle tilt boundaries, low angle twist and mixed boundaries are made of a periodic array of the screw and mixed dislocations, respectively. Fig. 1.7b is an accurate electron channeling contrast micrograph of a LAGB showing an array of dislocations in uranium dioxide [56]. Such LAGB has θ = 0.25-0.5° (from the EBSD map in Fig.1.7c).

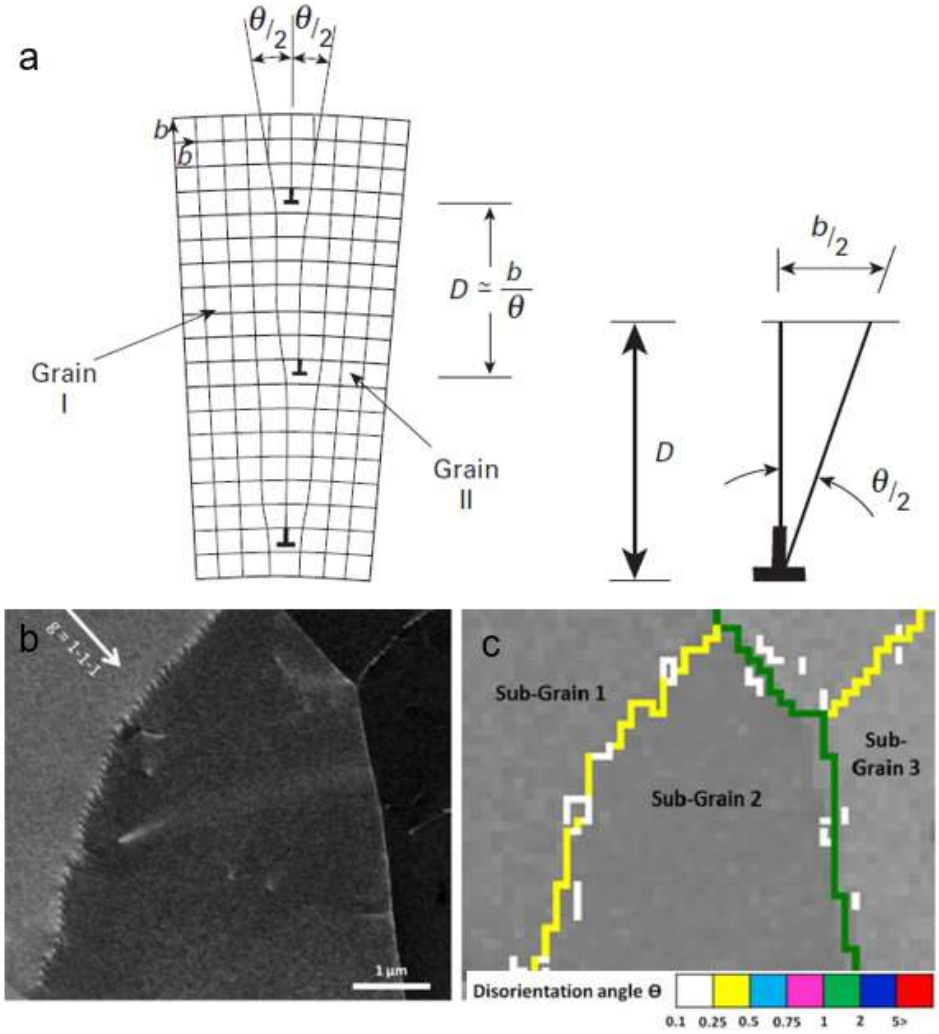

Fig. 1.7. Low angle symmetric tilt grain boundary [29]. (b) Accurate electron channeling contrast imaging of a low angle grain boundary in Uranium oxide. (c) Electron backscatter diffraction map of Fig. 1.7b [56].

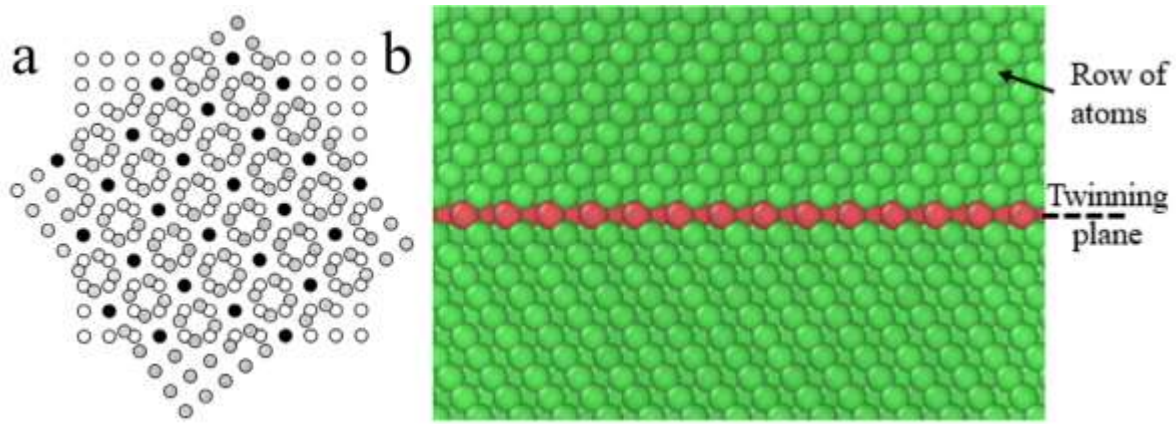

Fig. 1.8. (a) A schematic of the Σ5 CSL boundary. Filled circles are sites common to both lattices. (b) Coherent twin boundary in pure Ni.

The dislocation model cannot describe a high angle grain boundary (HAGB), as is the case for the LAGB, because the model fails at an angle greater than the transition θ between 10° and 15° [43]. The failure of the dislocation model for such larger θ is fundamentally linked to a need for minimizing GB energy that requires a strict periodic arrangement of dislocations. Instead, it is described using the geometrical concept of the coincidence site lattice (CSL) [57]. Some crystallographic planes continue through the GB from one grain to the other in a crystal. Consequently, atomic positions in the GB coincide with ideal positions of both adjacent lattices. Such lattice points make a CSL, an intersection of translation subsets of the two crystal lattices.

The CSL is characterized by a coincidence index (Σ). The latter is equal to the inverse of the fraction of lattice sites that coincide. It can also be the ratio of the volume of the CSL primitive cell to the volume of the lattice primitive cell [58]. Σ is always a whole number and is odd for cubic crystals. Fig. 1.8a shows a Σ5 CSL formed by rotation of two simple cubic lattices by the angle of 36.9° about <001> axis. GB between two grains with the highest number of coincidence sites is called the CSL boundary or special boundary. For example, a twin boundary (TB) is a CSL boundary with Σ = 3. On one side, if the TB is parallel to the twinning plane and the atoms in the boundary fit perfectly into both grains, it is called a coherent twin boundary. Fig. 1.8b is a coherent twin boundary with atoms in the twinning plane (red) fit with rows of atoms in both grains (green). On the other hand, if the twin boundary does not lie precisely parallel to the twinning plane and the atoms do not fit perfectly into each grain, it is an incoherent twin boundary.

1.3.2. Energy of a grain boundary

The dislocation Read-Shockley model of the LAGB can be used to calculate its energy [55]. The LAGB energy is the sum of energies from its constitutive dislocations. The following equation gives the energy for a case of an edge dislocation:

$$E_e = \frac{Gb}{4\pi(1-\nu)} \ln\left(\frac{D}{r_o}\right) + E_c \quad (1.4)$$

Where G is the shear modulus, ν is the Poisson's ratio, r_o is the cut-off radius of the dislocation core, and E_c is the energy of the dislocation core. For a symmetrical tilt LAGB, the number of dislocations per unit length (n) can be obtained as n = 1/D = θ/b [59]. Thus, its energy per unit length is then given by:

$$\gamma_{GB} = \frac{\theta}{b}\left\{\left[\frac{Gb^2}{4\pi(1-\nu)}\ln\left(\frac{1}{\theta}\right)\right] + E_c\right\} \quad (1.5)$$

From the above equation, γ_{GB} varies linearly with θ at low angles as shown in Fig. 1.9, the GB energy increases and deviates from 10-15°.

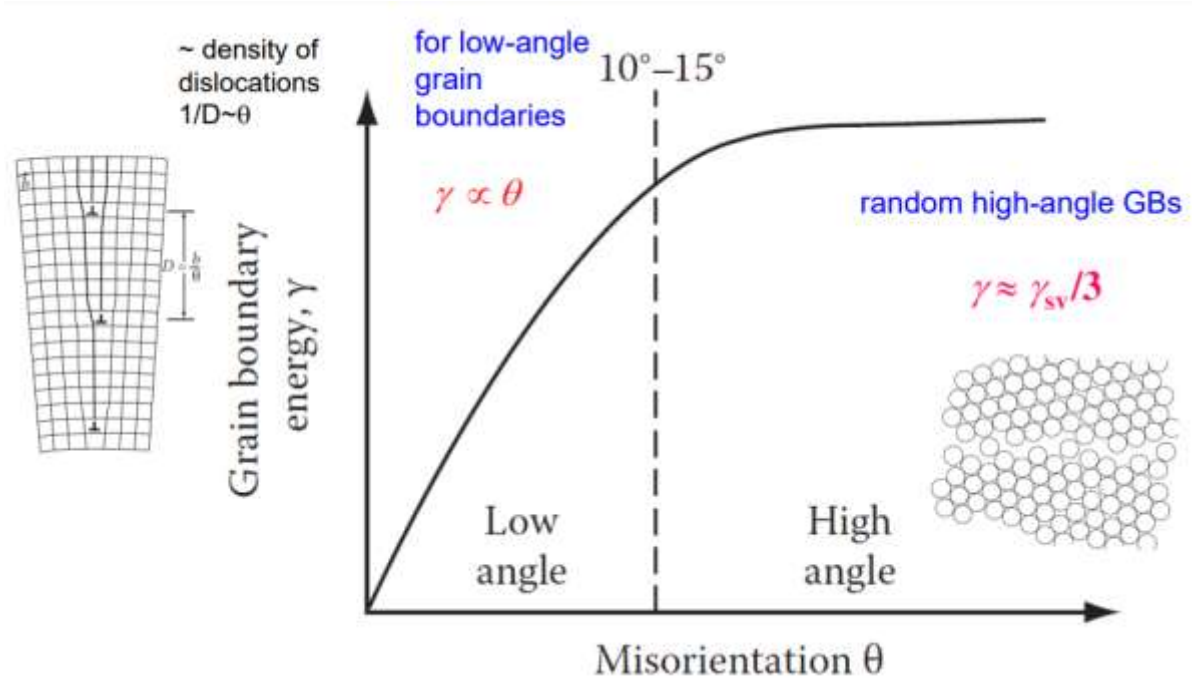

Fig. 1.9. θ against GB energy for LAGB [54].

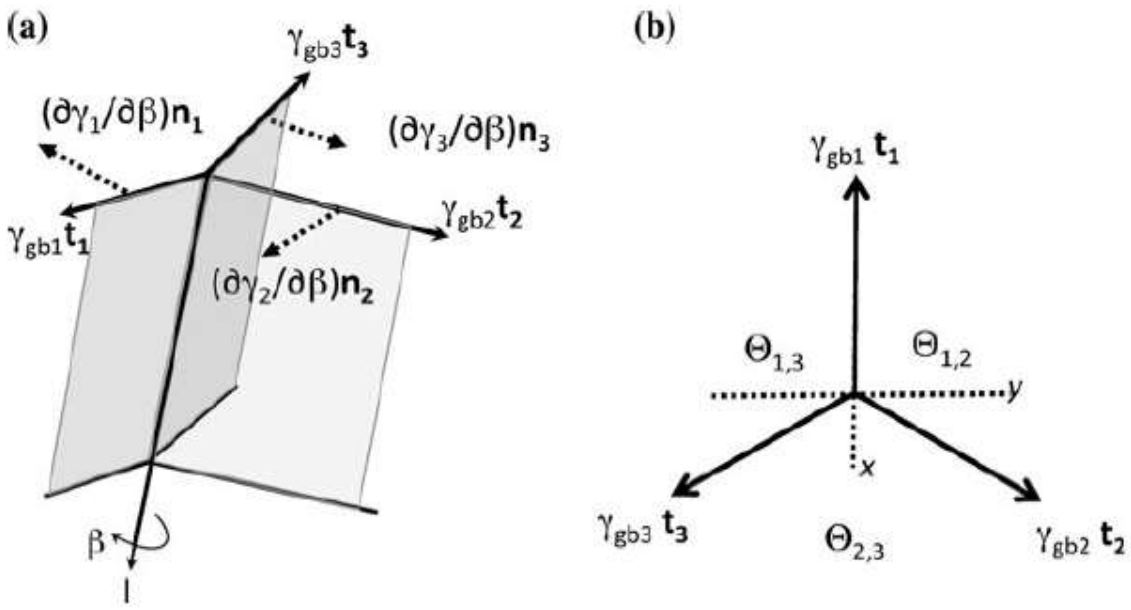

Fig. 1.10. Schematic representation of the balance of interfacial energies at triple junctions: (a) tangential and normal vectors in the Herring relation and (b) If the torque terms are ignored, only the tensions must balance [60].

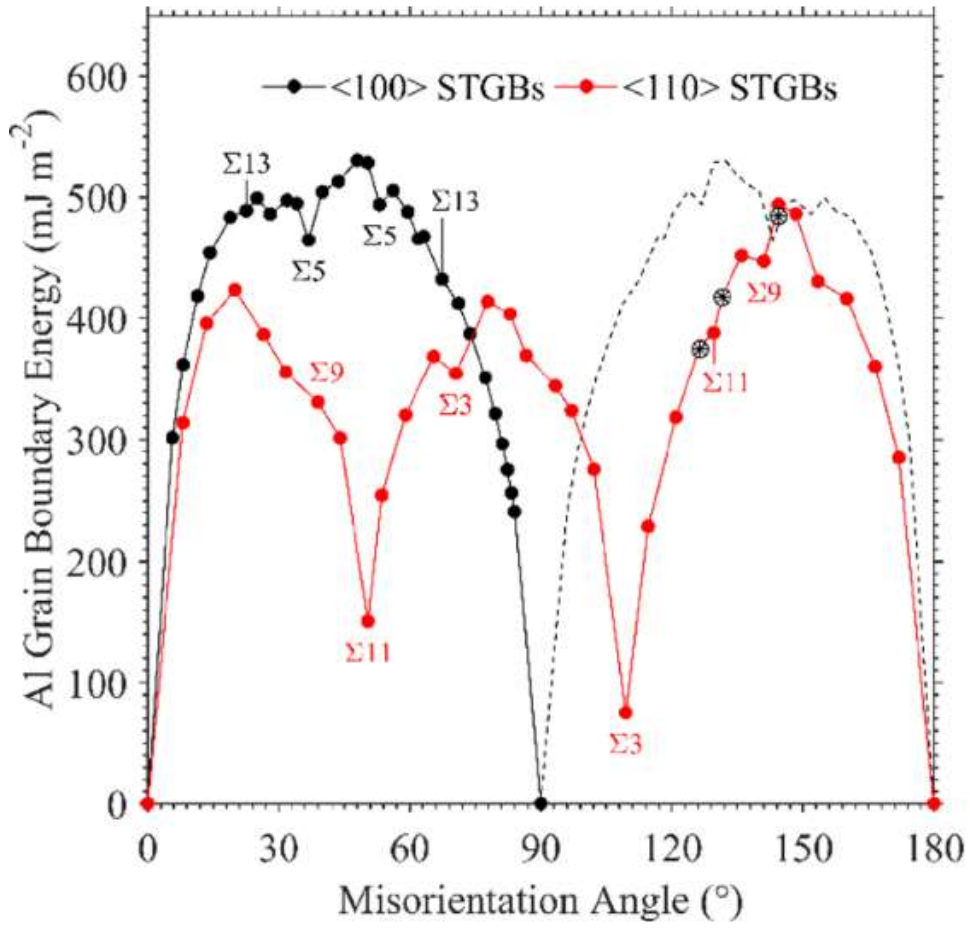

Fig. 1.11. GB energy as a function of θ for <111> and <110> symmetrical tilt GB in aluminium [61].

Unlike LAGB, the energy of the HAGB is calculated using the geometry of the interfacial junctions. It is calculated based on Fig. 1.10a-b and a simplified Young's equation [61] of the form:

$$\frac{\gamma_{gb1}}{\sin\theta_{2,3}} = \frac{\gamma_{gb2}}{\sin\theta_{1,3}} = \frac{\gamma_{gb3}}{\sin\theta_{1,2}} \quad (1.6)$$

Where γ_{gb1}, γ_{gb2} and γ_{gb3} are the energy of the three interfaces, and $\theta_{2,3}$, $\theta_{1,3}$ and $\theta_{1,3}$ are the misorientations across the boundaries. The relative GB energy can be determined by measuring dihedral angles between crystal misorientation across the boundaries.

Fig. 1.11 shows θ against γ_{GB} for <100> and <110> tilt HAGB in Al [61]. The <110> symmetrical tilt HAGB shows various minima with the lowest corresponding to the $\Sigma 3$ twin boundary. Furthermore, the curves show that the energy and misorientation relationship is not straightforward. Through a large number of measurements, it was found that there is not a simple relationship between γ_{GB} and its corresponding geometry. It was then suggested that the microscopic parameters of the GB may be controlling the γ_{GB}.

1.4. Dislocation-grain boundary interactions in FCC materials

1.4.1. Fundamentals of dislocation-grain boundary interactions

Under the action of applied stress, lattice dislocations glide on slip planes until they encounter an obstacle such as a GB. Fig. 1.12a is a transmission electron microscope (TEM) micrograph that displays a pile-up of dislocations against a GB in stainless steel [62]. The interactions of the leading dislocation with the GB take place when the stress at the front of the pile-up reaches a critical value (τ_c), *i.e.*,

$$\tau_c = n_p \tau_e \quad (1.7)$$

where $n_p\tau_e$ is the stress at the front of the pile-up, n_p is the number of dislocations in the pile-up and τ_e is the applied shear stress contributing to the dislocation pile-up. Consequently, different interactions mechanisms, which occur, depend on dislocation character (screw, edge, and mixed) and GB properties (GB type, plane, internal structure, energy, chemical composition, geometry, among others).

A pile-up of dislocations on a given slip system in grain A with the orientation of slip direction d_α^A and the orientation of the slip plane normal n_α^A can induce a wide range of interactions

mechanisms when τ_c is reached as depicted in Fig. 1.13b. The lattice dislocations on the incoming slip plane can be absorbed into the GB with (Fig. 1.13b) or without (Fig.1.13c-d) emission of dislocation in the adjacent grain. Pond et al. [13] discussed that absorbed lattice dislocation into random HAGB dissociate into GB dislocations with small and finite **b.** Using molecular dynamics (MD) simulations in Al, Chandra et al. [63] revealed that the absorption of lattice dislocation into the HAGB was found to vary with misorientation angle or GB energy. Both Pond et al. [13] and Chandra et al. [63] agreed that temperature plays an important role. They argued high temperatures modify the atomic structure of the HAGB. Consequently, there is a formation of a highly disordered HAGB with thermal defects. Moreover, they observed absorption of lattice dislocation with the emission of Shockley partial dislocation [64].

Dislocation can be also transmitted across a GB with [Fig. 1.13e] or without [Fig. 1.13f] leaving a residual burgers vector into the GB. The transmitted dislocations as shown in Fig. 1.13 is on an outgoing slip system with the orientation of slip direction d_β^B and orientation of slip plane normal n_β^B. The mechanisms of transmission of lattice dislocation across different GB have been examined using experiments and molecular dynamics simulations. Shen et al. [64] observed, using TEM, the transmission of dislocation across Σ3 TB with or without residual GB dislocation in lightly deformed 304 stainless steel. The pileup of dislocations against the TB, which induced an array of dislocations, is depicted in Fig. 1.12b. Inside a TEM, using in-situ nanoindentation near a (100) low angle tilt GB with a dislocation spacing of 19 nm inside a TEM in SrO3, acquired live micrographs showed the transmission of dislocation across the LAGB [65]. Lim et al. [59] investigated the slip-twin boundary interactions in nickel at 587K and observed a direct transmission of dislocation across coherent TBs which was due to cross slipping of screw dislocations. Transmission across a TB was also observed when the incoming and outgoing slip systems shared a common line and lattice dislocations have screw character with a line direction parallel to the common line in 310 stainless steel [66]. Indirect transmission of dislocations across a TB was also been observed in the same Cu foil [67]. Fig.1.12c shows the transmission of an array of dislocations across a HAGB [64].

Lattice dislocations can also be reflected in the original grain A (Fig.13h). The refection is due to a significant resistance to transmission of lattice dislocations due to the lack of favorably oriented glide planes in the neighboring crystal. The ejection of dislocation back into their original grain has been observed in ref. [66]. Shen et al. [12] also observed that the incoming dislocation on a given plane reflected in the original grain on a different slip plane.

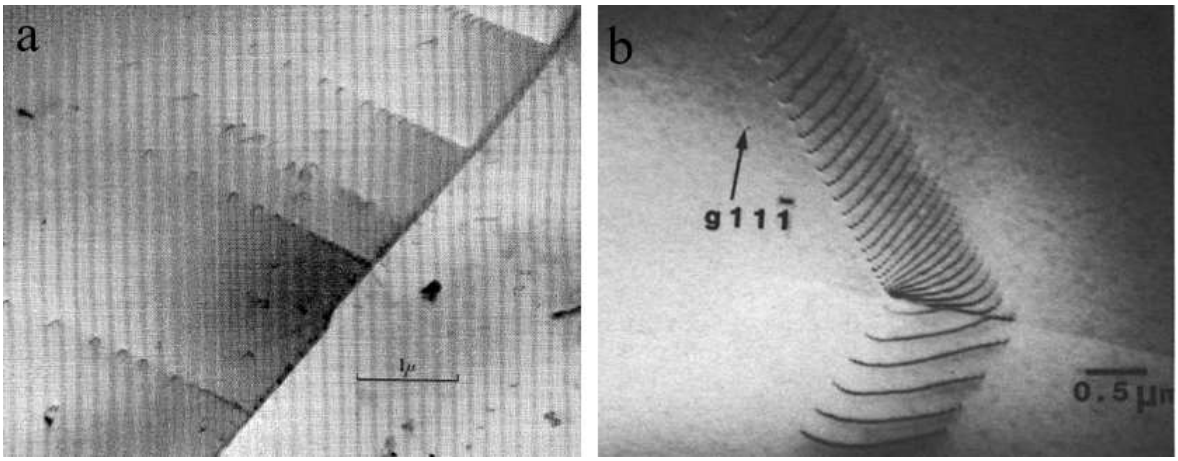

1.12. (a) Pile-ups consist in part of regularly spaced dislocations [62]. (b) the pile-up penetrates the boundary and generates another array of dislocations in the second crystal [64]

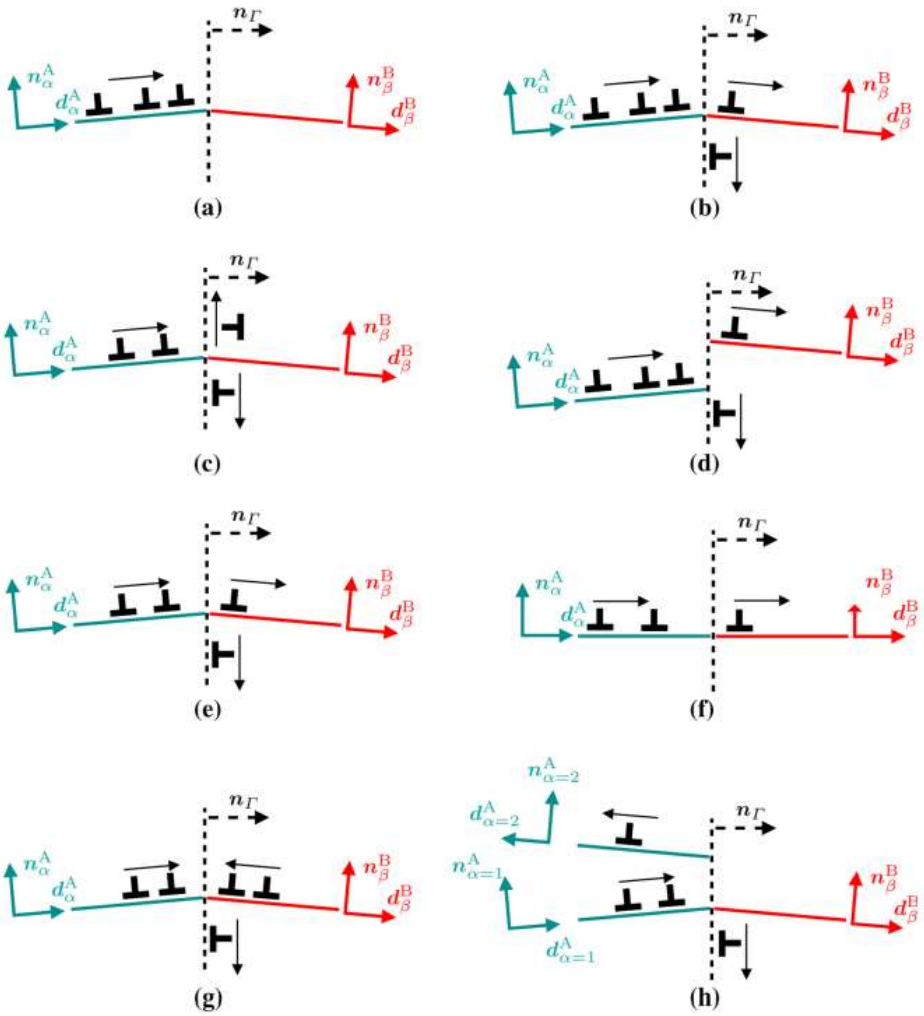

1.13. Slip transfer and dislocation interaction mechanisms in adjacent grain A and B, separated by grain boundary plane n_Γ [68].

1.4.2. Slip transfer criteria

Various criteria have been developed to predict which slip system will be activated in grain B due to the pile-up of dislocations on a given slip system in grain A. Using a series of experiments on bi-crystals, Livingston and Chalmers formulate a geometrical slip transmission criterion as follow [69]:

$$N = \left(n_{\alpha}^{A} \cdot n_{\beta}^{B}\right)\left(d_{\alpha}^{A} \cdot d_{\beta}^{B}\right) + \left(n_{\alpha}^{A} \cdot d_{\beta}^{B}\right)\left(n_{\beta}^{B} \cdot d_{\alpha}^{A}\right) \quad (1.8)$$

The symbols in the equations have been defined in section 1.4.1. The activated slip system in grain B is the one with maximum N. This criterion is based on the fact that the stress state on the adjacent grain due to the incoming pileup of dislocations is of pure shear type. This geometrical criterion alone cannot predict the exact activated slip system except in some special cases such as the direct transmission of screw dislocations across a twin boundary [70].

Shen *et al.* [12], [64] developed another geometrical factor that takes into account the grain boundary plane n_{Γ}. It is expressed as follows:

$$M = \left(l_{\alpha}^{A} \cdot l_{\beta}^{B}\right)\left(d_{\alpha}^{A} \cdot d_{\beta}^{B}\right) \quad (1.9)$$

Where l_{α}^{A} and l_{β}^{B} are normalized vectors of the lines of intersection between GB and incoming and outgoing slip planes. The combination of slip systems, which minimize the angles between their intersecting lines and their glide directions are chosen as the preferred incoming and outgoing slip systems.

Luster and Morris [71] simplified the N-factor and introduced Luster and Morris m' parameter by removing the second part of the eq. 1.7 as follows:

$$m' = \left(n_{\alpha}^{A} \cdot n_{\beta}^{B}\right)\left(d_{\alpha}^{A} \cdot d_{\beta}^{B}\right) \quad (1.10)$$

The Luster and Morris m' parameter considers the degree of co-planarity of the slip systems, and the GB is transparent when m' = 1 while it is impenetrable when m' = 0. Bieler *et al.* [72] investigated slip transfer in pure Al and found that the slip transfer across GBs is rare and occurs when m' > 0.97, which corresponds to the LAGB.

The resolved shear stress criterion states that the activated slip system has maximum resolved shear stress [64]. It is quantified as:

$$\tau_{\alpha}^{A} = \tau_{\beta}^{B} \cdot N \quad (1.11)$$

Where τ_{α}^{A} and τ_{β}^{B} are the shear stress at the head of the pileup of dislocations in their slip plane and the shear acting on the outgoing slip system, respectively. The resolved shear stress criterion based on maximizing the Peach–Koehler force on the activated slip system and the M factor criterion has been used to successfully predict the outgoing slip system. The M factor determines the slip plane and the shear stress criterion determines the orientation of the slip direction [12], [64].

When there are multiple slip directions with equal resolved shear stress, the residual Burgers vector criterion can be used. The activated slip system is the one that leaves a minimum residual burgers vector [66], [73]. The residual burgers vector (b_r) is given by:

$$b_r = b_i - Rb_o \tag{1.12}$$

where b_1 and b_2 are the Burgers vectors of the incident slip dislocation and the transmitted slip dislocation, respectively, and R is the rotation matrix that characterizes θ across the GB. A study of 189 dislocation-GB interactions in nickel crystals using MD simulations has shown that minimum b_r crucially determine whether a dislocation can or cannot cross the GB [74].

1.5. Fundamentals of CrCoNi medium entropy alloys

The CrCoNi MEA possesses an exceptional combination of mechanical properties at room and cryogenic temperatures. For example, a cold-forged and cold-rolled sample followed by annealing exhibited a tensile strength of 1.3 GPa, ductility up to 90%, and fracture toughness of 275 $MPa{\cdot}m^{-1/2}$ at cryogenic temperature or 77K [75]. Moreover, its strength was found to reach even as higher as 2 GPa for annealed samples after high-pressure torsion [76]. Such properties are higher than the CrMnFeCoNi alloy with more elements [19] and most conventional alloys, as shown on the Ashby plot of yield stress against fracture toughness (Fig. 1.14b). Thus, this alloy has potential applications in the aerospace, energy, oil, and gas sectors as they have excellent strength, ductility, oxidation resistance, and thermal stability [46], [75]. Some of the reasons for the outstanding mechanical properties of this alloy have been associated with its low SFE and high shear modulus [19] (see section 1.5.2). The low SF energy does not only favors the planar glide of dissociated dislocations and hinders cross-slip, but also promotes deformation twinning. This latter deformation mechanism introduces coherent interfaces acting as barriers to dislocation motion and leads to a dynamic Hall-Petch effect without reducing ductility [19].

Before the converging to the term "high entropy alloy (HEA)" by Yeh *et al.* [77], [78], Ranganathan [79] called them "multimetallic cocktails" in his article “Alloyed pleasures: multimetallic cocktails” while Cantor [80] called them “multicomponent” in his article “ microstructural development in equiatomic multicomponent alloys.” HEAs can be defined in terms of composition or configuration entropy [81]. In terms of compositions, HEAs contain at least five principal elements in approximately equiatomic concentrations as follow:

$$\begin{aligned} n_i \geq 5 \; ; \; 5\% \leq X_i \leq 35\% \\ n_j \geq 0 \; ; \; X_j \leq 5\% \end{aligned} \tag{1.13}$$

where n_i and n_j are the number of principal and minor elements, respectively, and X_i and X_j are atomic weight percentage of the principal and minor elements, respectively. The minor elements are added to enhance targeted properties [82].

The configuration entropy (ΔS_{conf}) is the most important component of the entropy of mixing in the Gibbs free energy of mixing given by the relationship :

$$\Delta G_{mix} = \Delta H_{mix} - T\Delta S_{mix} \tag{1.14}$$

where ΔG_{mix} is the Gibbs free energy of mixing, ΔH_{mix} is the enthalpy of mixing, T is the temperature and ΔS_{mix} is the entropy of mixing. ΔH_{mix} can be neglected for an ideal solution. Thus, the change in ΔG_{mix} is caused by ΔS_{mix} which given by ΔS_{conf}. For an equiatomic alloy with atoms occupying random positions, ΔS_{conf} is given a modified Boltzmann equation:

$$\Delta S_{conf} = R_g \ln(n) \tag{1.15}$$

Where Rg is the perfect gas constant and n is the number of elements. High n increases ΔS_{mix} term and lowers ΔG_{mix}. The decrease ΔG_{mix} was suggested to promote the formation of stable solid solutions over intermetallic compounds [77], [78]. HEAs are alloys with $\Delta S_{conf} \geq 1.5R_g$ as shown in Fig.1.14a. Conventional alloys such as steels, aluminum alloys, titanium alloys, and so forth have $\Delta S_{conf} \leq 0.69R_g$. Between HEAs and conventional alloys, there are medium entropy alloys (MEA). The latter are mainly developed from HEAs and comprise 2-4 principal elements.

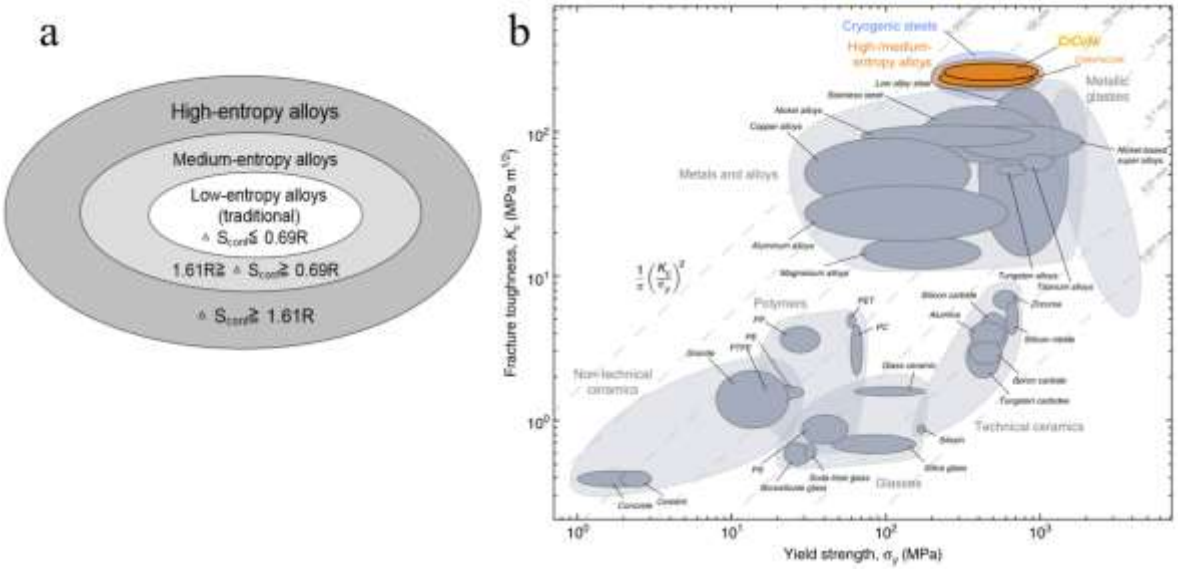

Fig. 1. 14. (a) Classification of alloys based on configuration entropy. (b) Ashby map of fracture toughness versus yield strength for various classes of materials [75].

1.5.1. Processing and microstructure

Pure Cr, Co, and Ni (purity above 99.99%) are melted at ~ 1690 K before being subjected to various thermomechanical processing methods such as rotary swaging followed by annealing [19], high-pressure torsion followed by annealing [76], etc. The latter controls the final microstructure and properties.

Backscatter electron (BSE) imaging, EBSD mapping, and x-ray diffraction (XRD) analysis have revealed that cast and thermomechanical processed CrCoNi MEA exhibit a single-phase [19]. Figure 1.15a is an x-ray diffractogram revealing that the single-phase has an FCC structure with a lattice parameter of between 0.356 nm and 0.357 nm [19], [83]–[85]. Fig. 1.15b displays a BSE micrograph of annealed specimen at 900°C for 1 hour after cold rolling [86]. The microstructure consists of equiaxed grains with significant annealing twins. The chemical composition of CrCoNi produced by different processing techniques slightly varies, but it is always close to the equiatomic compositions. Wave dispersive spectroscopy (WDS) revealed that CrCoNi single crystals grown using the Bridgman method have a composition of 33.42Ni-33.60-Co-32.98Cr (in at. %) [85]. Similarly, x-ray fluorescence analysis and energy dispersive spectroscopy (EDS) analysis of a recrystallized polycrystalline CrCoNi MEA that was previously rotary swagged revealed a chemical composition of 32.53Cr-33.30Co-32.85Ni (at.%) [19].

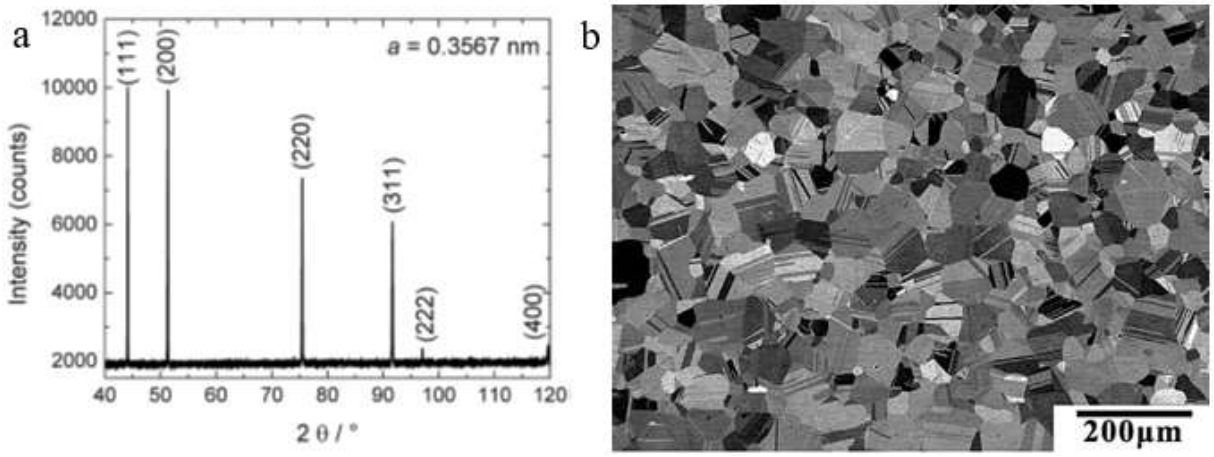

Fig. 1.15. (a) X-ray diffractogram of the recrystallized CrCoNi alloy indexed as single-phase FCC [19]. (b) Backscattering electron (BSE) micrograph of CrCoNi MEA after cold rolling and annealing at 1000°C for 1 hour [86].

Moreover, Gludovatz *et al*. [75] found a chemical composition of 32.55Cr-34.01Co-34.4Ni for a recrystallized sample that was previously subjected to cold forging and cross rolling. Since scanning electron microscopy (SEM)-based techniques and XRD are relatively coarse observations, some researchers went further and used TEM to investigate if there are secondary phases in CrCoNi MEA. On the one hand, Laplanche *et al.* [19] characterized specimens that had been rotary swagged (reduced diameter from 40.0 mm to 16.5 mm, *i.e.*, the total strain of 1.6%) and recrystallized at 1173 K for 1 hour in the air and found no secondary phases. Similarly, Praveen *et al*. [87] did not find any secondary phase using both transmission electron microscopy (TEM) and scanning transmission electron microscope-energy dispersive x-rays spectroscopy (STEM-EDS) on a sample that had been subjected to high-pressure torsion and annealing at 500-600°C for 2-60min. On the other hand, Deng *et al.* [84] observed annealing induced hexagonal close-packed (HCP) lamellae in specimens that were subjected to three equal channel angular pressing and annealing at 500°C. Miao *et al.* [88] also observed HCP lamellae after severe tensile deformation (>41% plastic strain level) followed by recrystallization at 1198K for 1 hour. In summary, the alloy has a single FCC from the melt and an additional secondary HCP phase observable in thermomechanical processed CrCoNi MEA.

1.5.2. Plastic deformation

In CrCoNi MEA alloy, plastic deformation is initially dominated by the glide of ½ <110> dislocations which can be dissociated into two 1/6 <112> Shockley partials bounded by a stacking fault along several {111} planes [19], [88], [89].

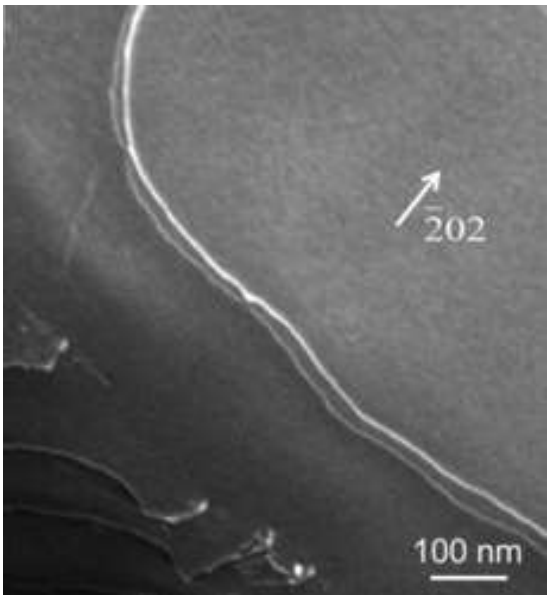

Fig. 1.16. Weak beam dark-field scanning transmission electron microscope micrograph showing Shockley partials dislocations of a dissociated dislocation in equiatomic CrCoNi MEA [90].

TEM micrograph (see Fig. 1.16) depicts two partial dislocations bounding a stacking fault in the cold-rolled and annealed sample of CrCoNi MEA that was deformed using a tensile test at an engineering strain rate of $10^{-3}s^{-1}$ [90], [91]. The SFE of the CrCoNi MEA has been calculated using Eq. 1.1 and by measuring d_p and β from the TEM micrographs. Laplanche *et al.* [19] measured d_p ~ 5 nm and ~10 nm near the screw and edge orientations, respectively, which gives approximate SFE of 22 ± 4 mJm^{-2}. The d_p are larger than ~ 4 and 6.5 nm measured in Cantor alloy, *i.e.,* SFE of CrCoNi MEA is lower than that of Cantor alloy of ~25 mJ m^{-2} [92]. Zhang *et al.* [93] calculated the value of SFE of an annealed sample at 1293K for 120h was 23.33 ± 4.31 mJm^{-2} [94]. Such values of the SFE are comparable to transformed induced plasticity steel (14-23 mJ m^{-2}) [95] and Hadfield and stainless steel (~ 16-28 mJ m^{-2}) [96].

The CrCoNi MEA is a low SFE material. Therefore, mechanical twinning is an important deformation mechanism. The early formed Shockley partials gliding on neighboring {111} planes act as precursors for the nucleation of twins [97]. The formation of twins depends on both strain rate and temperature. Mechanical twins increase with increased strain level while the volume fraction of twins at cryogenic temperature is higher than that at room temperature for the same strain level [19]. This occurrence agrees with the widely known fact that lowering temperature favors twinning over slip because the nucleation of dislocation is a thermal activation process, which is very difficult at low temperatures [29]. Stacking faults and

mechanical twins impede the dislocations' motion and increase the work hardening rate by delaying the onset of necking which increases ductility in this alloy [85].

Furthermore, Benay *et al*. [85] also observed the interactions of primary and secondary slip systems, resulting in a carpet-like structure. Continuous deformations of these carpet structures lead to high dislocation density dislocations walls. The latter was also observed in highly deformed Hadfield steels [97]. The formation of t high dislocation density dislocations walls is responsible for additional work hardening. Further enhancement of work hardening rates comes from the phase transformation from FCC to HCP phases close to twins and stacking faults [88]. A significant work hardening occurs even though the transformed volume is very small, *i.e.*, most HCP regions show thicknesses on several atomic layers [98].

1.5.3. Dislocation-grain boundary interactions

A CrCoNi MEA exhibits a strong Hall-Petch solid effect. Lu *et al.* [42] agreed well with GB strengthening because the yield strength increased from 248 MPa to 848 MPa when the grain size decreased from 50.00 μm to 0.56 μm. Similarly, Table 2 shows an immense increase in yield and tensile strength when the grain size is reduced to create a refined microstructure. For example, the yield stress quadruples from coarse-grained microstructure (20 μm) to ultrafine-grained microstructure (0.65 μm) [76]. Compared to other FCC alloys with the same mean grain size, Fig.1.17a shows that the CrCoNi alloy exhibits a higher Hall-Petch slope [42]. It can reach as high as above 600 $MPa \cdot \mu m^{-1/2}$[21], [42]. Schneider *et al.* [21] observed that GB and TB impede dislocation motion using a STEM. These results conclude that GB and TB contribute to the strengthening of CrCoNi. However, they found that the strength of boundaries depends on the operating slip transfer mechanisms while quantifying the strength of TB and GB. However, to our knowledge, there are limited studies that investigated slip transfer mechanisms in the CrCoNi MEA. Liang *et al.* [99] investigated the slip transfer mechanisms across TB using *in situ* TEM deformation on annealed samples. They observed classical slip transmissions mechanisms such as pile-up of dislocations against TB, transmission, and reflection of dislocations at TB (Fig. 1.16b). They also found that TB could act as a dislocation source to produce large slip bands. Thus, the present thesis investigates the interactions of dislocations with the different types of microstructural features such as GB (LAGB and HAGB), which is crucial for an understanding of the individual contribution of those features to the overall strength of the alloy.

Table 2. Tensile properties of CrCoNi medium entropy alloy at 297K [76].

	Mean grain size(μm)	Yield strength (MPa)	Tensile strength (MPa)
Ultrafine grained	0.65	1435	1580
Fine grained	1.5	832	1053
Coarse grained	20	374	843

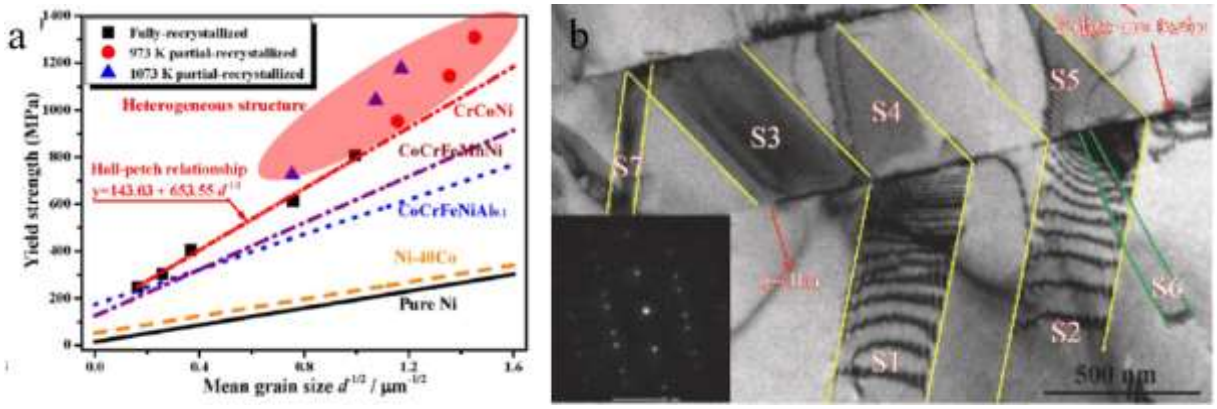

Fig. 1.17. (a) Mean grain against the yield strength of CrCoNi MEA compared to other FCC alloys [42]. (b) TEM micrograph showing dislocation transmission across the TB and reflection in original grain and the TB plane [99].

1.6. Thesis plan

In FCC and CrCoNi MEA, the initial stage of plastic deformation (incipient plasticity) occurs by nucleation of dislocations or motion of dislocations [29]. However, it is very difficult to investigate the incipient plasticity because macroscale mechanical tests such as tensile or compressive tests measure the average resistance of the whole material to deformation [43]. Using localized deformation techniques like instrumented nanoindentation, a small volume of a material can be probed [22]. The incipient plasticity appears as a displacement jump or a force drop on a load-displacement curve during a load-controlled or displacement-controlled nanoindentation test. It occurs when the maximum shear stress under a nanoindenter tip comes close to the theoretical shear stress. With this micro-mechanical response and the dislocation scale microstructure of dislocation obtained before and after deformation using electron channel contrast imaging [23], the origins and mechanisms responsible for incipient plasticity can be examined in fine detail.

An enormous variation in the resolved critical shear stress was observed in single crystals grown by the Bridgman method [100], [101]. The origin of such variations is still unknown. However, the analysis of the microstructural features such as low angle grain boundaries and how they

interact with dislocations produced by localized deformation by nanoindentation can shed some light on the origin of the variation of the critical resolved shear stress.

The CrCoNi MEA is a novel ternary alloy with superior properties to most HEAs and MEAs [75]. These properties have been associated with its low SFE and high shear modulus [19]. Low SFE promotes the formation of twins, which act as additional GBs. Generally, the Hall-Petch relation considers general HAGBs. However, this alloy has a high density of twins. To the best of our knowledge, one study looked at the Hall-Petch relation by considering TBs and argued that TB strengthening is as much as general HAGB strengthening [21]. However, there are limited studies on how individual GB contributes to the total strengthening in CrCoNi MEA.

Thus, this thesis will discuss the following questions:

- How do dislocation-based mechanisms control the incipient plasticity of CrCoNi MEA?
- How do incoming lattice dislocations interact with constituent intrinsic LAGB dislocations in a single crystalline CrCoNi MEA?
- How do incoming lattice dislocations interact at both TB and step in polycrystalline CrCoNi MEA?

2. Material and Methods

Abstract

Single crystalline and polycrystalline samples of CrCoNi MEA were used in the present thesis. Accurate Electron Channeling Contrast Imaging (A-ECCI) was used to image and characterize crystalline defects such as dislocations and stacking faults among others in CrCoNi MEA samples inside a scanning electron microscope. Instrumented nanoindentation test allows the introduction of plastic deformation in a small volume of materials at a precise location. Data from the test allows calculating hardness, young's modulus, and maximum shear stress at the onset of plasticity in CrCoNi alloy.

The numerical calculation-based superposition principle in linear elasticity was used to compute the stress field due to nanoindentation and dislocations. These calculations are critical for the quantitative assessment of the contribution of pre-existing dislocations to pop-in load during nanoindentation.

Furthermore, atomistic simulations were carried out to examine in detail the atomic-scale processes responsible for the pop-in both inside the grain and near a TB. Such molecular dynamics simulations are essential because the ex-situ experiments by A-ECCI do not provide the evolution of microstructure over time.

Résumé

Les échantillons monocristallins et polycristallins de l'alliage à moyenne entropie de CrCoNi ont été utilisés dans la présente thèse. L'ECCI a été utilisée pour imager et caractériser les défauts cristallins tels que les dislocations, les défauts d'empilement, les nanotwins, entre autres, dans les échantillons de l'alliage de CrCoNi à l'intérieur d'un microscope électronique à balayage (MEB). Le test de nanoindentation instrumenté permet d'introduire une déformation plastique dans un petit volume de matériaux à un endroit précis. Les données de l'essai permettent de calculer la dureté, le module de Young et la contrainte de cisaillement maximale au début de la plasticité dans l'alliage CrCoNi.

Un calcul numérique basé sur le principe de superposition en élasticité linéaire a été utilisé pour calculer le champ de contrainte dû à l'nanoindentation et aux dislocations. Ces calculs sont essentiels pour l'évaluation quantitative de la contribution des dislocations préexistantes à la charge de pop-in pendant la nanoindentation.

En outre, des simulations atomistiques ont été effectuées pour examiner en détail les processus à l'échelle atomique responsables du pop in à l'intérieur du grain et à proximité d'une macle. De telles simulations de dynamique moléculaire sont essentielles car les expériences ex-situ de l'A-ECCI ne fournissent pas l'évolution de la microstructure dans le temps

2.1. Introduction

The role of TEM in comprehensive dislocation scale imaging and characterization is incontestable. However, some drawbacks such as tedious and time-consuming thin-film sample preparation, artifacts introduced during such preparations, and a small viewable area make it difficult to investigate quantitatively localized deformation at specific microstructural features such as GB [102]. These difficulties are lessened by ECCI, which provides TEM-like diffraction contrast inside an SEM on a bulk specimen near the surface at a depth of ~150 nm deep with the phenomenon of electron channeling [26], [27], [56], [103]. The latter relies on electron backscatter diffraction (EBSD) to obtain the approximate orientation of the grain of interest. The high resolution-channeling pattern (HR-SACP) acquired in the zone of interest is overlayed on the simulated Kikuchi pattern to index pattern [104].

Macroscale mechanical properties tests such as tensile or compressive tests measure the average resistance of the whole material to deformation. Such tests make it challenging to investigate the individual contribution of microstructural features such as GB on the overall macroscopic strength, such as individual grain boundaries. Thus, deformation at a specific location is performed using instrumented nanoindentation to induce mechanical response near pre-defined and localized areas of the microstructure [105].

During nanoindentation, a nanoindenter is introduced into the sample with a certain stress field. The latter is amplified by defects such as dislocations. However, it is very difficult to quantify how much this stress field is amplified from the experiment. Thus, a numerical calculation based on elasticity theory is used to investigate the contribution of dislocations during deformation using nanoindentation [28], [106].

Atomistic simulations have been used to dynamically examine how nucleated dislocations interact with a twin boundary. They were performed using a Large-scale Atomic/Molecular Massively Parallel Simulator (LAMMPS) employing the atom embedded method for the CrCoNi MEA.

This chapter gives a brief overview of the material and experimental techniques used to investigate the evolution of microstructure and micromechanical response in monocrystalline and polycrystalline CrCoNi MEA samples.

2.2. The ternary CrCoNi medium entropy alloy

2.2.1. Processing methods

Guillaume Laplanche (ZGH, Institute for Materials, Ruhr-Universität Bochum, Universitätsstr. 150, 44801 Bochum) provided the monocrystalline and polycrystalline samples. This section provides a superficial overview of how the samples were processed since it is not the topic of this thesis. For details, the reader should look at the articles by Laplanche *et. al.* [19], [21], [107].

The single crystal was grown by a Bridgman technique employing a CMSX-4 type superalloy seed because the latter has the same structure and lattice parameters as CrCoNi MEA [108], [109]. A mixture of pure Cr, Co, and Ni (≥ 99.9 wt. %) was melted in the vacuum induction furnace at a temperature above the melting point of CrCoNi MEA of 1690 K. It was held above this temperature for 1 hour and 20 minutes. It was then withdrawn at a rate of 180 mm/h. Interested readers can find further details on the processing of the single crystalline ternary CrCoNi MEA in refs. [107] and on the Bridgman method [110].

The polycrystalline CrCoNi MEA was prepared in four successive steps. The first step involved melting pure constituent elements (purity ≥ 99.9wt %) in a vacuum induction furnace. The second step involved homogenization at 1473 K for 48 hours in an evacuated quartz tube and air-cooled to room temperature. The third step involved rotary swaging using a four die rotary swaging machine of type HMP R6-4-120-21S (HMP Umformtechnik GmbH, Pforzheim, Germany) in seven steps at room temperature to reduce the diameter from 40 mm to 16.5 mm. The final step was recrystallization at 1273K in air for 1 hour. The interested reader should consult Ref. [83] for further details on how the sample was produced.

2.2.2. Sample preparation

Cylindrical samples were cut and mounted in a resin for an easy grip during coarse grinding. The latter was done using various SiC papers using water as a lubricant. Fine grinding was successively carried out using the colloidal diamond suspension of 9 µm, 3 µm, and 1 µm. The sample was cleaned with soap and ethanol at each step. It was checked with an optical microscope to observe the extent of scratches and contaminants at the surface before chemo-mechanical polishing using an oxide polishing suspension. After this step, the observation of dislocations was still impossible with ECCI. Thus, the sample was polished with a solution of

a two-third oxide polishing suspension and one-third of hydrogen peroxide for half an hour to improve the surface quality. It was later ultrasonically cleaned for 5-10 minutes in a 96% solution of ethanol.

2.3. Experimental techniques

2.3.1. Scanning electron microscopy

The interaction of a beam of electrons and the specimen is the basis of SEM-based techniques. The beam of electrons is generated by a source (*e.g.*, a field emission gun) and is passed across a series of electromagnetic lenses to enhance it. It later interacts with the atoms of the specimen and produces different signals used to image various features of the microstructure and analyze chemical composition (Fig. 2.1). Secondary electrons (SE) are used to image the topography of the surface, backscattering electrons (BSE) imaging provides either phase or orientation contrast, and x-rays are used for chemical analysis [111]. Other signals include auger electrons, cathodoluminescence, electron beam induced current, and so forth [111]. SE and BSE micrographs were acquired using a Zeiss AURIGA field emission gun focused ion beam SEM (FIB-SEM) and Zeiss Supra 40 (Oberkochen, Germany). The accelerating voltage and working distance range were 10 kV to 20 kV and 5 mm to 10 mm, respectively. Post-processing of micrographs was carried out using ImageJ.

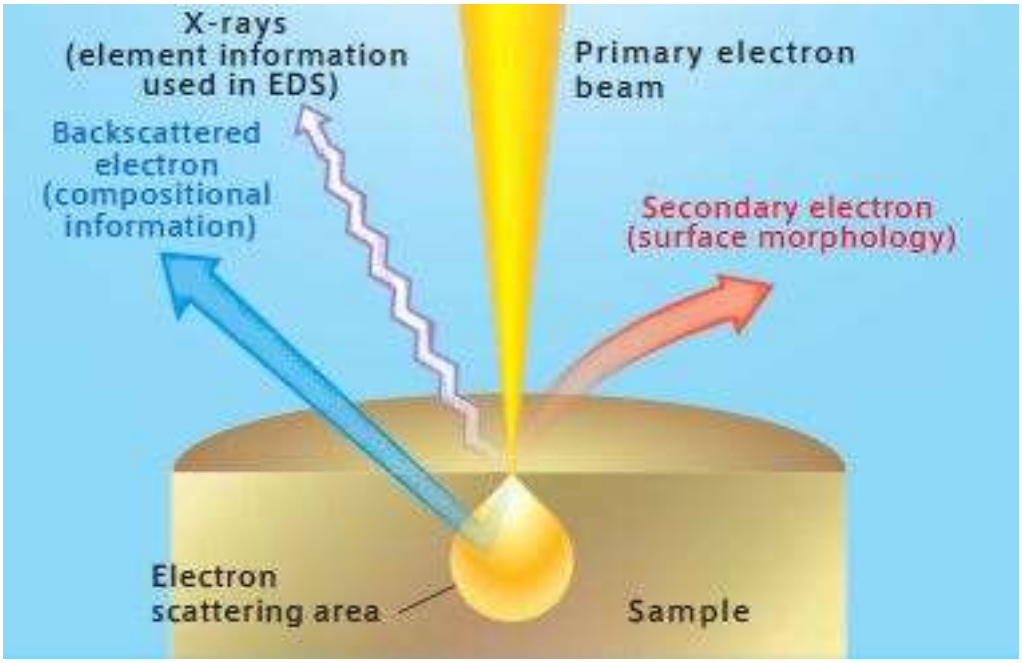

Fig. 2.1. Different emitted signals by bulk sample due to incoming electrons hitting the bulk sample in an SEM.

2.3.2. Energy dispersive x-rays spectroscopy

Energy dispersive x-ray spectroscopy (EDS) is an SEM-based technique that is used to perform chemical microanalysis of bulk specimens [112]. It employs a high-energy beam of electrons to bombard the sample. The electrons of the beam either are decelerated by the atomic nuclei or cause ionization of the inner shell electrons of surface atoms. The deceleration of electrons is responsible for the x-ray continuum (or background noise), whereas the ionization of the inner shells is responsible for peaks. In the latter, the incoming electron knocks out the inner shell electron leaving a hole. Subsequently, an electron from the outer shell fills the hole. The filling of an electron-hole emits characteristic x-rays whose energy depends on the nature of atoms present in the specimen. Figure 2.2 displays a K-shell electron of an atom being dislodged by a primary electron. Then, an L_3 subshell electron fills the electron vacancy with a generation of K-L_3 ($K_{\alpha 1}$) characteristic x-rays [113]. The energy of characteristic x-ray lines for most elements is less than 10 keV.

It suggested that the energy used to knock out elements should be at least 2.5 times the energy of characteristic x-rays of the elements [113]. Thus, SEM operating at 20-30 kV can analyze most of the elements. Qualitative analysis, *i.e.*, determination of elements present in the specimen, measures the energy of each characteristic x-rays. On the other hand, quantitative analysis, *i.e.*, the composition of each element, estimates the number of characteristic x-rays of any type emitted per second.

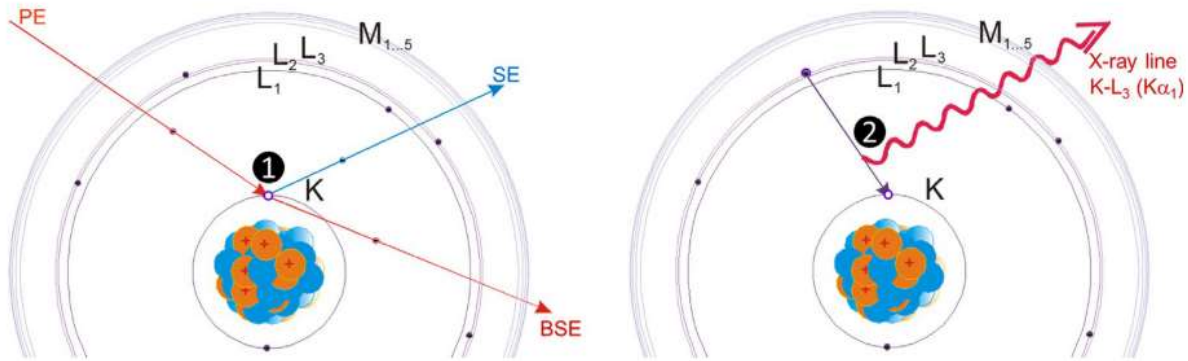

Fig. 2.2. A primary electron dislodges a K-shell electron of an atom in the specimen. An electron from the L_3 subshell shell fills the K-shell's electron vacancy, followed by a generation of $K_{\alpha 1}$ characteristic x-rays [113].

EDS maps and points for compositional analyses of the single crystal analysis were acquired using an SEM of type JEOL JSM-IT 300 equipped with an Octane Elite EDAX Ametek detector and the analytical software EDAX Genesis (v.6.53) (experiment and analysis of these EDS data were carried out by Guillaume Laplanche and co-workers). They were acquired with an accelerating voltage of 25 kV combined with a probe current of 60 mA, a working distance of ~10 mm, and a count rate of ~150.000 counts/s. A total number of 1024 frames were collected, resulting in a full recording time of ~10 h.

The elemental distribution maps of the sample of the polycrystalline CrCoNi MEA employed an SEM of type Zeiss Supra 40 (Oberkochen, Germany) equipped with Quantax Bruker EDS X-flash 5100 detector and Bruker ESPRIT software (2.0). They were acquired using an accelerating voltage of 20 kV, an aperture size of 60 μm, and a working distance of 10 mm.

2.3.3. Electron backscatter diffraction

Electron backscatter diffraction (EBSD) is an enhanced SEM-based technique used to study grain morphology, determine the crystal orientation and characterize the GBs, etc [114]–[116]. This technique relies on EBSD patterns. An optimum intensity of EBSD patterns is obtained when the specimen is tilted by 70°, *i.e.*, an angle of 20° between the incoming electron beam and the specimen surface. The formation of the EBSD patterns relies on Bragg's law:

$$n\lambda = 2d_{hkl}\sin\theta \quad (2.1)$$

Where n is the order of diffraction, λ is the wavelength of the incoming electron beam, d_{hkl} is the interplanar spacing of (hkl) planes, and θ is the diffraction angle. In the material, electrons scatter when the incoming beam strikes the specimen. However, there are always electrons arriving at Bragg's angle (θ_B) for a set of lattice planes. Each lattice plane produces two diffracting cones. The intersection of diffracted cones with the phosphor screen of the EBSD camera produces pairs of parallel lines or Kikuchi lines with the angular spacing of $2\theta_B$ (Fig. 2.3). These bands are projected lattice planes and their angular relationship provides crystallographic information about the sample.

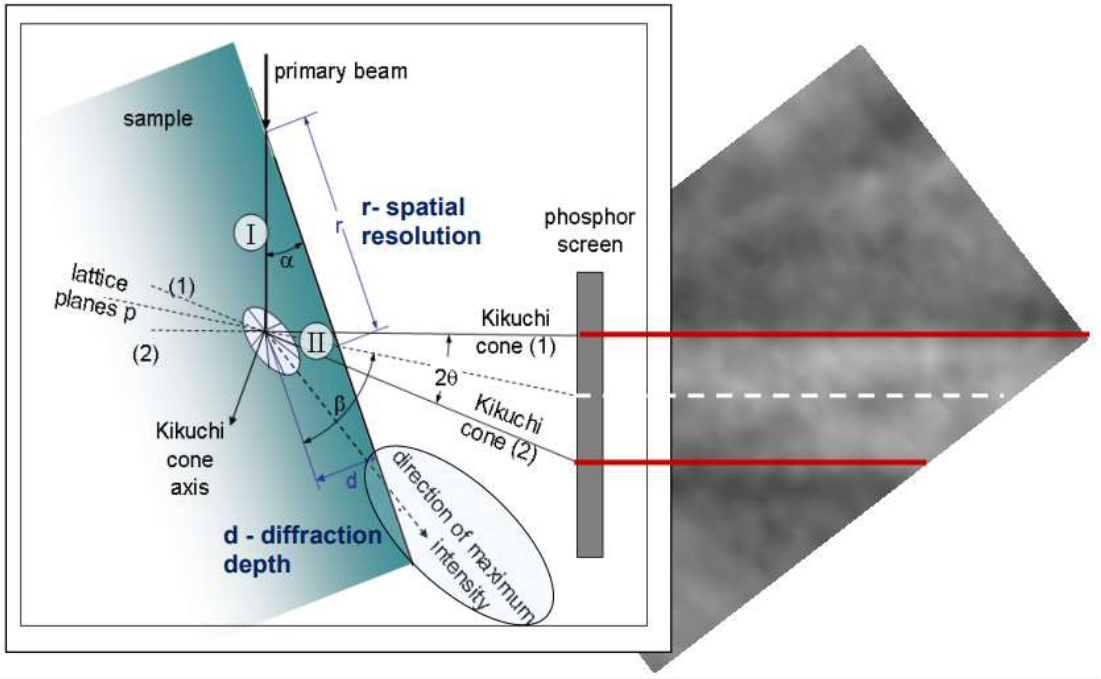

Fig. 2.3. Origin of Kikuchi lines from the EBSD (i.e., tilted specimen) perspective [117].

Current EBSD systems can have an excellent spatial resolution as low as ~ 25 nm depending on the direction parallel to the scanning or perpendicular due to the inclination of the sample relative to the incident beam [118]. The angular resolution as low as 0.5° is attainable with conventional EBSD and can be less using high-resolution electron backscatter diffraction (HR-EBSD). EBSD maps were acquired with a commercial EBSD system, Aztec (Oxford Instrument, Inc., UK), using an acceleration voltage of 20 kV, an aperture size of 120 µm, and a working distance between 10-15mm inside a Zeiss AURIGA FIBSEM (Oberkochen, Germany). The range of step size was 200 to 1000 nm. The EBSD maps were processed employing both the HKL Channel 5 (Oxford Instrument, Inc., UK) and ATEX (LEM3, France) [119] software packages.

2.3.4. Electron channeling contrast imaging

ECCI is the SEM-based technique that is used for imaging and analysis of crystallographic defects such as dislocations, stacking faults, etc., near the surface of polished bulk specimens inside the SEM [23], [24], [26], [56]. It is Coates [120] who stumbled upon Kikuchi-like patterns superimposed on a backscattered electron (BSE) image. Besides, he observed a strong dependence of BSE yield on the orientation of crystal lattice planes relative to the incident electron beam in bulk samples of single-crystal semiconductors using SEM at low magnifications. These patterns were theoretically interpreted by Booker *et al.* [121] who

demonstrated and concluded that the detection and measurement of variation in BSE yield could contrast defects such as dislocations because the lattice bending around such defects modulate the BSE yield. In 1972, dislocations were observed for the first time in the SEM [122], [123]. Even if dislocations were observed in the 70s, ECCI was not practical because the electron gun did not have adequate brightness. The recent development of field emission gun SEM (FEG-SEM) with a high spatial resolution of ~2 nm, small electron beam convergence, high current density, and small beam diameter has revived the interest in ECCI.

2.3.4.1. Accurate ECCI

Classical ECCI on monocrystalline or polycrystalline samples with grains larger than 2 mm relies on an electron-channeling pattern (ECP) to set up channeling conditions. For polycrystalline material with grains larger than 50 μm but less than 2 mm, a selected area channeling pattern obtained by rocking beam is used [104]. Thus, ECP and SACP are used for setting channeling conditions for coarse grains.

The development of a high-resolution selected area channeling pattern (HR-SACP) with a spatial resolution of 500nm and angular range of ~ 4° has allowed studying defects in fine-grained materials and highly strained materials [56], [103], [104]. Mansour *et al.* [23] used the HR-SACP overlaid on a simulated EBSD pattern to index the bands accurately and then tilted and rotated the sample to precisely and accurately align the incident electron beam around a specific band edge to set various channeling conditions. This combination of simulated EBSD pattern and HR-SACP precisely enables controlling the orientation of an incident beam relative to the crystal lattice planes with an accuracy of 0.1°. Thus, such a way of carrying out ECCI was termed accurate ECCI (A-ECCI). Note that there are other variants of ECCI such as rotational ECCI [124].

Many micrographs at different diffraction vectors (**g**) can be acquired making it possible to apply the invisibility criteria like in TEM to characterize dislocations and stacking faults: $\mathbf{g} \cdot \mathbf{b} = 0$ and $\mathbf{g} \cdot \mathbf{b} \times \mathbf{u} = 0$ and $\mathbf{g} \cdot \mathbf{R} = 0$ where $\boldsymbol{u}$ is a unit vector along the dislocation line and **R** is the fault vector [23], [27]. This technique was thus used to analyze the Burgers vector and line direction of dislocations in interstitial free steel using TEM-based extinction criteria [23]. It was also used to calculate the misorientation angle of low angle tilt boundary based on dislocation that made it in the steel [26] as well as dislocation network on sub-boundaries in deformed uranium oxide under creep [56]. Moreover, it was used to characterize dislocations

and their interaction with twin boundaries during the evolution of deformation produced by localized nanoindentation in the γ-TiAl-based alloy [24].

2.3.4.2. Setting up channeling conditions for A-ECCI

EBSD map and HR-SACP were employed for setting up the channeling conditions as well as ECCI micrographs were acquired on Zeiss Auriga FIB-SEM (Oberkochen, Germany). Firstly, an EBSD map was taken in the region of interest to obtain the relative crystallographic orientation of the grains in terms of three Euler angles (φ_1, Φ, φ_2). These Euler angles were used to simulate the EBSD patterns at 0° with an angular error of 2° since ECC micrographs are acquired at 0°. The dynamically simulated patterns were obtained using Esprit Dynamics software from Bruker. Secondly, HR-SACP with an angular range of 4.4° and spatial resolution of 500 nm is collected by the rocking beam approach on the GEMINI-type FEG-SEM electron column as described in the paper by Guyon *et al.* [104]. The parameters for acquiring the HR-SACPs were a working distance of 6.2 mm, an accelerating voltage of 10 and 20 kV, a 60 μm aperture size, and an 11 mm^2 four-quadrant Si-diode backscattered electron detector. Thirdly, the HR-SACP was superimposed on a simulated EBSD pattern to accurately and precisely determine the position of the optical axis to the Kikuchi bands with respect to the incoming electron beam (*i.e.,* the optical axis of the microscope). Finally, the sample was tilted and rotated to go at the edge of various bands to set different two-beam channeling conditions. In this thesis, the rotation and tilt angles range from 0 to 360° and 0 to 12°, respectively. Once the channeling condition, ECC micrographs were acquired at high magnification using a range of voltage from 10 to 20 kV, aperture of 60 μm and 120 μm as well as a working distance of 6.2 mm.

2.3.5. Instrument nanoindentation

Instrumented nanoindentation experiments were employed to measure small-scale mechanical properties such as hardness, Young's modulus, fracture toughness, etc. [125], [126]. Moreover, they offer incontestable capabilities of probing mechanical response at precise sample locations from very small volumes of materials [22]. During the nanoindentation test, a nanoindenter is placed in contact with the surface of the material being studied, and the load-displacement (P-h) is recorded, among other curves. The load on the nanoindenter and displacement of the nanoindenter are minimal and range from mN to μN and μm to nm, respectively.

The nanoindentation experiments on a single crystal employed a sharp Berkovich nanoindenter tip (Synton-MDP AG, Switzerland) inside the Hysitron TI-900 nanoindentation machine

(Bruker, US) (Fig. 2.4). These experiments were done in collaboration with researchers in the Department of Materials Science and Engineering at the University of Saarbrucken, Germany. The precise nanoindentation test placement near a LAGB (not observable with an optical microscope) was accomplished with the help of an *in-situ* scanning probe microscope available in TI-900 (the probe allows a scan of the area of interest before nanoindentation). The nanoindentation experiments on the polycrystalline sample were carried out using Ultra Nanoindentation Tester from Anton Paar (Buchs, Switzerland), equipped with a Berkovich nanoindenter.

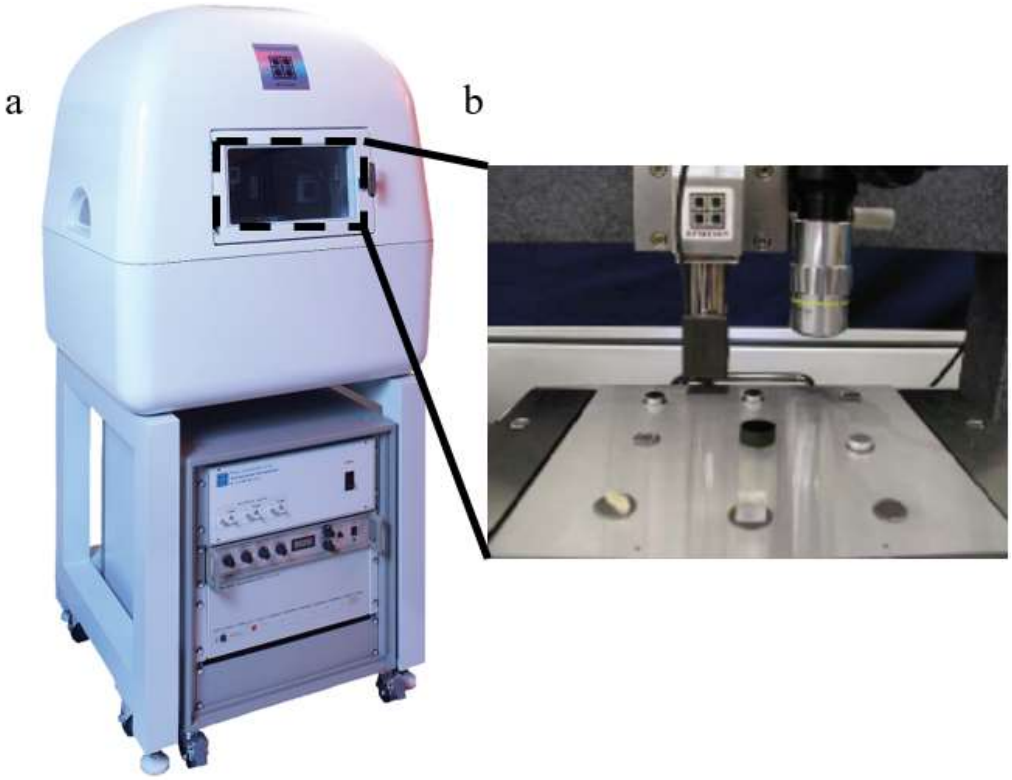

Fig. 2.4. (a) The acoustic/thermal enclosure of the TI-900 TriboNanoindenter, (b) inside TI-900, shows a multiple sample stage along with probes.

2.3.5.1. Analysis of a nanoindentation curve

Various methods such as the ones proposed by Doerner and Nix [127], Oliver and Pharr [125], [126], Woirgard and Dargenton [128] as well as Field and Swan [129] are used to analyze nanoindentation curves and data. This section briefly summarizes the method of Oliver and Pharr for the determination of mechanical behavior and properties of materials at small scales without imaging hardness impression [125], [126]. This method assumes that the material undergoes only elastic deformation during unloading and that no adhesion and frictional

stresses are acting between the surfaces and relies on the parameters that are shown in Figs. 2.5-6. The slope at the start of the unloading curve ($\frac{dF}{dh}$) gives the stiffness (S) as:

$$S=\frac{dF}{dh} = 2\beta E_r \sqrt{\frac{A_c}{\pi}} \tag{2.2}$$

Where β is a constant that expresses non-axisymmetry of the nanoindenter (β =1.034 for Berkovich tip), A_c is the contact area at the peak load and E_r is the reduced modulus. The calculation of A_c is dependent on the nanoindenter tip geometry and depth of contact (h_c) and is given by an area function for a perfect Berkovich of the form:

$$A_c = 24.5h_c^2 \tag{2.3}$$

The value of h_c is obtained from the experimental data using the relation:

$$h_c= h_{max} - \epsilon \frac{P_{max}}{S} \tag{2.4}$$

Where ϵ is the geometrical constant for the nanoindenter and P_{max} is the peak load. The detailed derivation of Eq. 2.4 can be found in ref. [125]. The obtained E_r from Eq. (2.2) is used to obtain Young's modulus of the sample (E_s) given that Young's modulus and Poisson's ratio of the nanoindenter (E_i and ν_i), as well as the Poisson's ratio of the sample (ν_s), are known from the relation:

$$\frac{1}{E_r}= \frac{1-\nu_i^2}{E_i} + \frac{1-\nu_s^2}{E_s} \tag{2.5}$$

Moreover, the hardness (H) can also be calculated using the relation:

$$H = \frac{P_{max}}{A_c} \tag{2.6}$$

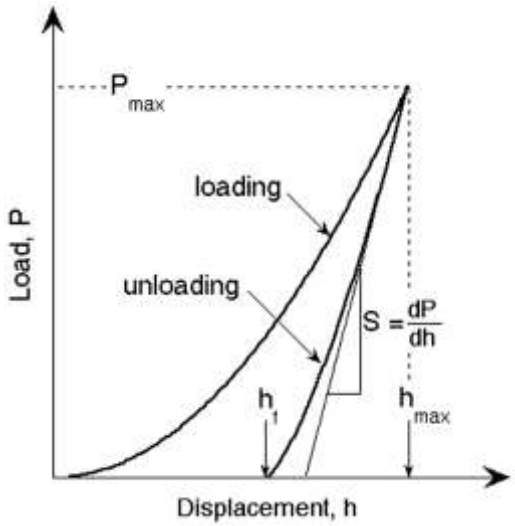

Fig. 2.5. Nanoindentation load-displacement curve with important measured parameters [125].

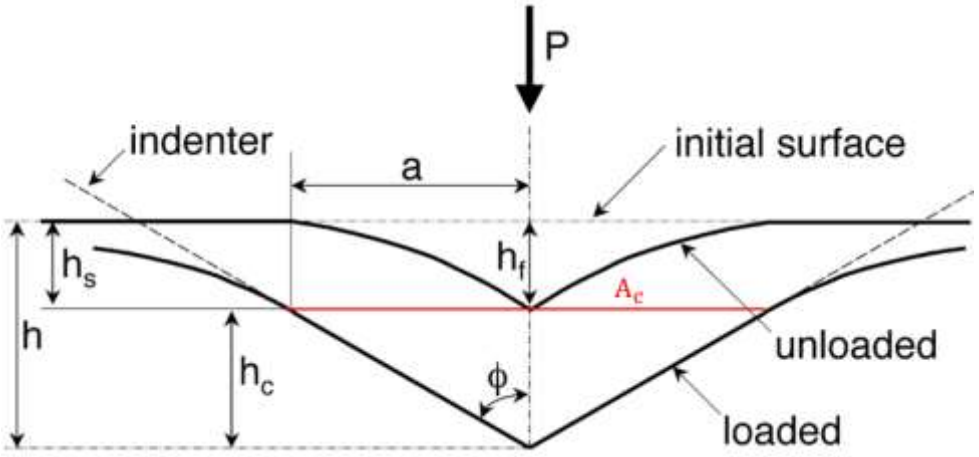

Fig. 2.6. Schematic of the unloading process with parameters characterizing the contact geometry [125], [126].

2.3.5.2. Pop-in in metallic materials.

In metallic materials, the initial contact of the nanoindenter and the sample is purely elastic and can be quantified using Hertz contact theory between a spherical body and an elastic half-space expressed as:

$$P = \frac{4}{3} E_r \sqrt{R h^3} \tag{2.7}$$

Where R is the radius of the nanoindenter. At some point, as the load increases, the material undergoes irreversible plastic deformation that appears as "a jump in displacement," also known as "an initial pop-in" in a load-controlled test (Fig. 2.7a) [130], [131]. Note that the displacement-controlled is the jump in force. The initial pop in occurs when the maximum shear stress underneath the nanoindenter (τ_{max}) exceeds a critical value as shown:

$$\tau_{max} = 0.31 \times \left(\frac{6 \times (E_r)^2}{\pi^3 R^2} \times P_{pop}\right)^{\frac{1}{3}} \tag{2.8}$$

where P_{pop} is the load at the pop-in. The values of τ_{max} were found to be in the range of the theoretical shear stress (τ_{th}), *i.e.*, between G/25 and G/5, where G is the shear modulus [132]–[134]. For example, the calculated τ_{max} of 1.8 GPa in Al was in the range of τ_{th} [135]. Thus, the initial pop-in was mainly linked to nucleation of dislocations in metallic materials [136]–[139]. Indeed, Zhou *et al.*[140] observed the initial pop-in and nucleation of half prismatic dislocation loops in defect-free single crystals of Al using molecular dynamics (MD) simulations. Some material's initial pop-in is followed by small multiple pop-ins [139], [141]. The subsequent small pop-ins were linked to various mechanisms such as dislocation multiplication or motion [139].

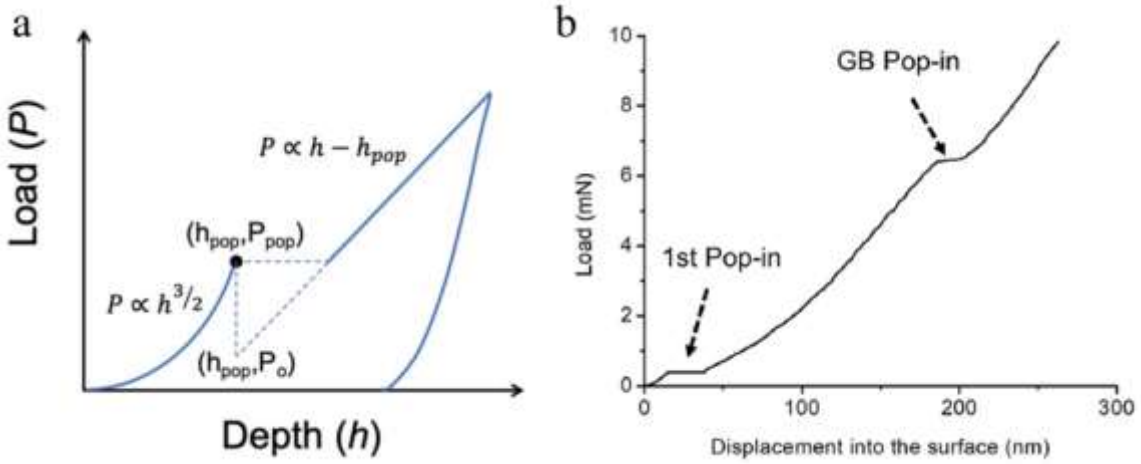

Fig. 2.7. (a) P-h curve with the initial pop-in [130]. (b) P-h curve showing both initial pop-in and GB pop-in [142].

However, both experimental and numerical studies agreed that nanoindentation near a GB produces a large GB pop-in in addition to the initial pop-in (Fig. 2.7b). Javaid *et al.* [143] carried out a nanoindentation test near a GB with 57° of misorientation between adjacent grains in tungsten and observed two large pop-ins. ECC micrographs revealed the transmission of dislocations which he associated with the secondary GB pop-in. Similarly, Lu *et al.* [144] employed 3D multiscale modeling coupling discrete dislocation dynamics (DDD) and finite element methods (FEM) and observed initial pop-in due to activation of dislocation and GB pop-in due to the transmission of dislocation across the boundary [145].

2.4. Numerical calculations based on elasticity theory

The elasticity calculations based on the superposition principle in linear elasticity were used to calculate the stress field due to both nanoindent and dislocations. They provide the influence of different dislocation configurations on the maximum shear stress necessary to initiate plasticity.

2.4.1. Stress field under the axisymmetric nanoindenter

During nanoindentation loading, the stress field arising from the contact between the nanoindenter and the sample surface (*i.e.*, the stress field underneath the axisymmetric nanoindenter) is determined using the contact mechanics-based equations 3.19 of Johnson [106] that describes a point load applied on elastic half-space as found in ref. [146] under the assumption of linear isotropic elasticity.

Given that $r = \sqrt{x^2+y^2}$ and $p = \sqrt{x^2+y^2+z^2}$ in Fig. 2.8, the components of stress in Cartesian coordinate are given by the following expressions:

$$
\begin{aligned}
\sigma_{xx} &= \frac{P}{2\pi}\left[\frac{1-2\upsilon}{r^2}\left\{\left(1-\frac{z}{p}\right)\frac{x^2-y^2}{r^2}+\frac{zy^2}{p^2}\right\}-\frac{3zx^3}{p^5}\right] \\
\sigma_{yy} &= \frac{P}{2\pi}\left[\frac{1-2\upsilon}{r^2}\left\{\left(1-\frac{z}{p}\right)\frac{y^2-x^2}{r^2}+\frac{zy^2}{p^2}\right\}-\frac{3zy^3}{p^5}\right] \\
\sigma_{zz} &= \frac{3P}{2\pi}\frac{z^3}{p^5} \\
\tau_{xy} &= \frac{P}{2\pi}\left[\frac{1-2\upsilon}{r^2}\left\{\left(1-\frac{z}{p}\right)\frac{xy}{r^2}-\frac{xyz}{p^3}\right\}-\frac{3xyz}{p^5}\right] \\
\tau_{xz} &= -\frac{3P}{2\pi}\frac{xz^2}{p^5} \\
\tau_{yz} &= -\frac{3P}{2\pi}\frac{yz^2}{p^5}
\end{aligned}
\qquad (2.9)
$$

The stress field due to the nanoindentation test induces elastic deformation. Thus, they are described by these equations. Continuous loading will result in the stress reaching the maximum shear stress, inducing other deformations such as plastic deformation. The maximum shear stress can be obtained from the experiment from the load to pop-in, as shown in Eq. 2.8.

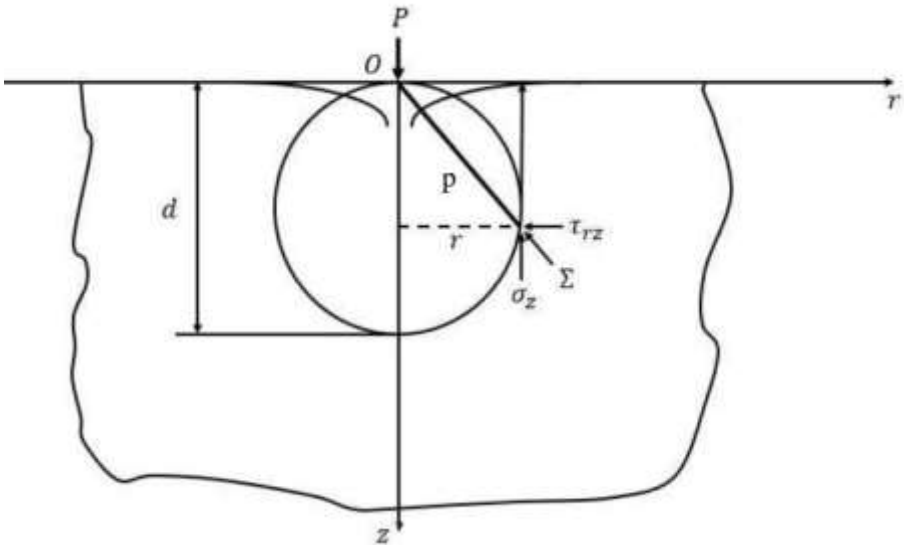

Fig. 2.8. Loading to the point load at O

2.4.2. Stress field due to dislocation

A dislocation elastically distorts a perfect crystal lattice. Thus, it introduces an internal stress field in the surrounding lattice sites. The magnitude of this stress field has been simplistically determined using conventional linear elasticity theory for isotropic and continuous medium [29]. For a simple case of an infinitely-long screw dislocation shown in Fig.2.9a formed by cutting a radial slit LMNO parallel to the z-axis and displacing it by b along the z-axis, the displacement occurs only in z-directions and increase from 0 to b as θ increases from 0 to $2\boldsymbol{\pi}$:

$$u_x = u_y = 0 \tag{2.10}$$

$$u_z = \frac{b}{2\pi} \tan^{-1}\left(\frac{y}{x}\right)$$

The first derivative of the components of displacement gives only four components of strain (others are zero), which are used in Hooke's law to obtain the four components of stress:

$$\sigma_{xx} = \sigma_{yy} = \sigma_{zz} = \sigma_{xy} = \sigma_{yx} = 0$$

$$\sigma_{xz} = \sigma_{zx} = -\frac{Gb}{2\pi} \frac{y}{(x^2+y^2)} \tag{2.11}$$

$$\sigma_{xz} = \sigma_{zx} = \frac{Gb}{2\pi} \frac{x}{(x^2+y^2)}$$

For an infinitely-long edge dislocation shown in Fig. 2.9b formed by cutting a radial slit LMNO parallel to Z-axis and displacing it by b along the x-axis, the same procedure used for the screw dislocation is applied, and the component of stress are:

$$\sigma_{xz} = \sigma_{zx} = \sigma_{yz} = \sigma_{zy} = 0$$

$$\sigma_{xx} = -\frac{Gb}{2\pi(1-\upsilon)} \frac{\left(3x^2+y^2\right)}{(x^2+y^2)^2}$$

$$\sigma_{yy} = -\frac{Gb}{2\pi\,(1-\upsilon)} \frac{(x^2-y^2)}{(x^2+y^2)^2} \tag{2.12}$$

$$\sigma_{zz} = -\frac{Gb}{2\pi\,(1-\upsilon)} \frac{(x^2-y^2)}{(x^2+y^2)^2}$$

$$\sigma_{xz} = \upsilon\,(\sigma_{xx} + \sigma_{yy})$$

Since $x^2 + y^2 = r^2$, the stresses and strains are proportional to $\frac{1}{r}$ *i.e.,* they diverge to infinity when r tends to zero. Therefore, linear elasticity theory does not apply near the dislocation center, also called the dislocation core radius. Consequently, a hole of radius r_0 is drilled in the

cylinder (Fig. 2.9) for the sake of calculations. The values of r_0 are assumed to be in the range of b to 5b [29].

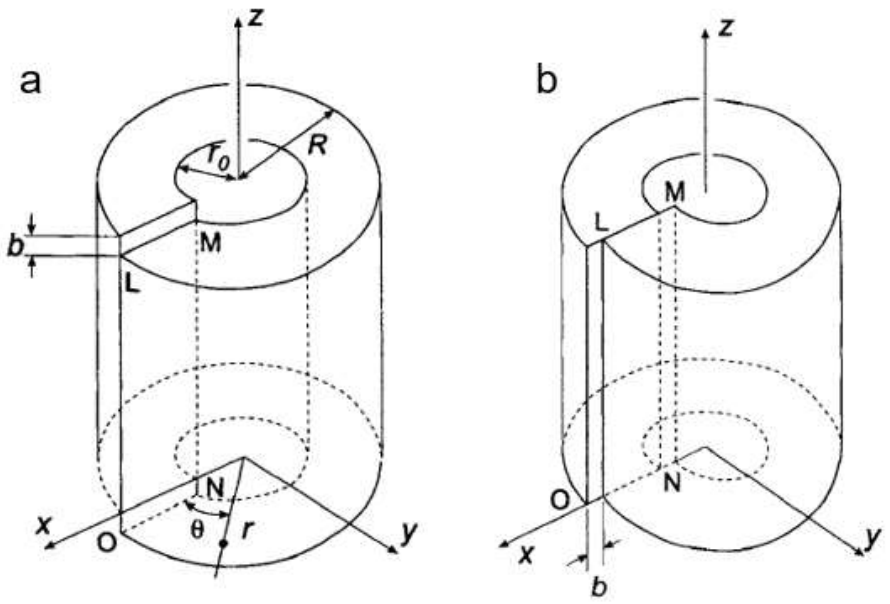

Fig. 2.9. (a) Elastic distortion of a cylindrical ring simulating the distortion produced by a screw dislocation. (b) Elastic distortion of a cylindrical ring simulating the distortion produced by an edge dislocation [29].

2.5. Atomistic simulation

Atomistic simulation is a numerical method based on the discretization of materials at the atomic scale [147]. There are two categories of atomistic simulations: molecular statics and molecular dynamics. Molecular statics rely on numerical optimization methods to find the minimum potential energy of the simulation model at 0K [148]. The lowest energy system is obtained using a minimizing algorithm such as conjugate gradient [149]. The molecular statics' calculation makes it possible to extract, e.g., the crystal lattice structure of phases such as cohesive energy and lattice parameter under different conditions such as strain and stress.

Alternatively, molecular dynamics (MD) simulate the evolution of atomic position over time following Newton's second law of motion [147]. The positions of atoms are varied with the atomic velocities by incorporating the temperature and time parameters into a simulation cell. Thus, this type of simulation can predict the evolution of a system during the deformation test. One of the most used deformation tests is the nanoindentation test. Atomistic simulations using nanoindentation as a deformation test have been used extensively to investigate elementary plastic deformation mechanisms in different materials. For example, it has been used to

investigate incipient plasticity in Al [150], [151] and nanocrystalline Fe [41], nucleation, and evolution of dislocations in CrCoNi MEA [152]. The computation of the atomic interactions is fundamentally in molecular statics and dynamics. It allows obtaining the force applied to each atom, and this is obtained by the use of interatomic potential [153].

2.5.1. Molecular statics

In molecular statics, energy minimization algorithms are employed to produce a system with the minimum potential energy at absolute zero temperature. The easiest way to obtain a system with the lowest energy is to minimize the energy by nullifying the force acting on each atom. The system is relaxed when the derivative of the potential energy to the atomic displacements is zero. Such a condition implies that the forces acting on the atoms are below a predefined value (or zero in an ideal case). Consequently, atomic velocity is zero.

The lowest energy system is achieved using different various iterative minimization algorithms. Among these algorithms, the conjugate gradient (CG) algorithm has proven efficient for achieving convergence rapidly for large systems [149]. The CG, as is the case for other iterative line search minimization algorithms, displaces the atoms that are within the simulation box to find the lowest energy state. A system configuration (R_k) at iteration k is adjusted by $\alpha_k D_k$ to reduce the energy of the system during linear search minimization as given by the relation:

$$R_{k+1} = R_k + \alpha_k D_k \tag{2.13}$$

Where α_k is the step size and D_k is the search direction. In the CG, the search direction is chosen based on all prior iterations, ensuring that oscillations are avoided at the energy minima. The conjugate gradient algorithm of Polak-Ribiere [149] was used in this study as implemented in the LAMMPS code. In our numerical simulation, the system of atoms is relaxed when the energy between two successive adjustments, divided by the energy of the system, is less than a dimensionless stopping criterion, E_{stop}:

$$E_{stop} = \frac{E_k - E_{k-1}}{E_k} \tag{2.14}$$

E_{stop} was set to 10^{-6} for our atomistic simulations [149].

2.5.2. Molecular dynamics

Unlike the static method, MD simulations take into account the kinetic energy of the atoms. Thus, the dynamic evolution of atoms' positions and velocities is obtained over time using

Newton's second law of motion [148]. The knowledge of forces acting on atoms allows us to find these atoms' acceleration through fundamental dynamics. After an interval time knowing its position, the velocity and atoms' position are deduced from the obtained acceleration. The timestep (Δt) is an essential parameter in MD simulations. The calculation is needlessly long and has significant numerical rounding errors when Δt is small. In contrast, the calculated trajectory moves away from the natural trajectory when Δt is large, *i.e.*, simulations become unstable and diverge. In this study, MD simulations used Δt of 0.001 ps since the material is a metallic alloy at room temperature.

Verlet algorithm incorporated into LAMMPS code integrates Newton's equations numerically. It is based on writing the third-order Taylor developments of the atomic positions, **r**, at timesteps t - Δt and t + Δt [148]:

$$\mathbf{r}(t + \Delta t) = \mathbf{r}(t) - \dot{\mathbf{r}}(t)\,\Delta t + \frac{1}{2}\ddot{\mathbf{r}}(t)\,\Delta t^2 - \frac{1}{6}\dddot{\mathbf{r}}\,\Delta t^3 + O\,\Delta t^4 \quad (2.16)$$

$$\mathbf{r}(t + \Delta t) = \mathbf{r}(t) - \dot{\mathbf{r}}(t)\Delta t + \frac{1}{2}\ddot{\mathbf{r}}(t)\,\Delta t^2 + \frac{1}{6}\dddot{\mathbf{r}}\Delta t^3 + O\,\Delta t^4 \quad (2.17)$$

where $O\,\Delta t^4$ is the error term. The positions of atoms at t + Δt can be obtained from the positions at t and t – Δt:

$$\mathbf{r}(t + \Delta t) = 2\mathbf{r}(t) - r(t-\Delta t) + \ddot{\mathbf{r}}(t)\,\Delta t^2 + O\,\Delta t^4 \quad (2.18)$$

The acceleration, $\ddot{\mathbf{r}}(t)$, experienced by each atom is obtained from Newton's second law with m as mass and V as the interatomic potential:

$$\ddot{\mathbf{r}}(t) = -\frac{1}{m}\,\nabla V[r(t)] \quad (2.19)$$

Although it is not required to know the velocity of the particles to find new positions, its knowledge is vital to determine the thermodynamic quantities of the system, such as kinetic energy, temperature, etc. The velocities, $\dot{\mathbf{r}}(t)$, of the atoms are thus deduced from their successive positions using the relation:

$$\dot{\mathbf{r}}(t) = \frac{r(t+\Delta t) - \mathbf{r}(t-\Delta t)}{2\Delta t} + O\Delta t^2 \quad (2.20)$$

2.5.3. Interatomic potential

Interatomic potentials describe the atomic interactions in the systems and thus determine the behavior of a system. The pair potentials such as Lennard-Jones, Morse, and coulombic

potentials are appropriate for interactions of molecules in a gas [147]. These simple pair potentials cannot describe complex atomic interactions in solid materials such as metals and alloys. Therefore, Daw and Baskez [154] developed the embedded atom method (EAM) potential to describe the interatomic interactions of metal and alloys using the density functional theory (DFT). The latter calculates the interatomic forces based on the quantum mechanisms, and the potential is determined by an electric field formed by the distribution of nuclei and electron charges. The EAM potential is semi-empirical potential (*i.e.*, parameters fitted to experiment and DFT). The total energy of atom i using EAM (E_i) determined from:

$$E_i = F_\alpha \left(\sum_{i \# j} \rho_\beta (r_{ij}) \right) + \frac{1}{2} \sum_{j \# i} \varphi_{\alpha\beta} (r_{ij}) \tag{2.21}$$

where F_α is the embedding energy, *i.e.*, the energy required to embed an atom type α at a position of atom (i) with a local electron density, ρ_α, due to the neighboring atoms, φ is an interaction pair potential between atom i and neighboring atom j, α and β are the element types of atoms i and j, r_{ij} is the distance between atoms i and j. In this study, the interactions of the atoms are enabled by the EAM potential developed by Li et al. [155].

2.5.4. Analysis and visualization of atomic data

All visualization and postprocessing of atomic information require computation tools to visualize and analyze dislocation scale processes during deformation. In this study, they were performed using the Open Visualization Tool (OVITO). Various approaches were used to analyze the data, but the most important ones are the common neighbor analysis (CNA) and Dislocation Extraction Algorithm (DXA).

The common neighbor analysis (CNA) algorithm determines the geometry of bonds between an atom and its neighbor intending to determine the local lattice crystal structure of the atoms in a simulation cell. It filters the atoms and classifies them into crystalline systems to determine which atoms belong to phases or defects [156], [157]. The CNA modifier allows using subsequent modifiers such as the "select type" and "delete selected" e.g., selecting and removing atoms with FCC crystal structure which allows obtaining atoms associated with defects in this study.

A dislocation Extraction Algorithm (DXA) identifies dislocation line defects in the atomistic data [158]. It estimates Burgers circuits to extract the dislocations and stores them as vectors using the simulation cell recognition algorithm CNA. DXA determines the burgers vectors, dislocation line, and dislocation type.

3. Origin and effect of pre-existing configurations of dislocations on incipient plasticity in a single crystalline CrCoNi medium entropy alloy

Abstract

The content of this chapter was taken from the upcoming article entitled ***"Influence of dislocation configurations on the pop-in load during nanoindentation in a CrCoNi medium entropy alloy****." Frederic Habiyaremye, Antoine Guitton, Xiaolei Chen, Thiebaud Richeton, Stéphane Berbenni, Guillaume Laplanche, Nabila Maloufi***.***

The incipient of plasticity in metallic materials is linked to nucleation of dislocations. Such an event is indicated as an initial pop-in on a load-displacement curve during a nanoindentation test. The maximum shear stress at this pop-in was found to be in the range of theoretical shear stress. However, the nanoindent performed on the same sample surface exhibited a wide scattering of the maximum shear stress data. Such scattering implies that additional microstructural features control the pop-in rather than the global dislocation density. Thus, this chapter explores local dislocation configurations such as distance from the nanoindentation axis to the nearest dislocation, presence of dislocation pair, or dipole as means to explain the origin of the wide scattering of the data.

Résumé

*Le contenu de ce chapitre a été repris dans l'article à paraître intitulé « **Influence of dislocation configurations on the pop-in load during nanoindentation in a CrCoNi medium entropy alloy** ». Frederic Habiyaremye, Antoine Guitton, Xiaolei Chen, Thiebaud Richeton, Stéphane Berbenni, Guillaume Laplanche, Nabila Maloufi.*

Le début de la plasticité dans les matériaux métalliques est lié à la nucléation des dislocations. Un tel événement est indiqué par un pop-in initial sur une courbe charge-déplacement pendant un test de nanoindentation. La contrainte de cisaillement maximale à ce pop-in s'est avérée être dans la gamme de la contrainte de cisaillement théorique. Cependant, les nanoindentations réalisées sur la même surface d'échantillon ont présenté une large dispersion des données de contrainte de cisaillement maximale. Une telle dispersion implique que des caractéristiques supplémentaires de la microstructure contrôlent le pop-in plutôt que la densité globale de dislocations. Ainsi, ce chapitre explore les configurations locales de dislocations telles que la distance entre l'axe d'nanoindentation et la dislocation la plus proche, la présence d'une paire de dislocation ou d'un dipôle comme moyen d'expliquer l'origine de la grande dispersion des données.

3.1. Introduction

Metallic materials' incipient plasticity, also known as pop-in, has been extensively investigated using instrumented nanoindentation because the latter can probe localized mechanical responses at a submicron length scale [159]–[161]. Since the nanoindented volume is small, probably devoid of defects and pop-in stress (τ_{max}) is in the range of theoretical shear stress (τ_{th}) (G/25 and G/5 where G is the shear modulus), the pop-in was associated with homogeneous nucleation of dislocations (HomND) [140], [162], [163]. However, the values of τ_{max} (see Eq. 2.8) significantly varied for nanoindentation tests performed in materials with different processing methods [133] and deformation histories [136], [163]. Moreover, they varied for tests carried out the different nanoindenter tips' types [132] and varying nanoindenter tip radii [133]. There were no observations of pop-in in some cases. These observations revealed that the pop-in might also be due to heterogeneous nucleation of dislocations (HetND).

Such significant variation of τ_{max} was linked to dislocation content quantified by global dislocation density (ρ). The values of τ_{max} for undeformed samples were higher than the deformed samples [132], [163]. The undeformed sample has low ρ, and incipient plasticity is more likely to occur by homogeneous dislocation nucleation (HomND). In contrast, a deformed sample has higher ρ, and plasticity is more likely to occur by heterogeneous nucleation of dislocations. However, such reasoning failed to explain the scattering of τ_{max} data when the tests are carried out in the same material [132], [139]. Barnoush *et al.* [132] results revealed that 42% of 230 nanoindent showed pop-ins in cyclically deformed aluminum with a global value of $\rho = 2\times10^{14}$ m^{-2}. Thus, a new parameter beyond global ρ is needed to explain the mechanisms of incipient plasticity. Barnoush *et al.* [137] suggested that the scattering may be related to the probability of finding pre-existing dislocations (PED) below the nanoindenter during the nanoindentation test. They quantified this probability using the mean free path ($\bar{L}$) that is determined using the relation, $\bar{L} = \sqrt{\rho^{-1}}$. For larger $\bar{L}$, there is a small probability of finding pre-existing dislocation (PEDs) in the nanoindented regions, *i.e.*, the initial pop-in is more likely to occur by HomND and vice versa. Additionally, large nanoindenter tips are more likely to encounter PEDs in the nanoindentation volume than small nanoindenter tips. The limit of ρ and $\bar{L}$ on the explanation of pop-in lies in the fact that they are based on theoretical/numerical predictions rather than real experimental observations. While the predictions can be relevant for simple configurations such as a random distribution of defects,

it fails to explain the pop-in in the complex structures of defects such as an array, a wall, a pair of dislocations, the dipole of dislocations, and so forth.

The significant scattering of τ_{max} have also been linked to the concentration of vacancies in FeCoCrMnNi HEA [164], [165]. Zhu *et al.* [165] evaluated activation energy and volume for the onset of plasticity and concluded that the pop-in occurs by vacancy or vacancy mediated heterogeneous dislocation nucleation in FeCoCrMnNi HEA. In this mechanism, vacancy clusters collapse to form dislocation loops. Using the same concept similar to the one used for pre-existing dislocation, Wang *et al.* [164] found that increasing the tip radius increases the activation volume and thus lowers the τ_{max} because the nanoindenter tip is more likely to encounter a vacancy.

This study combines experiment-based A-ECCI and nanoindentation and elastic calculations based theory to investigate:

- origin and mechanisms of incipient plasticity in CrCoNi MEA
- effect of various localized configurations of dislocations on the values of τ_{max} in CrCoNi MEA.

3.2. Microstructure

A BSE micrograph of a single crystal of CrCoNi MEA displays randomly oriented regions with distinct shapes, sizes, and small disorientations (Fig. 3.1). These regions are called dendrites. The orientation randomness of these dendrites is due to crystal mosaicity and such microstructural growth was observed in single crystals grown with the same method [166]. Crystal mosaicity is due to crystal lattice rotations caused by mechanical forces resulting from thermal, shrinkage, and convective stresses and the chemistry of the liquid phase alloy, which locally affects undercooling [110].

An EBSD map acquired with a step size of 5 µm in Fig. 3. 2 reveals that θ between neighboring dendrites are below 7°. LAGBs separate these dendrites which are also referred to as subgrains. Fig. 3. 3 is a frequency histogram that shows that ~92% of the LAGB in the single crystalline CrCoNi alloy have $\theta < 2.5°$. The average size of the dendrite was around 100 µm calculated using the linear intercept method.

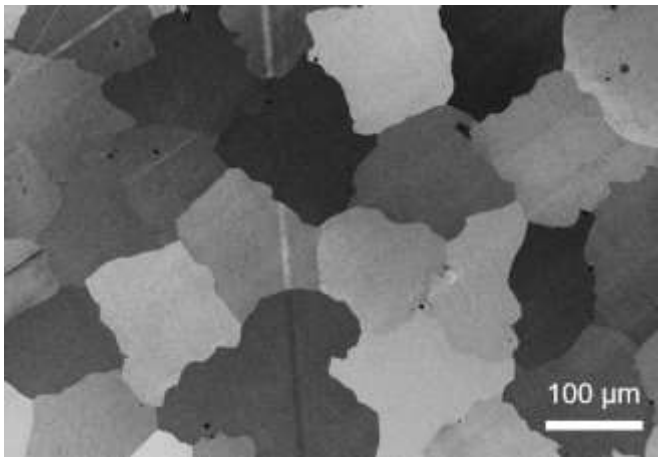

Fig. 3.1. BSE micrograph of a single crystalline CrCoNi MEA

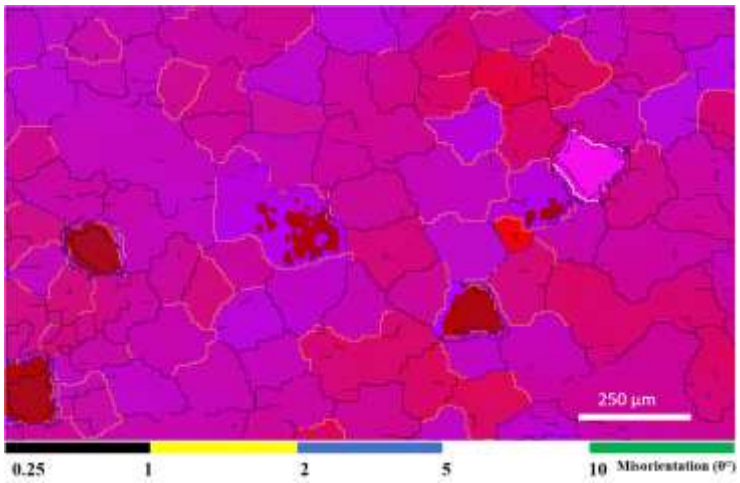

Fig. 3.2. All Eulers and misorientation maps of a single crystalline CrCoNi MEA.

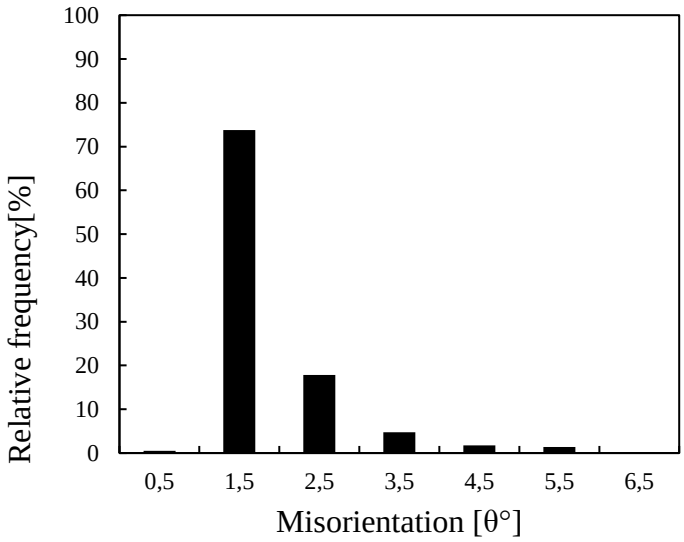

Fig. 3.3. The misorientation distribution in a single crystal of CrCoNi MEA.

EDS maps (see Figs. 3. 4b-d) showcase the distribution of chemical elements within the BSE micrograph in Fig. 3.4a. Numbers (1-4) and numbers (5-8) in Figs. 3. 4b-c are EDS point analyses of interdendritic and dendritic regions, respectively. The results of EDX point analyses are summarized in Table 3.1. They revealed that interdendritic regions are ~25 µm wide with an average composition of $Cr_{35}Co_{32}Ni_{33}$ whereas dendrites are enriched in Co and depleted in Cr with an average composition of $Cr_{30}Co_{36}Ni_{34}$. Since all of our nanoindent were performed at distances of at most 12 µm away from the LAGB (see Fig. 3a), the mechanical responses are therefore representative of the composition present in the interdendritic regions ($Cr_{35}Co_{32}Ni_{33}$) [167].

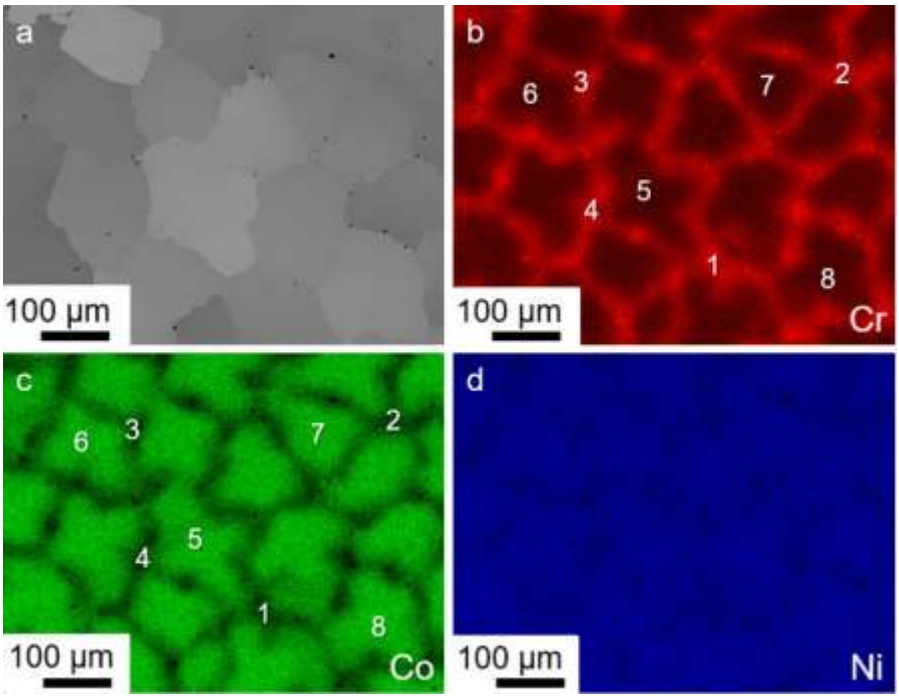

Fig. 3.4. (a) BSE micrograph of an [001]-oriented single crystal of the CrCoNi MEA. EDS maps of (b) Cr, (c) Co, and (d) Ni (Maps were provided by Guillaume Laplanche and coworkers) [167].

Table 3. 1. Chemical composition in dendritic and interdendritic regions (in at.%) for positions in Figs. 3.4c-d [167]

Interdendritic regions				Dendritic regions			
N°	Cr	Co	Ni	N°	Cr	Co	Ni
1	35.0	31.5	33.5	5	30.0	36.0	34.0
2	35.0	32.0	33.0	6	30.5	35.5	34.0
3	35.0	31.5	33.5	7	30.0	36.0	34.0
4	35.0	31.5	33.5	8	30.0	35.5	34.0

3.3. Defects

The imaging and characterization of crystal defects using the A-ECCI have been done for various materials using invisibility criteria [23], [27], [56]. The ECC micrographs acquired at four different diffractions vectors (**g**) in the same region are displayed in Fig. 34. Most dislocations appear as asymmetrical wing-shaped spots with a black and white (B-W) contrast. The spots are traces on the surface of a threading dislocation (TD), *i.e.*, a dislocation nearly perpendicular to the surface. Due to the surface relaxation effect, the Burgers vectors of the TDs cannot be determined using the invisibility criteria [23], [27] because these dislocations exhibit a residual contrast even if the invisibility criteria are fulfilled. Therefore, it is very convenient to determine the density of dislocations. However, it is not straightforward to determine whether a particular dislocation has an edge, mixed, or screw character. The direction of the B-W contrast of TDs is the same for the dislocation with the same **b** (see a white rectangle in Fig. 3.5**). S**ince the CrCoNi MEA crystallizes into a single FCC phase from the melt, these dislocations are most likely to have $\mathbf{b} = \frac{1}{2}\langle 110\rangle$. The stacking fault (see ellipses in Figs. 3.5a, b, d) has a contrast that starts with a bright line at the intersection with the surface and fades as it inclines deep into the crystal because the diffracted intensity oscillates with depth in the crystal. Such contrast has been modeled in ref. [168]. The stacking fault (see ellipses in Fig. 3.5) was in contrast under $\mathbf{g} = (2\text{-}40)$, $\mathbf{g} = (240)$, $\mathbf{g} = (220)$. It is out of contrast under $\mathbf{g} = (2\text{-}20)$ (see Table 3.2).

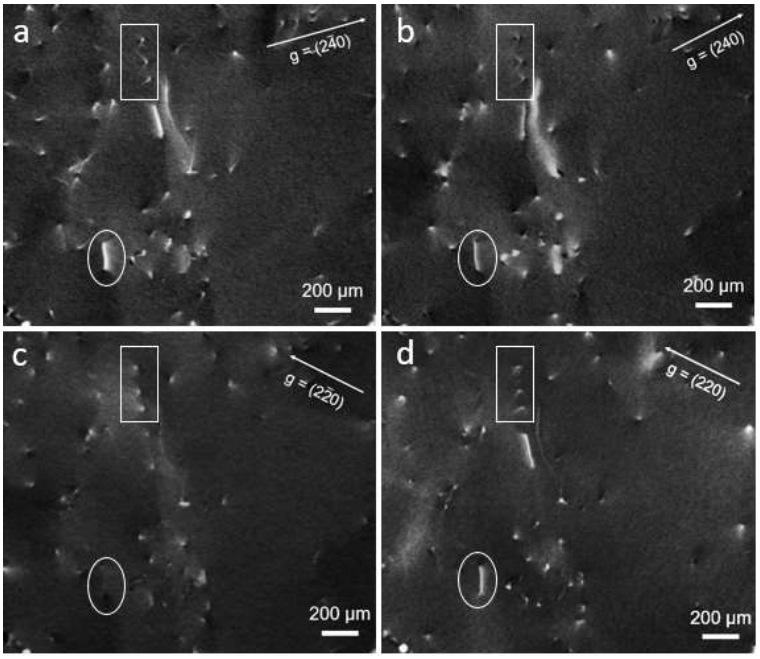

Fig. 3.5. ECC micrographs under four different diffraction vectors (**g**)

Table 3.2. **g.R** criterion for stacking fault

R/g	(2-40)	(240)	(2-20)	(220)
[111]	≠ 0	≠ 0	= 0	# 0
[112]	≠ 0	# 0	= 0	≠ 0
[-1-12]	# 0	# 0	= 0	# 0

Since this FCC monocrystalline sample is non-deformed, *i.e.* grown from the melt, it is more likely that partial dislocations are formed by the collapse of the lattice surrounding a cavity that has been produced by the aggregation of vacancies on (111) planes, i.e., they are Frank partial dislocations with **R** belongs to a/3<111>[29]. Thus, the most likely **R** is a/3[111].

The dislocation density of dislocation in a single crystal was determined using ECC micrographs. Generally, $\rho = L/V$, where L is the length of dislocation and V is the volume containing L. Alternatively, $\rho = n/A$, where n is the number of dislocations intersecting the unit area [29]. Using the second method, since the dislocation are TDs, and they cannot be out of contrast, the average global ρ is 3.62×10^{12} m^{-2}.

3.4. Incipient of plasticity

Arrays of nanoindents were placed on the sample employing a maximum load of 0.5 mN and 1mN using a spacing of 3 µm and 5 µm, respectively. Such spacing is enough to avoid the mutual interaction between neighboring nanoindents. Figure 3.6a displays an array of 36 nanoindents made at a maximum force of 1 mN. Nanoindents for this study were inside subgrains far away from the LAGBs to ensure that they do not influence the nanoindentation test results [27]. Figure 3.6b showcases a representative load-displacement (P-h) curve for a nanoindent performed inside a subgrain (at ~10 µm from the nearest LAGB, see the white ellipsis) up to a maximum load of 0.5 mN. It shows that the first part follows Hertz's law; therefore, it is elastic (see the red dashed line in Fig. 3b and Eq. 2.7). The average value of R obtained by Hertz fit using Eq. 2.7) is ~220 nm. Assuming isotropic elasticity, E_r is estimated to be ~212 GPa using Eq. 2.8. On the P-h curve in Fig. 3.6b, the end of the elastic portion is characterized by an initial pop-in that occurs at a pop-in load (P_p) of 203.4 µN and a pop-in depth (h_p) of 13.45 nm.

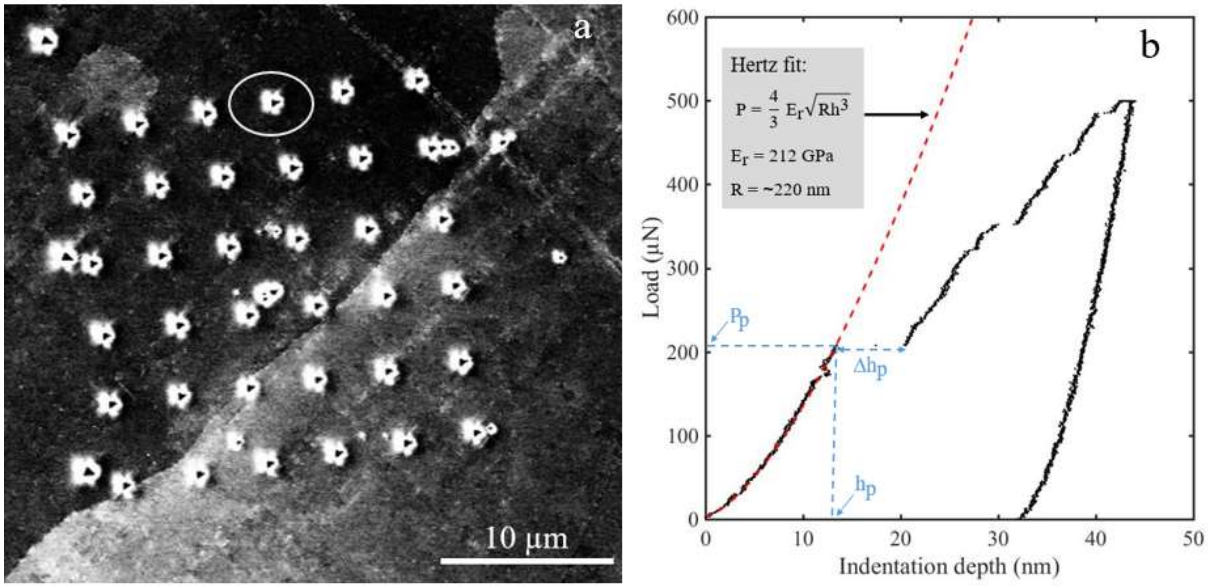

Fig. 3.6. (a) An array of 36 nanoindents with a maximum load of 1 mN. (b) A typical load-displacement curve of the nanoindent inside the subgrain for a maximum load of 0.5 mN The red dashed line represents the fit to the theoretical Hertz elastic contact solution.

Both h_p and Δh_p increase with the pop-in load as shown by Fig. 3.7. This plot is consistent with the ones reported by Schuh and Lund [40] in 4H SiC, Pöhl [20] in pure polycrystalline iron, and Sekido *et al.*[41] in steels. The values of h_p are linked to the mechanisms responsible for the initial pop-ins, while the values of Δh_p are related to the number N_{hkl} of induced dislocations emitted below the nanoindenter linked in grain with hkl orientation [[169]]:

$$N_{hkl} = \frac{\Delta h_{hkl}}{|b|} \tag{3.1}$$

where Δh_{hkl} is the projection of Δh_p along with the slip system.

The local dislocation density (ρ_{loc}) can be estimated with the aid of figure 3.8. It is achieved by overlaying the ECC micrographs before and after nanoindentation. A circle is drawn around the plastically deformed zone (the bright region on the ECC micrograph Fig. 3.8b). Dislocations inside this zone are assumed to be the ones interacting with the incoming nanoindenter. The same circle is drawn on the ECC micrograph before nanoindentation. Values of ρ_{loc} are calculated as the number of dislocations in the circle over the area of the circle. P_p is plotted against ρ_{loc} (Fig. 3.9). The results show that the relationship is consistent with a power-law of the form, $P_p \sim 3.1 \times 10^5 \times \rho^{-0.27}$.

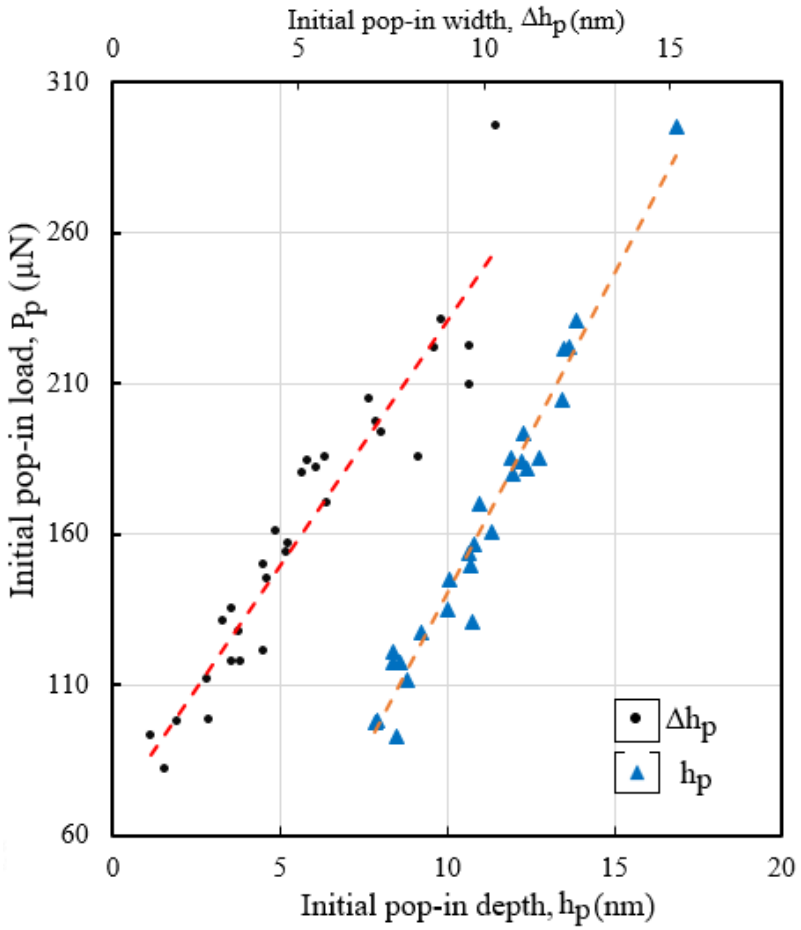

Fig. 3.7. The initial pop-in load (P_p) against the pop-in depth (h_p) and pop-in width (Δh_p).

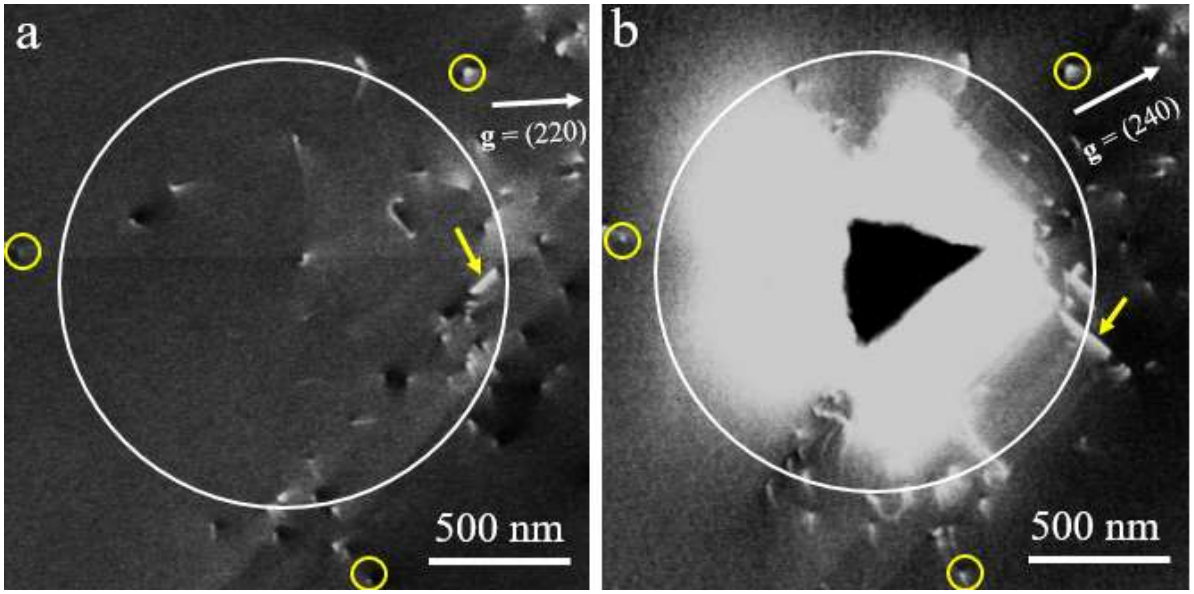

Fig. 3.8. ECC micrographs of localized microstructure (a) before and (b) after nanoindentation. Yellow circles in figures 1a-b enclose reference dislocations used to show that the two images are taken in the same region. Yellow arrows indicate stacking faults. White circles show the areas from which ρ is determined.

Slightly different power-law relationships of the form, $P_p = \rho^{-0.5}$ (ρ being determined as the density of etch pits) and $P_p = s \times \rho^{-0.5} + t$ (where *s* and *t* are constants, ρ being the density of Frank-Read sources that are randomly dispersed throughout the simulation box) have previously been obtained in refs [9] and [43], respectively. The dislocation activation model used in [163] was limited by two fitted experimental data points and a ρ range from 1×10^{12} m^{-2} to 2×10^{12} m^{-2}. Employing a three-dimensional dislocation dynamics and finite element method simulator, Crone *et al*. [170] improved the number of data points to four and the ρ range from 1.25×10^{12} m^{-2} to 8×10^{13} m^{-2}. However, the number of data points was still too low to define a reliable power law for the relationship between ρ and P_p. Although one can argue that ρ and P_p are linked by a power-law based on experimental and numerical results in the literature, these results are limited in terms of ρ range to produce an acceptable and reliable fitting model. Therefore, further experiments with access to a wide range of ρ_{loc}, for example 10^7- 10^{14} m^{-2}, are needed to capture the experimental scatter in the measured P_p values and its relationship with ρ.

From P_p values and analyzed nanoindentation data, Eq. 2.8 is used to calculate the τ_{max}. Fig. 3.10 shows τ_{max} against ρ_{loc}. τ_{max} were found to be in the range of 6-11 GPa. These values are also within the range τ_{th}, *i.e*, between G/25 = 3.6 GPa and G/5 = 18 GPa (G = 90 GPa for CrCoNi [83]). Such values imply that the initial pop-in may be related to nucleation of dislocations. The model for homogeneous nucleation of a dislocation loop has been developed by Hirth and Lothe [28]. It was expanded by Michalske and Houston [171] and then by Chiu and Ngan [172]. In this model, an increase in the total energy due to the creation of an edge dislocation loop of radius, r, and **b** perpendicular to the loop plane is given by:

$$E = \frac{Gb^2 r}{2(1-\nu)} \ln\left(\frac{2r}{r_o}\right) - \pi r^2 \tau b \qquad (3.2)$$

Where ν is the Poisson's ratio, r_o is the dislocation core radius and τ is the applied stress. The first term on the right-hand side is the elastic energy of the loop and the second term is the work done by the τ.

Solving the Eq. 3.2 for $\frac{dE}{dr} = 0$ give the critical radius, r_c:

$$r_c = \frac{Gb}{4\pi\tau(1-\nu)} \left[\ln\left(\frac{2r_c}{r_0}\right) + 1\right] \qquad (3.3)$$

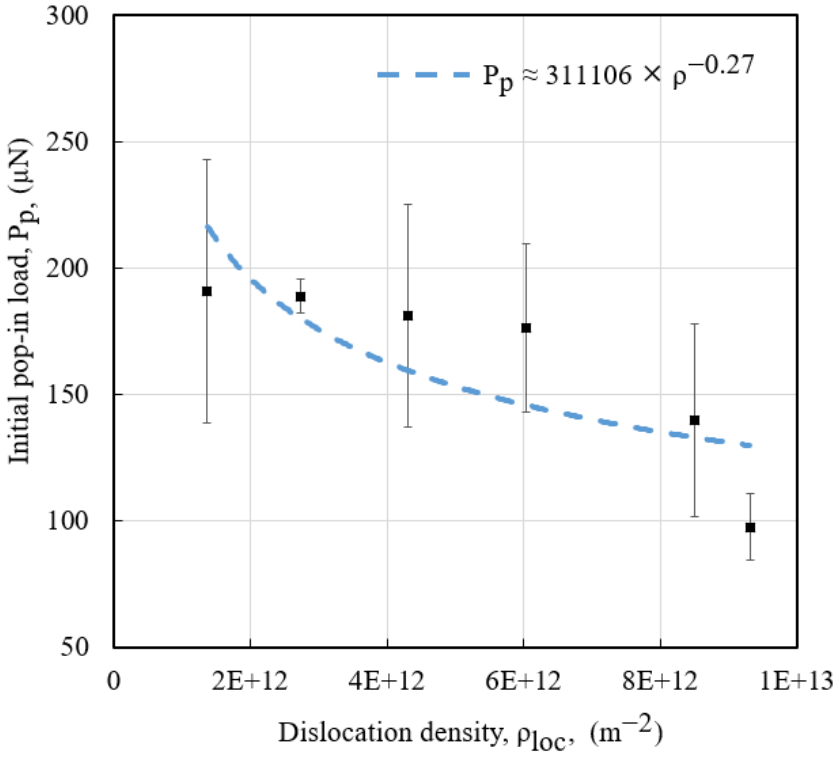

Fig. 3. 9. A plot of the initial pop-in load (P_p) against the localized density of dislocations (ρ_{loc}). The curve is built by determining the ranges of P_p and ρ_{loc}. The average and standard deviation for P_p and τ_{max} were determined on each range. The middle point is the average and the maximum and minimum are ± standard deviation.

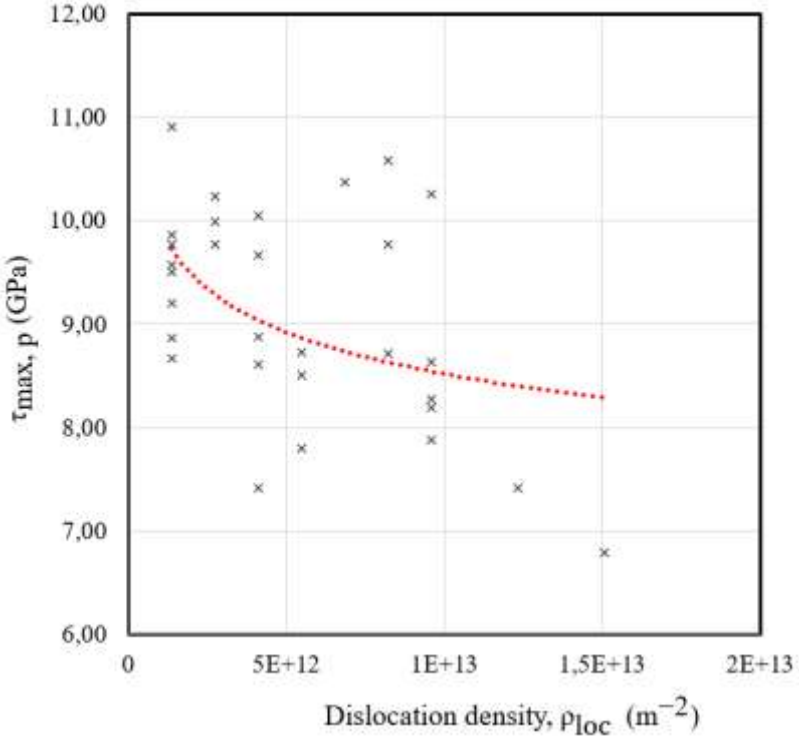

Fig. 3. 10. A plot of ρ_{loc} against τ_{max}

Moreover, replacing r_c in Eq. 3.2 gives, the activation energy (E_a) to create a stable dislocation loop in the interior of a crystal as follows:

$$E_a = \frac{Gb^2 r_c}{4(1-\nu)} \left[\ln\left(\frac{2r_c}{r_o}\right) - 1\right] \tag{3.4}$$

Solving $E_a = 0$ (at 0K) (the absence of thermal fluctuation energy) gives $r_c = 1.36\, r_0$ or $r_c = er_0/2$ (e is the Euler angle). Again, replacing r_c value in Eq. 3.2 and solving for τ_c gives the relation,

$$\tau_c = \frac{Gb}{\pi\,(1-\nu)\,e\,r_0} \tag{3.5}$$

τ_c is resolved shear stress of τ_{max} on active slip system required for spontaneous nucleation of an edge dislocation loop. For $r_0 = 3b$, $\nu = 0.31$, $b = 0.252$ nm , $G = 90$ GPa, $\tau_c \approx 5.1$ GPa at 0 K. Since $\tau_c \sim \tau_{max,\,t}/2$ where $\tau_{max,\,t}$ is the theoretical τ_{max} [165], [172], $\tau_{max,\,t} = \sim 10.2$ GPa. At room temperature, the thermal contribution will lower τ_c and thus $\tau_{max,\,t}$. Using finite element analysis and MD simulations, Wagner *et al.* [173] found that increasing temperature from 0 to 300 K results in a decrease of τ_{max} from 5.8 to 4.9 GPa in a single crystal of aluminium. Based on that study, it is reasonable to assume that $\tau_{max,t}$ will decrease from 10.2 GPa at absolute temperature to 9.5 GPa at 293 K. Therefore, the initial pop-in is more likely to occur by HomND when the values of τ_{max} is greater than 9.5 GPa. When the values of τ_{max} are less than 9.5 GPa, the initial pop-in is more likely to occur by HetND.

Figure 3.10. also shows that τ_{max} can take significantly different values for the same ρ_{loc}. For example, τ_{max} takes the value of 7 GPa or 10 GPa for $\rho_{loc} = 1.37 \times 10^{12}$ m^{-2}. Similar results were reported in ref. [163]. In the latter, a large scattering of the values of τ_{max} for the same local etch pit dislocation density was reported in tungsten. Therefore, a new parameter is required to explain the scattering of τ_{max}.

Since the distribution of dislocations lying in the zone of ECC visibility is known before nanoindentation, the distance from the nanoindentation axis (center of residual nanoindent) to the nearest dislocation (D_{nd}) is introduced as a new spatial parameter beyond the average ρ_{loc}. This parameter is obtained by superimposing the micrographs acquired from the same location before and after nanoindentation (Fig. 3.11a-b and c-d). Then, D_{nd} is measured as shown in figure 3.11a. Given that h_p is less than 20 nm in our experiments, whereas defect observation depth of A-ECCI is ~150 nm (depending on both **g** and material) [26], it is reasonable to assume

that dislocations observable at the surface from ECC micrographs are truly the ones that may affect the nanoindentation test. Figure 3.12 displays a plot of τ_{max} against D_{nd}. The latter shows that τ_{max} increases with D_{nd} following a power law of the form: $\tau_{max} \approx 4.8 \times D_{nd}^{0.12}$. The area beneath the nanoindenter tip with τ_{max} is calculated from the contact radius obtained from Hertz's theory:

$$a_c = \left(\frac{3P_pR}{4E_r}\right)^{\frac{1}{3}} \tag{3.6}$$

inserting appropriate values in eq. 3.6 gives an average a_c of 50±5 nm. For nanoindentation test at $D_{nd} > 600$ nm, *i.e.*, far away nanoindentation axis, HomND seems to be responsible for the initial pop-in. In this case, HomND is governed by lattice friction (the pop-in occurs when τ_{max} is greater than the Peierls-Nebarro stress) and tip radius (*i.e.*, a small radius has a small sampling volume which is more likely to be a defect-free volume) [141].

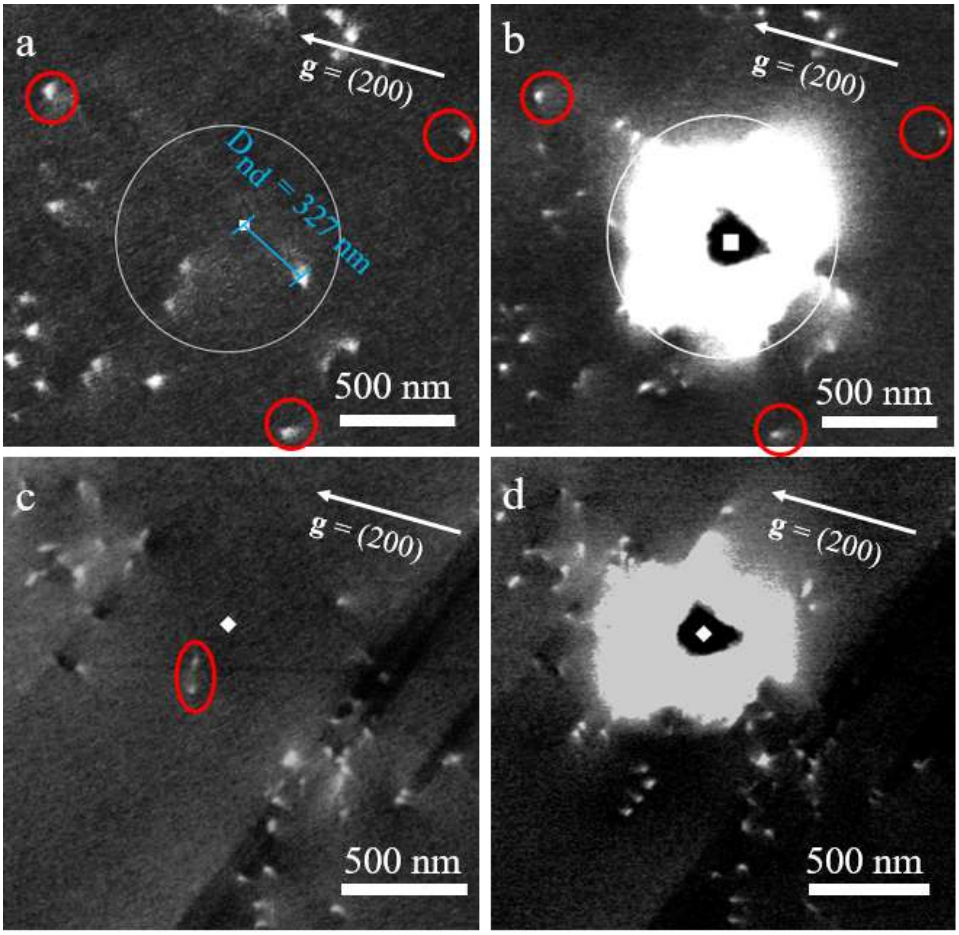

Fig. 3. 11. ECC micrographs (a) before and (b) after nanoindent in the subgrain at a maximum load of 0.5 mN. The blue lines represent the distance D_{nd} from the nanoindentation axis to the nearest visible dislocation. Red circles are reference dislocations. ECC micrographs (c) before and (d) after nanoindentation for dislocation pair/dipole.

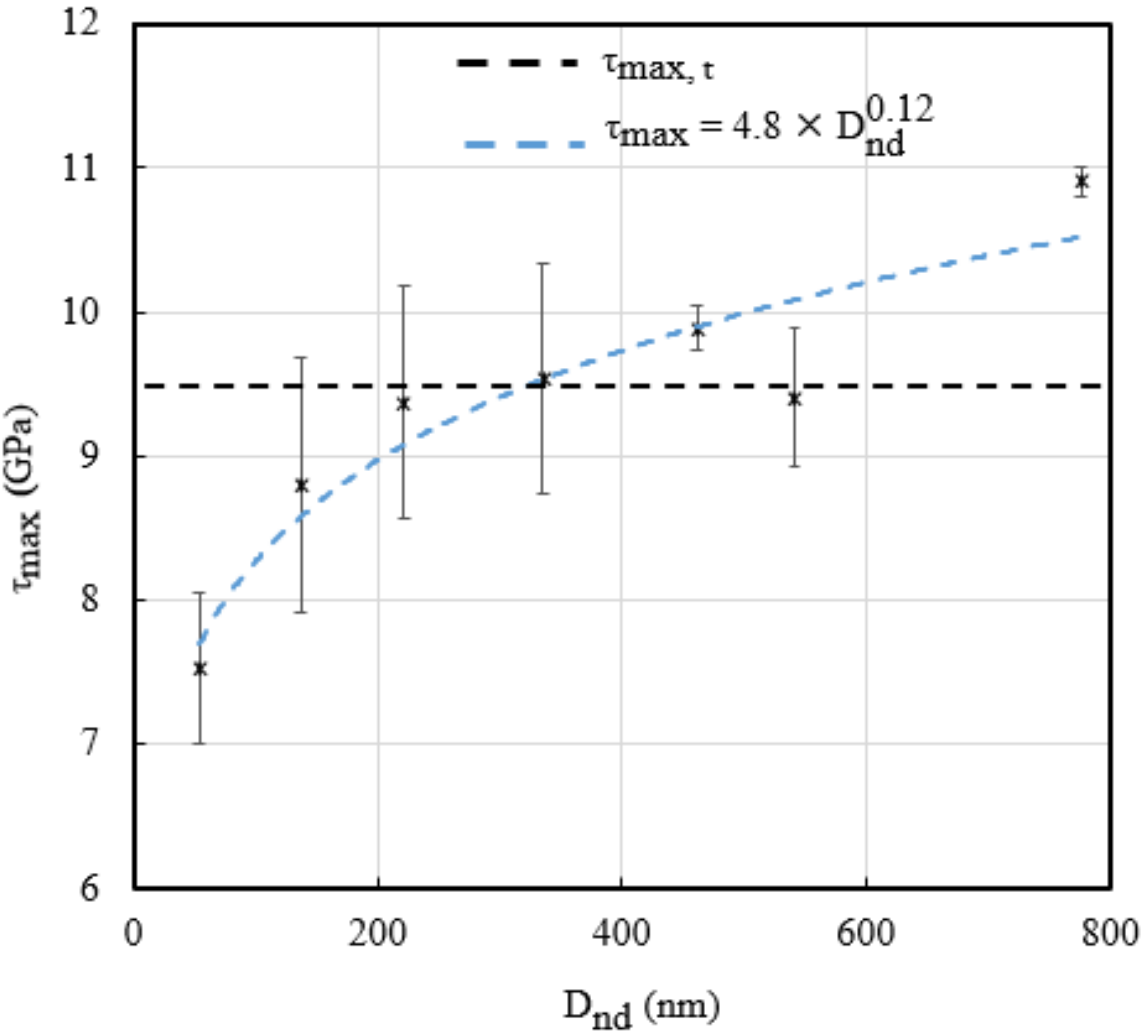

Fig. 3.12. A plot τ_{max} against D_{nd}. Initially, the ranges of ρ and D_{nd} were chosen. Then, the average and standard deviation for P_p and τ_{max} were determined. The minimum and maximum are ± standard deviation, while the middle point is the mean value for each range.

The decrease of τ_{max} when D_{nd} becomes smaller has been linked to HetND due to pre-existing defects such as dislocations, stacking faults, and vacancies [163], [164], [174]. The first mechanism states that incipient plasticity occurs by activating PEDs when they are mobile [29]. The second mechanism occurs by HomND, but the pre-existing stress field reduces both τ_{max} and h_p. Even if only one nearest dislocation was considered for the plot in Figs. 3.12, ECC micrographs in Fig. 3.11a shows that there are other dislocations at a distance close to D_{nd} which may additionally enhance the pre-existing stress field beneath the nanoindenter.

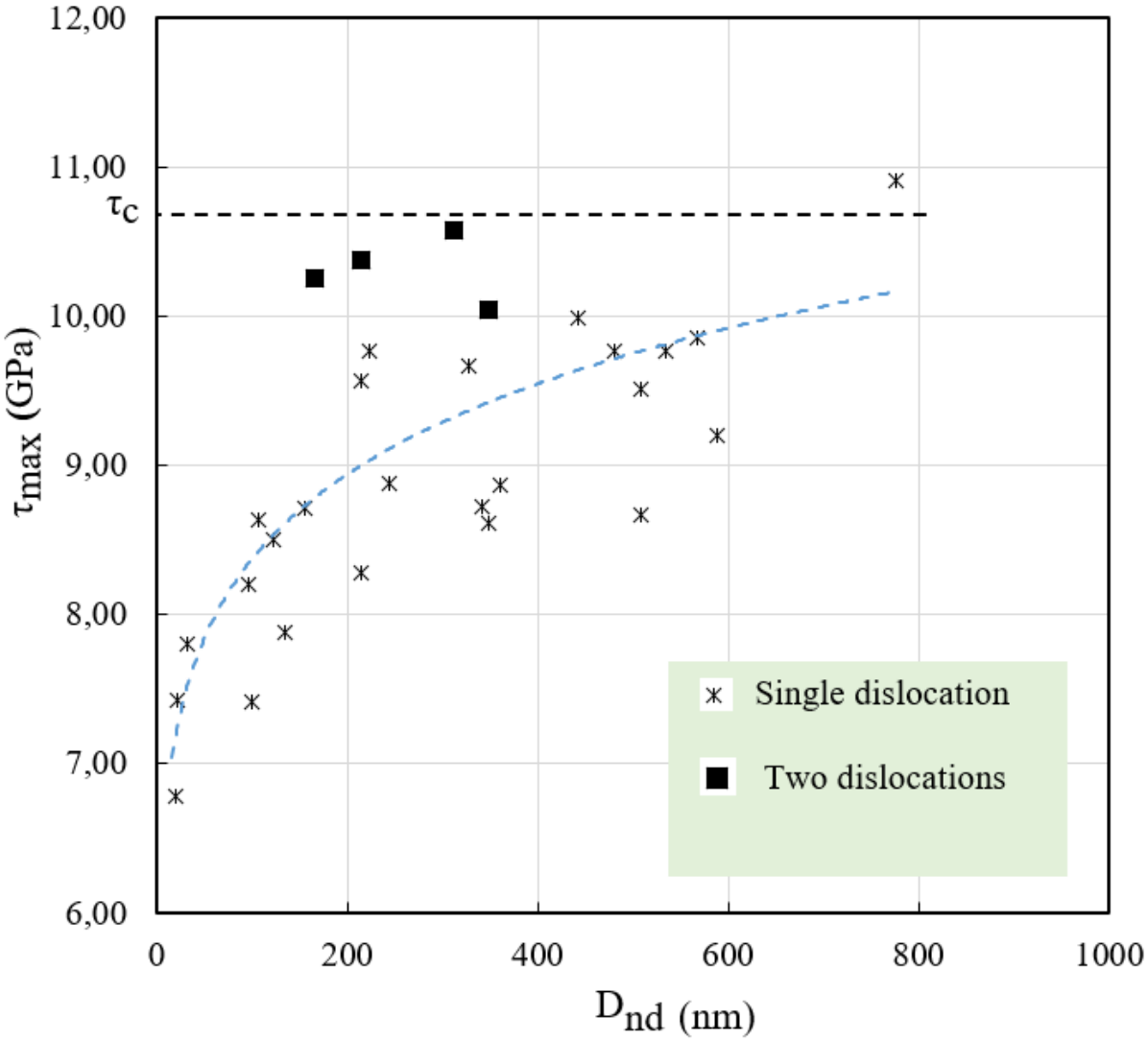

Fig. 3.13. A plot of maximum shear stress at the pop-in (τ_{max}) against distance (D_{nd}) from the nanoindentation axis to the nearest dislocation (D_{nd}), showing the difference between single dislocations and the configuration of two dislocations.

Fig. 3.13 shows a detailed plot of Fig. 3.12. The four square-shaped points show nanoindents that were placed where the nearest dislocation configuration is either a dislocation pair (two parallel dislocations with the same **b** (Fig. 3.14a)**)** or a dislocation dipole (two parallel dislocations with opposite **b** (Fig. 3.14b)) as shown by a representative micrograph (Figs. 3.11d). These nanoindents exhibited higher τ_{max} than their counterparts at the same D_{nd}.

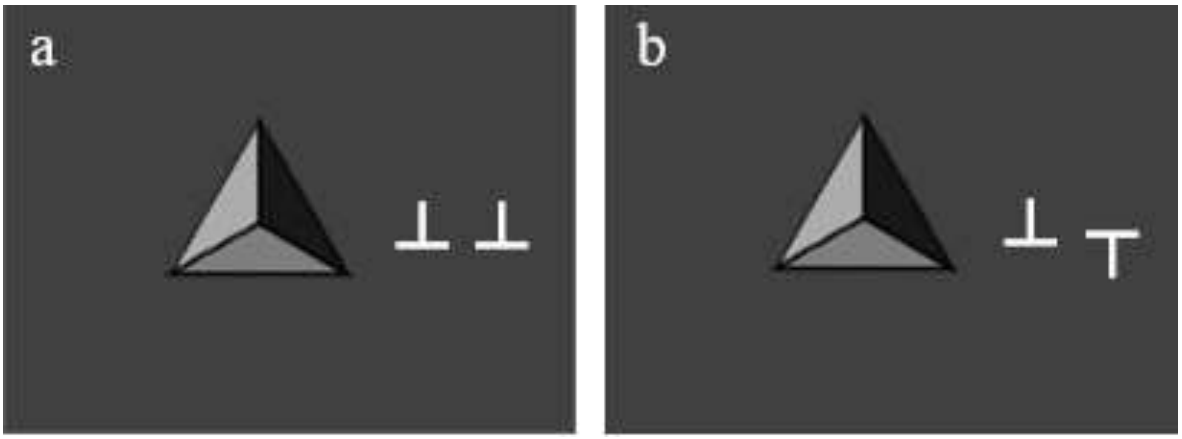

Fig. 3.14. (a) Schematic representation of a dislocation pair and a dislocation dipole. The symbols ⊥ are used to mark the positions of dislocations and do not refer to their type.

3.5. Numerical calculations based on elasticity theory

3.5.1. Procedure

This three-dimensional numerical calculation uses the superposition principle in linear elasticity to compute the stress field at an arbitrary point (X_1, X_2, X_3). The latter is obtained as the sum of the stress field from the nanoindenter and the stress field due to the dislocation (s). The stress field produced by the axisymmetric nanoindenter is calculated from the equations derived from the contact mechanics by Johnson (see Eqs. 2.9, Johnson's equations describe a point load applied to elastic half-space under the assumption of linear isotropic elasticity) [106] and then integrated on the contact surface between a nanoindenter and the sample surface as follows [146]:

$$\frac{\sigma_{ij}\left(\frac{x}{a},\frac{y}{a},\frac{z}{a}\right)}{p_o}=\int_0^a\int_0^{2\pi}\check{p}(x',y')\sigma_{ij}\left(\frac{x}{a}-x',\frac{y}{a}-y',\frac{z}{a}\right)rd\theta dr \tag{3.7}$$

where x'= rcosθ, y'= rsinθ, p_o is the mean contact pressure, $p_o=\left(\frac{6\times(E_r)^2}{\pi^3 R^2}\right)^{\frac{1}{3}}$ describe the elastic regime until the incipient plasticity occurs during loading, $\check{p}(x',y')$ is the surface pressure distribution for a circular contact, $\check{p}(x',y')=\sqrt{1-\frac{x'^2+y'^2}{a^2}}$. The nanoindentation axis is parallel to x_3. The stress field generated by a dislocation is determined from the superposition of the well-known solutions of edge and screw straight dislocations in a homogeneous infinite medium under linear elasticity [29]. The dislocation self-stress field is considered to be zero at the dislocation position. The dislocation core radius is assumed |3***b***|. In this calculation, only a dislocation with an edge character is used. Two arbitrary edge dislocations with **b** = ½ [10$\bar{1}$] on (111) plane and **b** = ½ [110] on (1-11) were chosen. They are regarded as infinite straight

lines parallel to x_3, where x_1 and x_2 are the contact surface. The crystal directions of their **b** are either parallel to X_1 or at an arbitrary angle in the x_1-x_2 plane.

The simulation box has dimensions of 200 × 100 × 100 nm^3. Single dislocation, dislocation pair, and dislocation dipole are placed at varying distances from the nanoindentation axis at a fixed x_3. The maximum shear stress's depth is calculated using the relation $Z_p = 0.48a_c$ (a_c = 50±5 nm). Thus, Z_p is in the range of 21-26 nm. The maximum shear stress (MSS) is calculated using the Tresca Criterion (half the difference between the maximal and minimal principal stresses). The properties of CrCoNi MEA and diamond nanoindenter used for the elastic calculations are displayed in Table 3.1 and Table 3.2, respectively.

Figure 3.15 shows the stress field solely due to nanoindentation. The stress field around the nanoindentation axis (0, 0) is axisymmetric and the MSS is 3.21 GPa (Fig. 3.15a) at (0, 0, -25). The depth of MSS of 25 nm is within the range of the theoretically calculated Z_p (Fig. 3.15b).

Table 3.1. Properties of CrCoNi MEA

Property	Values
Materials	CrCoNi MEA
Orientation	[001]//x3
Crystal structure	FCC
Young's modulus (E, GPa)	235 [83]
Shear modulus (G, GPa)	90 [83]
Poisson's ratio (ν)	0.31 [83]
Bulk modulus (B, GPa)	208 [83]
Yield strength at RT (σ_{YS}, GPa)	360 [19]
Lattice parameter (a, nm)	0.357 [85]
Burgers vector magnitude (|**b**|, nm)	0.2524

Table 3.2. Parameters and values used in the calculations for the nanoindenter [163].

Parameters	Values
Nanoindenter	Diamond
Young's modulus (E, GPa)	1141
Tip radius (R, nm)	220
Poisson's ratio (ν)	0.07

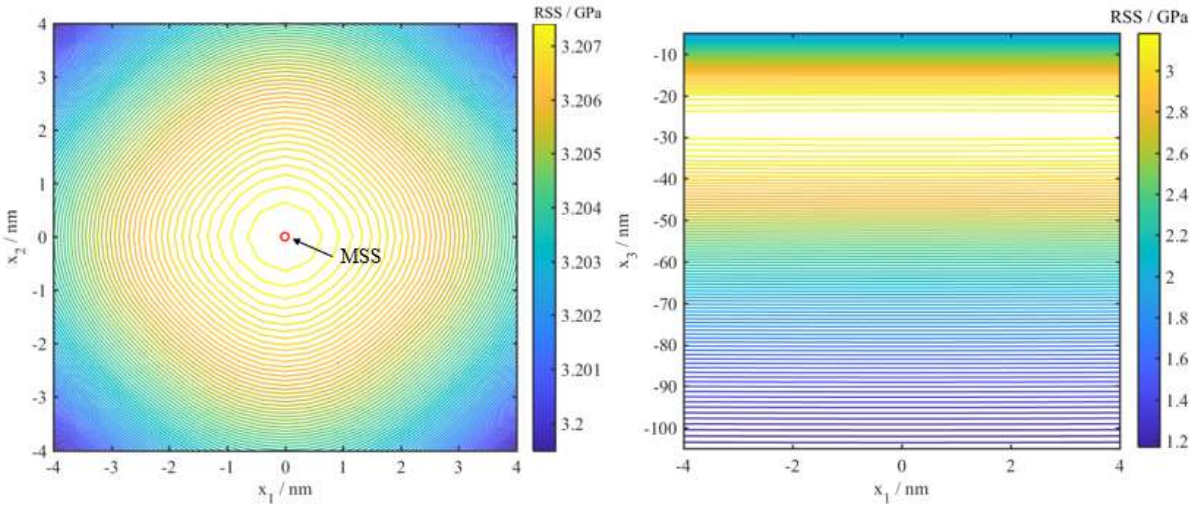

Fig. 3.15. The stress distribution solely due to nanoindentation (a) x_1-x_2 plane (b) x_1-x_3 plane. The maximum shear stress (MSS) shown by the red circle is the point with the highest stress.

When an infinitely long edge dislocation with **b** = ½ [10-1] was placed at (0,0) (Fig. 3.16a) with the dislocation line parallel to x_2 axis and **b** parallel to x_1, the MSS increased almost 4-fold from 3.21 GPa to 11.70 GPa. The distribution of the stress changed dramatically. Unlike the stress field due to nanoindent, the stress field due to dislocation is not axisymmetric

Therefore, the high-stress field is mainly in quadrants II and I while there are only stress field lines due to nanoindent in quadrants III and IV (Fig. 3.16b). The x_2-x_3 plane stress distribution showed that the MSS is at (-0.4, 0, -25) nm (see fig. 3.16c). Moreover, it shows high stress along the line of dislocations as expected (Fig.3.16c). At around Zp, the stress field distribution varied compared to other positions along with x_3 (see red ellipsis in Fig. 3.16c). Fig. 1.16d displays the stress distribution of dislocation with opposite **b** = ½ [-101]. Like Fig. 3.16b, the stress field lines are mainly distributed in quadrants II and I.

A dipole and a pair of two edge dislocations with **b** = ± ½ [-101] were placed at (0, 0) nm and (0, 2) nm Figures 3.17a-c. The dislocation spacing was chosen through a successive calculation stating from the 3b. For the spacing less than 2 nm, the least MSS is higher than 15 GPa which is unrealistic. The MSS for a dipole (14.39 GPa) was higher than a pair of dislocations (13.49 GPa) for spacing between two dislocations of 2 nm. The stress field lines are mainly between the dislocations of the dipole while it is more or less evenly distributed with respect to the position of the two dislocations for the pair of dislocations. Moreover, the position of the MSS is (0.4, 0, -25) nm for a dipole of dislocations while it is (-0.4, 0, -25) nm for a pair of dislocations. The position of MSS is between the two dislocations because they attract each other. Therefore, there will be larger stress between them, and the maximum position is

reasonably located between the two toward the dislocation adjacent to the nanoindentation. At such a position, the contribution of the nanoindenter stress field is high. If the lowest to highest order is used, it would be: dipole of dislocation > pair of dislocation > single dislocation > nanoindentation.

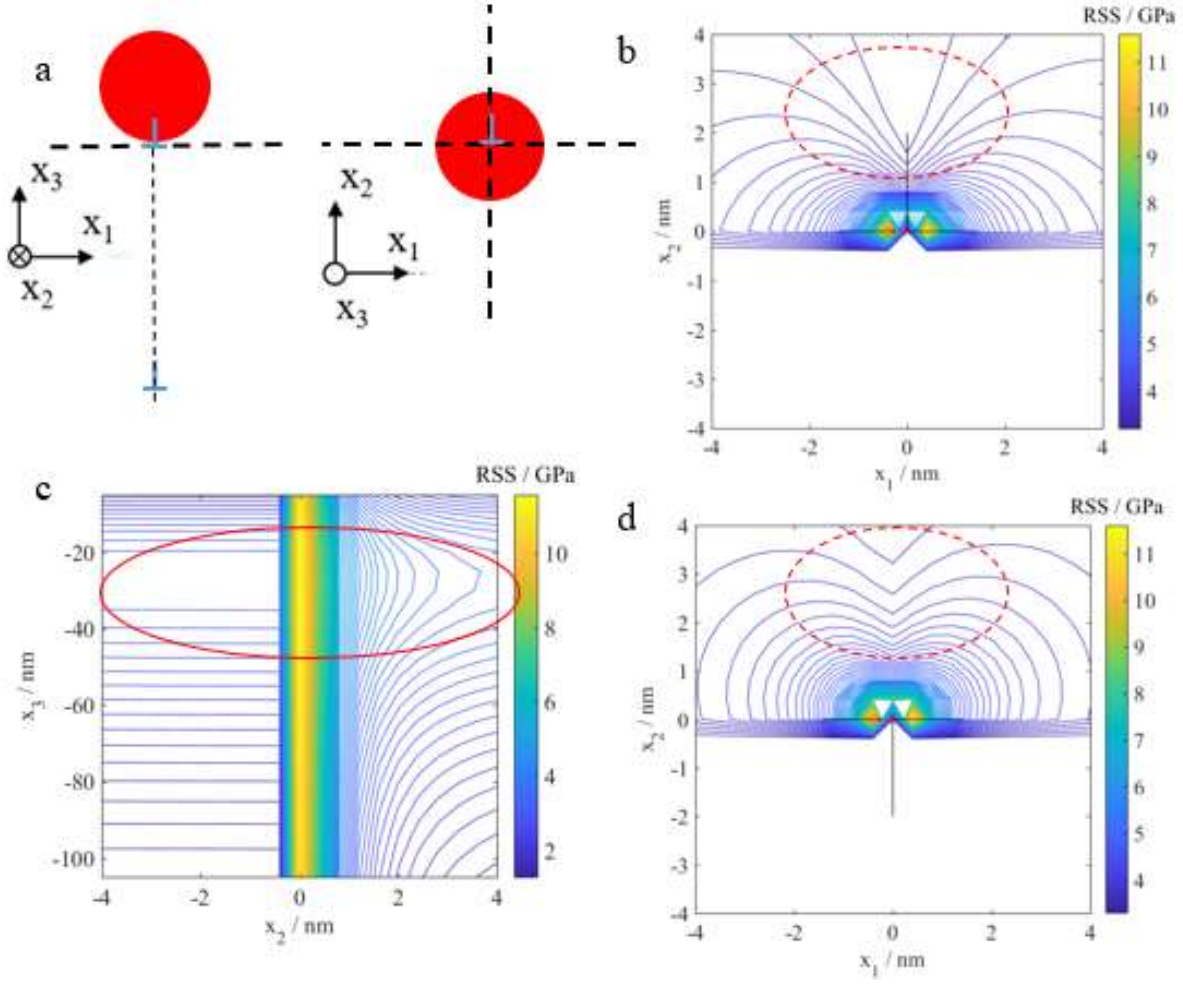

Fig. 3.16. (a) Schematic showing the position of an infinitesimal long edge dislocation at (0, 0) nm with **b** parallel with X_2 and **u** parallel with X_3 (X_1-X_3 and (X_1-X_2) planes are shown). The stress distribution is due to nanoindenter and dislocation for the (b) X_1-X_2 (c) X_2-X_3 planes for dislocation with **b** = ½ [10-1] and (d) X_1-X_2 plane for dislocation with opposite **b** = ½ [-101].

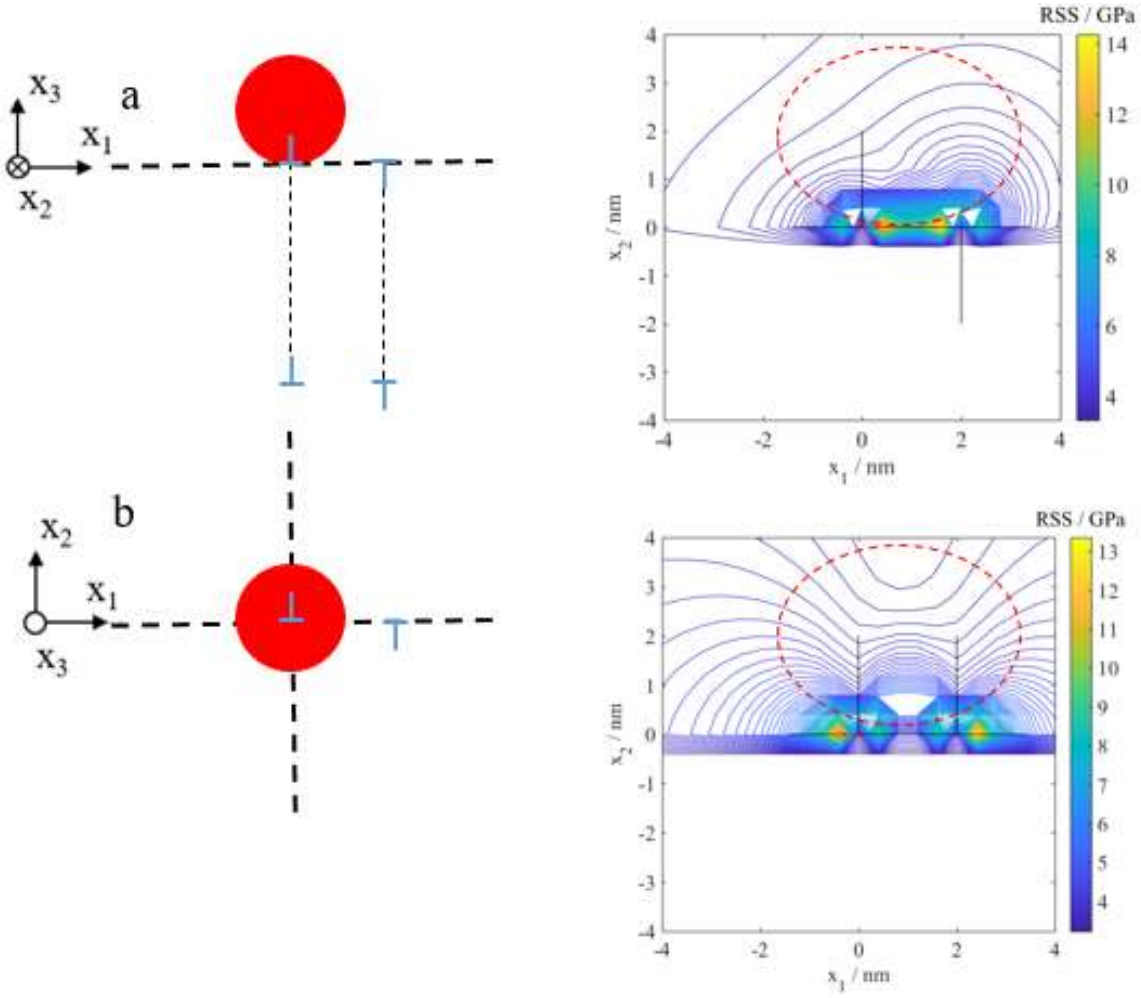

3.17. Schematic representation of the position of a pair of dislocations in-plane (a) X_1-X_3 and (c) X_1-X_2 planes. Stress distribution for (c) a dipole, (d) a pair of dislocations.

A dislocation with **b** = ½ [-10-1] was placed at different distances from the nanoindentation axis (D_{nd}). The values of MSS against D_{nd} (Fig. 3.18). For this curve, the mesh size was reduced to optimize calculation time. However, the trends would be the same irrespective of the mesh size. The figure shows that MSS decreases with increasing $D_{nd.}$ Such a trend implies that the contribution of the stress field of the dislocation to the total stress field decreases as the dislocation is far away from the nanoindentation axis. It becomes stable at 50 nm and exhibits a slight small decrease. The reason for the minimum at 50 nm is not clear. However, it may have been caused by the location of mesh points during calculations rather than an actual physical mechanism.

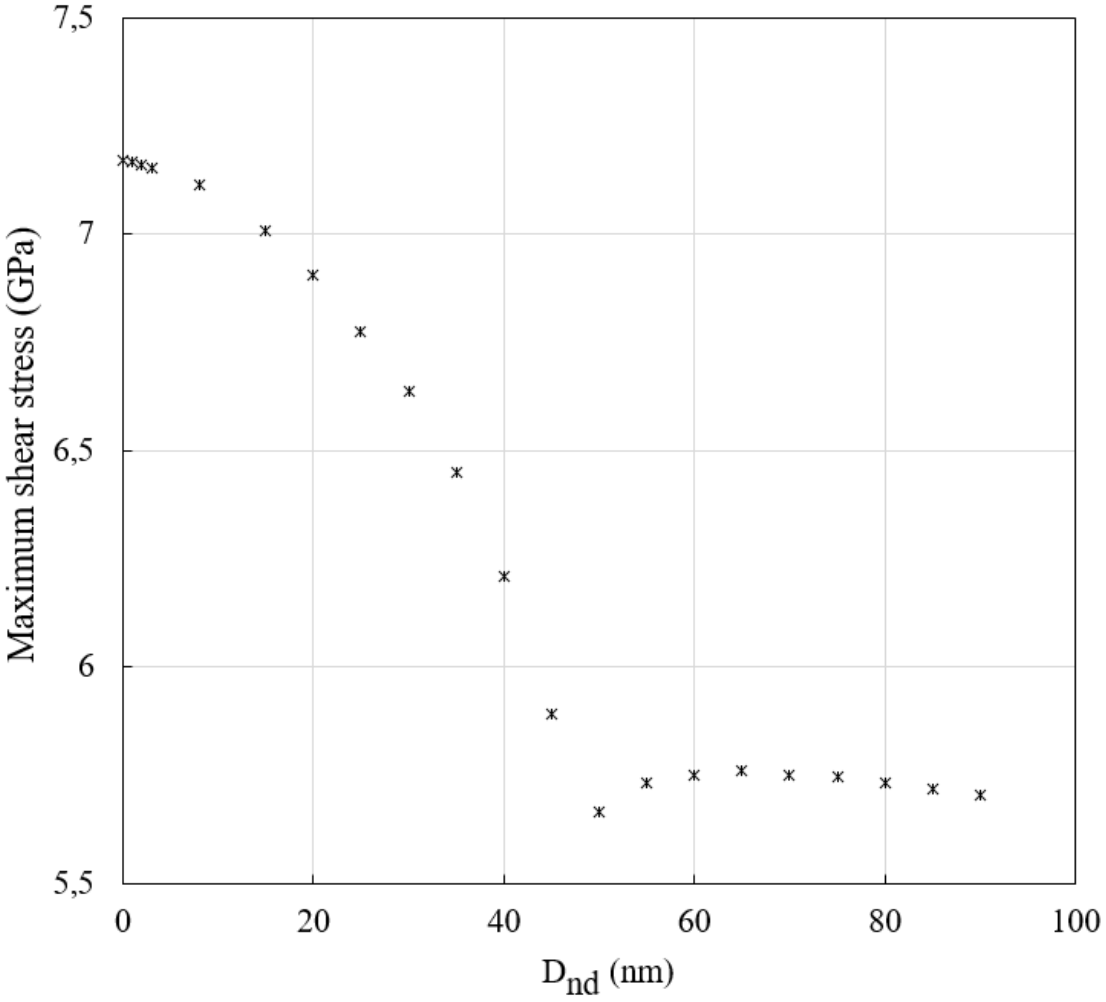

Fig. 3.18. D_{nd} against the MSS for **b** = ½ [10-1].

3.6. Discussion

ECC micrographs from our experimental study provide the localized configurations of dislocation, which allow us to investigate, beyond ρ, other essential parameters such as D_{nd}. Besides, elasticity calculations are used to further our analysis by providing unreachable configurations by the experiment, such as the influence of a single dislocation, dislocation dipole, and a pair of dislocations. The theoretical τ_{max} increases proportionally to $P^{1/3}$ and $h^{1/2}$ and it becomes maximum at a depth of $0.48a_c$ which represents the shear stress required for the onset of plasticity.

In the absence of PEDs, τ_{max} approaches τ_{th} and it represents a nanoindent placed in a defect-free zone. The occurrence of the initial pop-in at τ_{max} approaches τ_{th} in the defect-free zone has been reported in refs. [141], [175]–[177]. In the presence of PEDs, τ_{max} is the sum of τ_i and τ_d

where τ_i and τ_d are the shear stresses due to nanoindentation and PEDs, respectively. The value τ_d can be obtained by:

$$\tau_d = \tau_{max} - \tau_i \quad (3.8)$$

The influence of PEDs on incipient plasticity has been studied in refs. [136], [138], [178]. In these references, they obtained higher τ_{max} in low global ρ materials than in high global ρ materials. They argued that there are many PEDs and dislocation sources and pop-in occurs at a low τ_{max} in high global ρ materials. However, a large scatter of nanoindentation data within the same sample raises many questions about whether other factors are implicated in incipient plasticity [135], [139].

In dislocation free zone $\tau_d = 0$ (Eq. 3.8) and $\tau_{max} \approx \tau_i$. In presence of PEDs, τ_d is non-zero and depends on D_{nd}. From the experiment, τ_d values vary from 0 at $D_{nd} > 600$ nm to ≈ 4 GPa at a dislocation below the nanoindenter ($D_{nd} \approx 0$). Similar results were obtained from the elasticity calculations. Both the experiment and the numerical model agree that the contribution of τ_d to the maximum shear stress for the onset of plasticity decreases with D_{nd}. However, their values differ in magnitude because numerical calculation values of MSS are obtained for a single edge dislocation placed in a perfect crystal, whereas experimental values of τ_{max} may be due to dislocations with different characters at different D_{nd} and other defects such as vacancies (not observable by A-ECCI) that are concomitantly interacting with the stress field of the nanoindenter [131], [173].

In addition to the D_{nd} parameter, the contribution of τ_d depend on the dislocation configurations as expected. Using numerical calculations, it was found that the values of MSS were higher for a pair of dislocations than for a single dislocation. While experimental τ_{max} marks the elastic-to-plastic transition, it does not specify which mechanism is responsible for it. However, both numerical and experimental results show that it is due to dislocation-based mechanisms as postulated in literature. Initial ρ-based explanations for mechanisms for the pop-in that relied on the probability of finding pre-existing dislocation below the nanoindenter [163] failed to explain a wide distribution of τ_{max} in the regions with the same ρ. Indeed, the probability of finding pre-existing dislocation increases with ρ if it is assumed that PEDs are randomly distributed, which is not always the case. Thus, ρ-based explanation partially explains the pop-in because they do not take into account the case where dislocations have a particular configuration (single dislocation, a dipole, a pair of dislocation, etc.) below the nanoindenter nor the case where a dislocation or multiple dislocations are at some distance from the

nanoindenter. This study shows that the wide statistical distribution τ_{max} and mechanisms responsible for the pop-in are mainly rooted in the localized configuration of dislocations as well as their relative position to the nanoindentation axis. However, more than one dislocation along with other defects such as point defects affect the value of τ_{max} which makes it difficult to isolate individual cases. Based on both the experiment and numerical calculations, there are three cases. The first case is that PEDs act as dislocation sources and the pop-ins occurs at a low τ_{max} and h_p for dislocation below the nanoindenter (low value of D_{nd}). The second case is that PEDs amplify the shear stress below the nanoindenter, and the pop-in occurs by HetND at an intermediate τ_p and h_p when dislocations are slightly far from the nanoindenter but can interact with it. The third case is when PEDs are far from the indented region, *i.e.*, beyond critical $D_{nd,}$ and the latter behaves as PEDs-free regions with pop-in occurring by HomDN at $\tau_{max,\,t}$ approaching τ_{th}.

3.7. Conclusions of the chapter

ECCI was coupled with nanoindentation to investigate, beyond ρ, whether configurations of dislocations and D_{nd} are responsible for both the scattering of τ_{max} and mechanisms of the initial pop-in using a single crystal of CrCoNi medium entropy alloy. Using ECCI, ρ_{loc} and configurations of dislocations where the nanoindent was to be placed, were roughly known. Moreover, elasticity calculations were used to complement the experiments and introduce model configurations of dislocations that are not accessible by the experiment.

The main conclusions of this study are as follows:

- Although experimental τ_{max} values decrease with decreasing ρ_{loc}, they also exhibit a wide scattering. Moreover, a significant difference in τ_{max} value is observed for nanoindent placed in the region with the same ρ_{loc}.
- Both experimental results and elasticity calculations agree that the contribution to the maximum shear stress by dislocations decreases with increasing D_{nd}. Moreover, the elasticity calculations revealed that different configurations of dislocation such as a pair of dislocations have more contribution than a single dislocation. Consequently, the origin of the large scatter of experimental values of τ_{max} is related to the complex interactions of stress fields due to the configurations of dislocations and the incoming nanoindenter.

- Mechanisms responsible for the initial pop-in are homogeneous and heterogeneous nucleations of dislocation, which are controlled by D_{nd} and different configurations of dislocations.

This study found that an initial pop-in is a complex event that is concomitantly controlled by a wide range of local microstructural characteristics. While this study emphasizes dislocations, other defects such as vacancies, surface roughness, and crystallographic orientation may play a role in the initial pop-in load. Therefore, further experimental or numerical studies incorporating all or some of these microstructural features are needed to understand plasticity induced by nanoindentation in metallic materials.

4. Interactions of nanoindentation induced dislocations with a low angle grain boundary in a CrCoNi MEA

Abstract

Some content of this chapter has been published in the journal of material science and engineering A. “Habiyaremye F, Guitton A, Schäfer F, Scholz F, Schneider M, Frenzel J, Laplanche G, Maloufi N., Plasticity induced by nanoindentation in a CrCoNi medium-entropy alloy studied by accurate electron channeling contrast imaging revealing dislocation-low angle grain boundary interactions. Mater. Sci. Eng. A., 817 (2021) 141364. https://doi.org/10.1016/j.msea.2021.141364.”

Nanoindentation-induced dislocation-LAGB interactions were investigated in a single crystal of CrCoNi using A-ECCI and instrumented nanoindentation. Different microstructure evolution and micromechanical responses were observed when nanoindent were placed at varying distances from the LAGB. When the distance between the LAGB and the nanoindenter tip is greater than four times the nanoindentation size (corresponding ratio: $R_d > 4$), the LAGB does not influence the micromechanical response and does not interact with nanoindentation induced dislocations. On the contrary, when the nanoindenter comes into direct or indirect contact with the LAGB ($R_d < 1$), the P-h curve deviates, at a low load, from the elastic stage and pop-ins are not observed. In this instance, the motion of pre-existing LAGB glissile dislocations accommodates plasticity. For the intermediate cases with $1 < R_d < 4$, the initial pop-in loading depends on the local defect density. In the latter case, the nanoindentation-induced dislocations impinge directly on the LAGB. Microstructural analyses reveal that the LAGB adapts to the plasticity by blocking the lattice nanoindentation induced dislocations, activating a dislocation nucleation site in the adjacent subgrain/dislocation emission from the LAGB, and inducing slight movements of its dislocations.

Résumé

Une partie du contenu de ce chapitre a été publiée dans le journal of “Material science and engineering A” "Habiyaremye F, Guitton A, Schäfer F, Scholz F, Schneider M, Frenzel J, Laplanche G, Maloufi N., Plasticity induced by nanoindentation in a CrCoNi medium-entropy alloy studied by accurate electron channeling contrast imaging revealing dislocation-low angle grain boundary interactions. Mater. Sci. Eng. A., 817 (2021) 141364. https://doi.org/10.1016/j.msea.2021.141364."

Les interactions des dislocations avec le joint de grain à faible désorientation ont été étudiées dans un monocristal de l’alliage à moyenne entropie de CrCoNi en utilisant l’A-ECCI et la nanoindentation. Différentes évolutions de la microstructure et réponses micromécaniques ont été observées lorsque les nanoindentations étaient placées à des distances variables d’un sous-joint de grain. Lorsque la distance entre le joint de grain à faible désorientation et la pointe du pénétrateur est supérieure à quatre fois la taille de l'nanoindentation (rapport correspondant : $R_d > 4$), le sous-joint de grain n'influence pas la réponse micromécanique et n'interagit pas avec les dislocations induites par la nanoindentation. Au contraire, lorsque l’nanoindenteur entre en contact directement ou indirectement avec le sous-joint de grain ($Rd < 1$), la courbe P-h dévie à faible charge du stade élastique, et les « pop-ins » ne sont pas observés. Dans ce cas, le mouvement des dislocations préexistantes du sous-joint de grain contrôle la plasticité. Pour les cas intermédiaires avec $1 < R_d < 4$, la charge initiale de pop-in dépend de la densité locale de défauts. Dans ce dernier cas, les dislocations induites par la nanoindentation sont directement sur le sous-joint de grain. Les analyses microstructurales révèlent que le sousjoint s'adapte à la plasticité en bloquant les dislocations induites par la nanoindentation, en activant un site de nucléation de dislocation dans le sous-grain adjacent/émission de dislocation à partir du LAGB, et en induisant de légers mouvements de ses dislocations.

4.1. Introduction

4.1.1. Hall Petch strengthening

The CrCoNi MEA exhibits outstanding damage tolerance at cryogenic and room temperature. Shear modulus [107] and stacking fault energy [19] are responsible for excellent damage tolerance. The high shear modulus of CrCoNi alloy encourages a strong work hardening rate. On the other hand, the low stacking fault energy promotes nanotwinning, resulting in coherent interfaces which provide additional dislocation barriers [21], [75].

The Hall-Petch strengthening is particularly effective in CrCoNi MEA [21], [42], [76]. Both grain boundaries and annealing twins were found to contribute to this strengthening, resulting in the Hall-Petch slope exceeding 600 $MPa \cdot \mu m^{-1/2}$[21]. However, there is a lack of understanding regarding the relative contributions of each different type of boundary, even though promising modeling advances were recently reported in the literature [179], [180].

Moreover, a significant scattering of critical resolved shear stresses (CRSS) for different single crystals of HEA and MEA was reported in the literature [100], [101], [181], [182]. In various single crystals, the LAGB density may enormously vary from one study to another depending on the growth rate because HEA and MEA are chemically complex and exhibit crystal mosaicity [166]. LAGBs resist the motion of dislocations. Thus, different densities of LAGBs are probably responsible for the observed scatter of CRSS values [19]. Therefore, this chapter investigates the LAGB-dislocation interactions in CrCoNi MEA to understand better, how LAGBs contribute to the strength of MEA and HEA single crystals.

4.1.2. Dislocation-LAGB interactions

The investigations of dislocation-LAGB interactions have mainly been done by simulation using discrete dislocation dynamics (DDD) and molecular dynamics (MD) [183]–[187]. MD simulation by Gao and Jin [184] of lattice dislocation-symmetric tilt Lomer-type LAGB in Ni revealed that lattice dislocations are either transmitted across the boundary or absorbed in the boundary to form a stable symmetrical or asymmetrical Hirth lock depending on the exact site of the interaction. Kapoor and Verdhan [183] revealed that a tilt LAGB reacts with the incoming lattice dislocations to form dislocation junctions, which lock them and create dislocation pile-

ups. Additionally, they found that the externally applied stress necessary to free locked dislocation follows the Hall–Petch relation, *i.e.*, LAGB obstructs dislocations' motion.

Only a handful of experimental investigations are available because they are challenging to carry out. They were mainly performed by *in-situ* and *ex-situ* tests inside a TEM [188], [189] limiting experiments to small samples (TEM lamellae). Kondo [188] observed that LAGB initially blocks and traps incoming dislocations. Then, it emits dislocations when the stress at the leading dislocation reaches a critical value. Correspondingly, Ohmura *et al.*[189] observed that a low-angle lath boundary impedes the motion of dislocations followed by their emission when critical stress is reached.

4.1.3. Grain boundary and pop-in on load-displacement curve

Various attempts to link microstructures and mechanical responses near GB were performed by carrying out nanoindentation close to GBs, analyzing the micromechanical responses, and theoretically linking them with dislocation activities without any dislocation scale imaging. Soiffer *et al.* [190] compared hardness near GBs and inside the grains in pure Cu and found that hardness near GBs is 33% higher than hardness inside the grains. They associated this behavior with the anisotropy of dislocation-GB interactions. Soer *et al.* [191] linked dislocation transmission across GBs to the pop-in on the load-displacement curve for nanoindent performed between $0.2 < R_d < 0.4$ (R_d is the ratio of the distance to the GB to the residual nanoindent size) in a BCC Fe-14wt% Si alloy because they did not observe pop-ins in the matrix (far away from the GBs). Wang and Ngan [192] observed two large pop-ins when nanoindentation tests were performed close to GBs in pure niobium. They attributed the first and second pop-ins to incipient plasticity and the sudden transmission of dislocations across the GB, respectively. Since there are several possibilities to account for the occurrence of strain bursts during nanoindentation, these tests must be accompanied by dislocation-scale observations.

In this study, instrumented nanoindentation is used to induce plasticity near a LAGB. Then, A-ECCI is employed *post mortem* to monitor the resulting microstructural changes. This chapter has the following objectives:

- To study the LAGBs in a single crystal of CrCoNi and choose the LAGB of interest.
- To explore how nanoindentation-induced dislocations interact with the LAGB of interest and the resulting micromechanical response.

4.2. LAGB of interest

Fig. 4.1 is the HR-EBSD map of the region of interest acquired with a step size of 0.35 µm in refined accuracy to detect all LAGBs. The analysis of misorientation revealed that θ < 5° and the lowest detectable θ is as low as 0.15°. The area marked with a black frame in Fig. 4.1 is magnified in the crystallite orientation map shown in Fig. 4.2a, where the red color indicates that the crystallites have near {001} orientations. Figure 4.2a is centered on a LAGB of interest separating subgrains A and B. The range of θ-values along the LAGB is 0.15°-0.3°, as deduced from the misorientation map.

Assuming that this LAGB consists of an array of equally spaced dislocations, invoking the model of Read and Shockley [29], the expected spacing between dislocations (D) can be estimated using Eq. 1.3. Using **b** = ½ a <110> and θ = 0.15-0.3°, we find D values of between 100 and 50 nm.

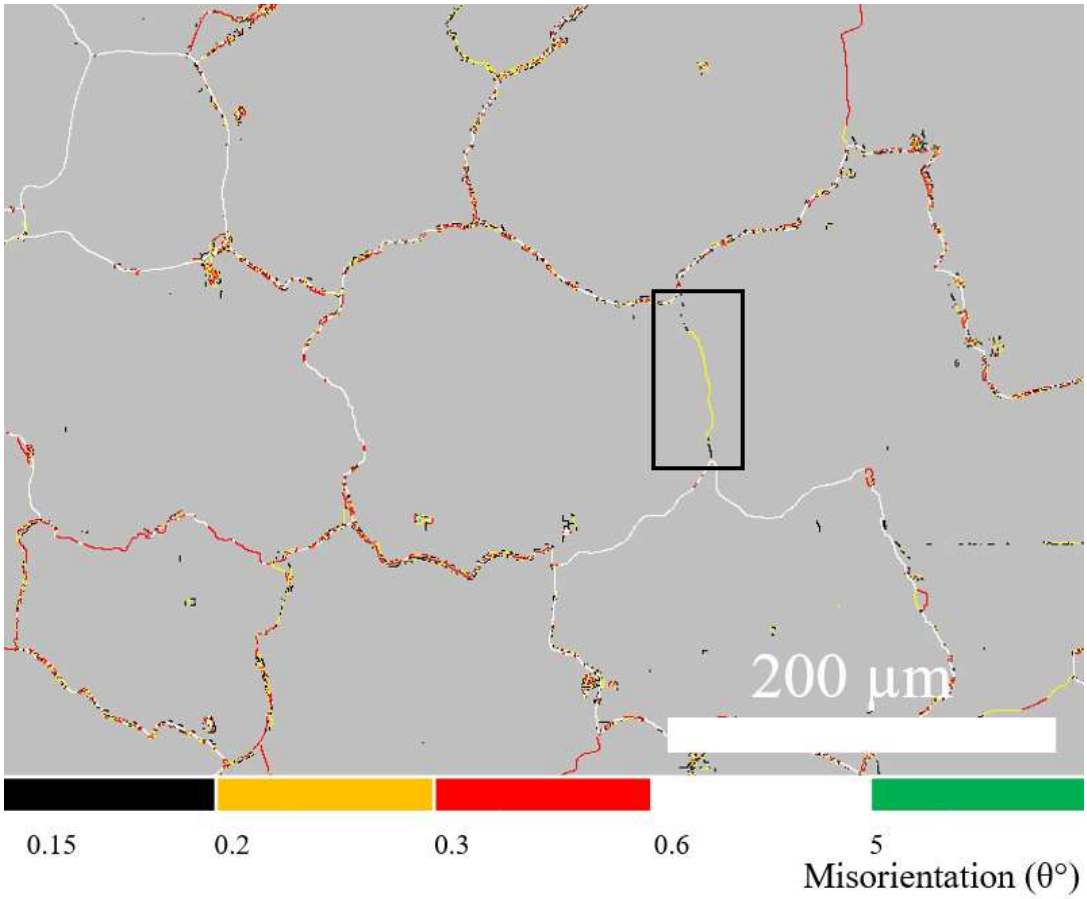

Fig. 4.1. EBSD misorientation map of the region of interest. The black rectangle shows the LAGB of interest.

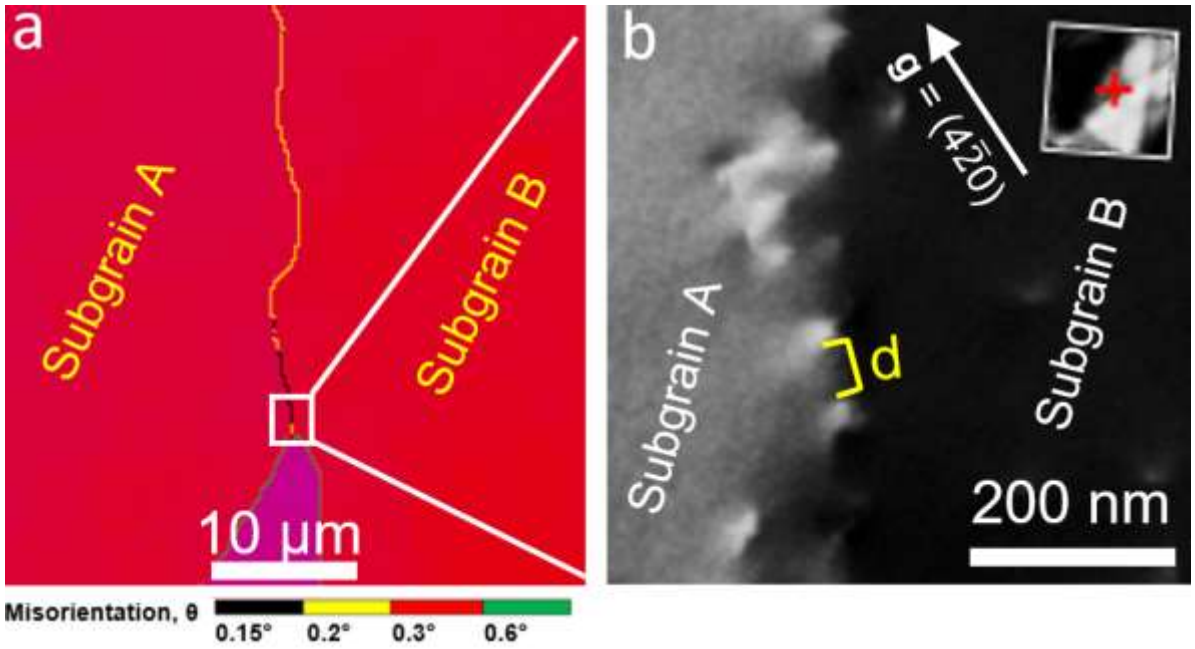

Fig. 4.2. (a) Orientation map showing the LAGB of interest. (b) ECC micrograph of a portion of the LAGB [167].

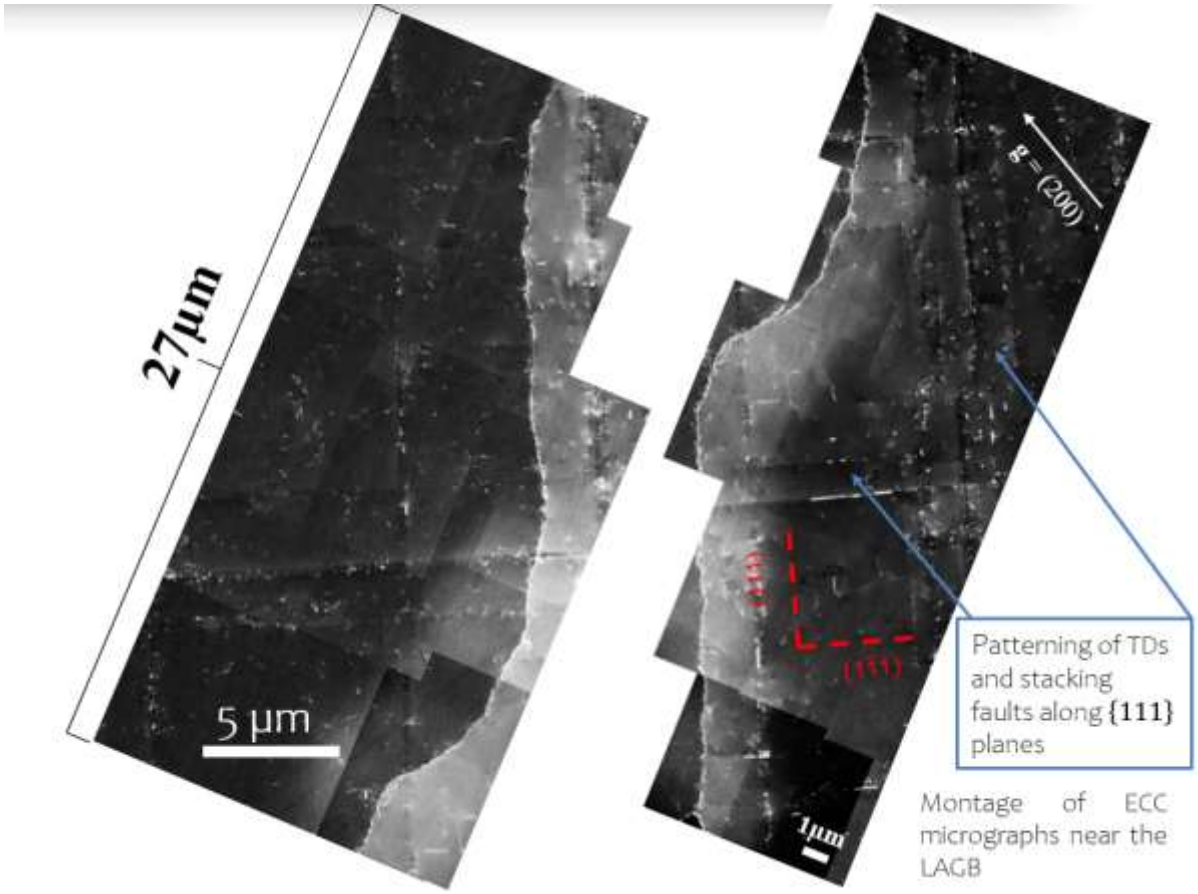

Fig. 4.3. Montage of 72 ECC micrographs acquired in the vicinity of the LAGB of interest.

The ECC micrograph (Fig. 4.2b) acquired with **g** = $(4\bar{2}0)$ in the black-framed region (Fig. 4.1) shows that the LAGB consists of an array of threading dislocations with a mean spacing D = 60 ± 5 nm (see the yellow bracket in Fig. 4.2b). From this value, an average θ = 0.24 ± 0.02° can be deduced from Eq. 1.1. This latter value is consistent with the misorientation angle determined by EBSD and validates our approach using A-ECCI.

Fig. 4.3 shows a montage of 72 micrographs in the vicinity of the LAGB of interest. It shows that the region close to the LAGB of less than ~ 5 µm has lower ρ than the region far away from the LAGB. Moreover, some dislocations and stacking faults are arranged regularly along {111} crystallographic planes.

4.3. Dislocation-LAGB interactions and their corresponding micromechanical response

An array of 56 nanoindents was placed in the vicinity of the LAGB of interest (area previously imaged by ECCI in Fig. 4.3). The maximum load was 500 µN, and the spacing between dislocations was 3 µm to avoid interactions between neighboring nanoindents. Among these nanoindents, 15 nanoindents, surrounded by a red line in Fig. 4.4a, were selected for the analysis. Their loads at the pop-in were obtained from the analysis of their corresponding load-displacement curves. Fig. 4.4b shows a plot of the initial pop-in load against the distance to the LAGB (see *x*-axis at the top) and the normalized distance R_d (ratio between the distance to the LAGB and the nanoindent size, see bottom *x*-axis on Fig. 4.4b). *R*-values are twice the distance to the LAGB since the nanoindent size is ~0.5 µm. From Fig. 4.4b, the loads at the initial pop-in are centered around a mean value of 158 µN with a standard deviation of 23 µN when $R_d > 1$ (black dashed line in Fig. 4.4b). Such pop-in loads' distribution can be associated with the density of pre-existing defects before nanoindentation [139].

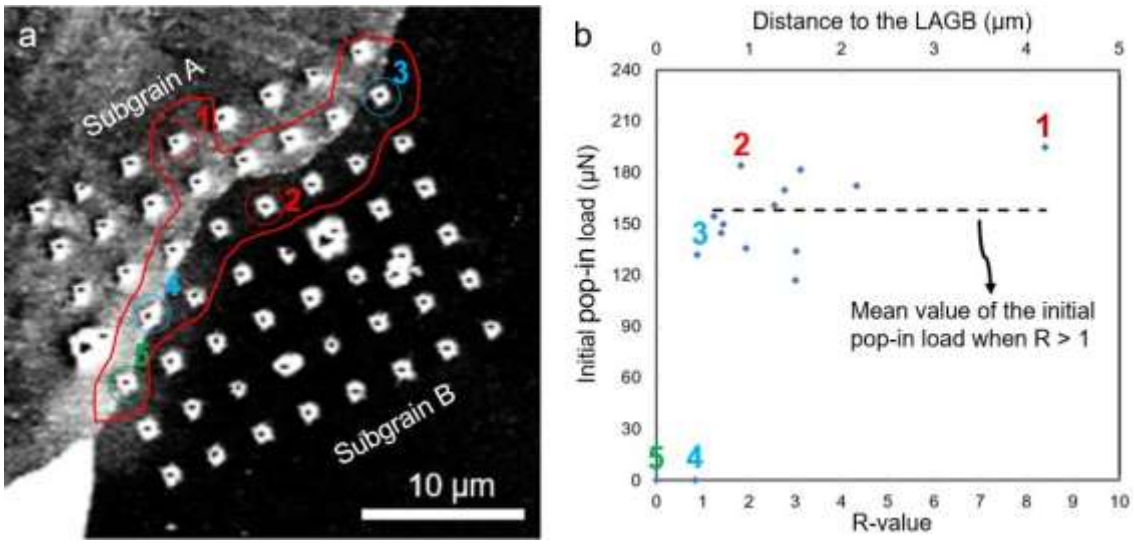

Fig. 4.4. (a) The array of 7×8 nanoindents close to the LAGB of interest. (b) Nanoindents close to the LAGB (see red curves) were used to plot R-value and distance to the LAGB against the initial pop-in load. Numbers and colored circles show nanoindents analyzed in detail in subsequent sections. The black dashed line in (b) shows the average initial pop-in load of nanoindents when $R_d > 1$.

Moreover, a significantly lower pop-in load was found for nanoindents that are closer to the boundary ($R_d < 1$, #4 and #3 in Fig. 4.4a), whereas it was absent for nanoindents on the LAGB (#5). For comparative purposes, we investigated two nanoindents (#1 and #2 in Fig. 4.4a) located inside subgrains A and B, far away from the LAGB. The following sections compare the microstructure evolution and micromechanical response of the five nanoindent mentioned above, and the results are presented in Figs. 4.5-10.

4.3.1. Micromechanical response and microstructure evolution inside the subgrains

Nanoindentation was carried out in subgrains A and B (nanoindents #1 and #2 shown in Fig. 4.5a) at locations with an average $\rho = 2.02 \times 10^{12}$ m^{-2}. Fig. 4.5b shows their load-displacement (*P*-*h*) curves (black and red curves for nanoindents in subgrains A and B, respectively). Both curves were fitted with the contact theory of Hertz described by Eq. 2.7 (see chapter 2), implying that the initial contact is purely elastic (see the dotted light blue curve in Fig. 4.5b). At the end of the elastic deformation, the initial pop-in occurs at loads of 194 μN and 185 μN in subgrains A and B, respectively (black arrow in Fig. 4.5b). The origins and mechanisms of the initial pop-in have been discussed in chapter 3.

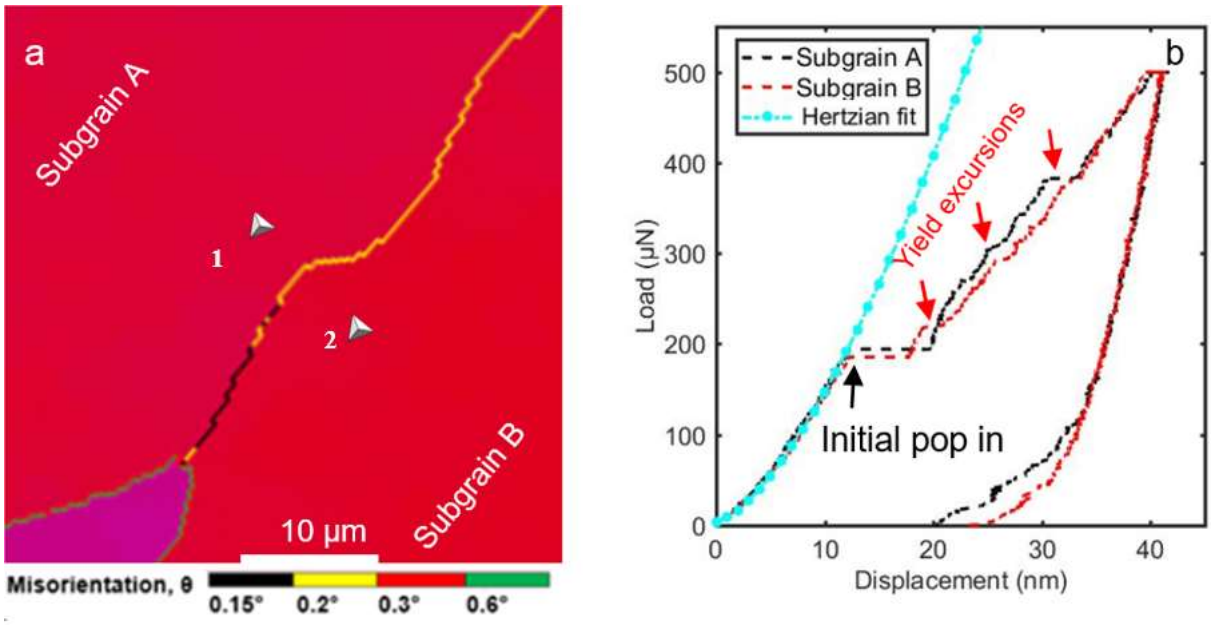

Fig. 4.5. (a) Positions of nanoindents in the subgrains A and B superimposed onto the EBSD misorientation and all Eulers maps (nanoindents #1 and #2 in Fig. 3a). (b) Their corresponding load-displacement curves in subgrains A and B [167].

Figure 4.5b shows that the initial pop-in is followed by multiple small yield excursions highlighted by red arrows. These subsequent pop-ins were attributed to the unlocking of pinned pre-existing defects [139] or motion of dislocations [193], [194]. Figs. 4.6 displays ECC micrographs acquired before and after nanoindentation and their corresponding schematic representations for the nanoindent in subgrain A. Pre-existing threading dislocations (PEDs) are shown in Fig. 4.6a. Pile-ups of nanoindentation-induced dislocations (NID) (blue arrow in Figs. 4.6c) are observed along the traces of the {111} planes. Indeed, plastic deformation of CrCoNi MEA occurs by gliding of 1/2<110> dislocations that can be dissociated into 1/6<112> Shockley partials on {111} planes in CrCoNi alloy [19]. The bright areas, enclosed by the red ellipses in Fig.4.6c correspond to stacking faults or nano-twins, which were also observed by ECCI in other metallic materials [24], [168].

A three-step procedure was followed to distinguish PEDs and NIDs. The ECC micrographs were acquired using the same diffraction conditions before and after nanoindentation. Then, the two micrographs were overlaid to follow the positions of the PEDs. Finally, new dislocations that appeared and formed pile-ups on {111} planes were identified as NIDs. A schematic drawing of the deformed microstructure in Fig. 4.6c is shown in Fig. 4.6d, where PEDs, NIDs, and SFs are marked in blue, yellow, and red, respectively.

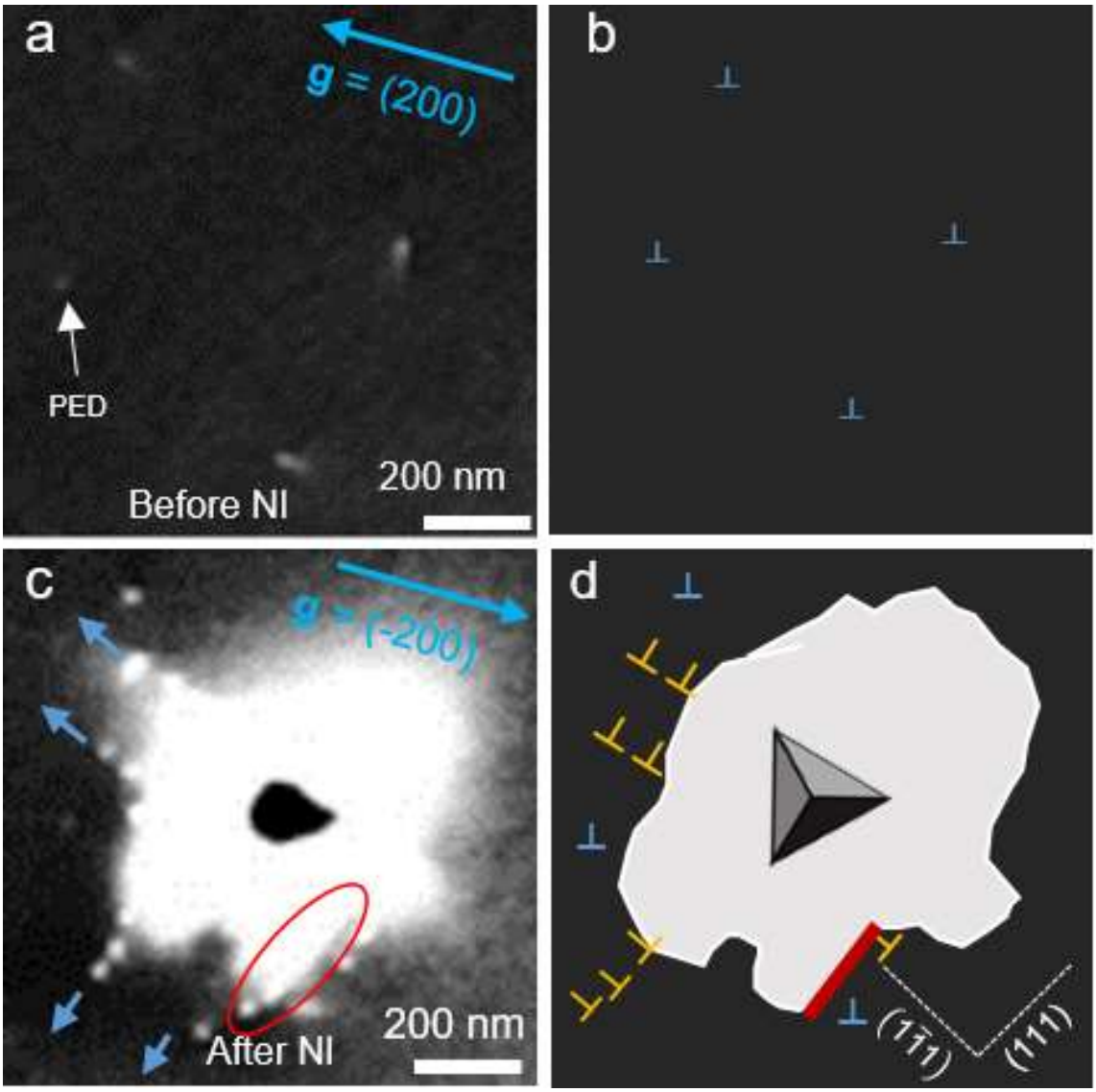

Fig. 4.6. (a) and (c) are ECC micrographs before and after nanoindentation in subgrain A (nanoindent #1). (b) and (d) are schematic representations of (a) and (b), respectively. Note that the symbol ⊥ is used to mark the positions of dislocations and does not refer to their character. The white dashed lines in (d) show the traces of the (111)/(11$\bar{1}$) and (1$\bar{1}$1)/(1$\bar{1}\bar{1}$) planes. The red ellipse in (c) red ellipsis and a thick red line (d) mark the traces of SFs. NI stands for nanoindentation.

The symbols ⊥ used in Figs. 4.6b and d (and in subsequent figures) mark the positions of dislocations and do not refer to their type (since there is no standard symbol for dislocations with a mixed character). The PEDs remained unaltered, probably because these dislocations lie outside the deformed region and do not interact with the newly formed NIDs. The pile-ups of the NIDs are visible on two sides of the nanoindent on the traces of the (111)/(11$\bar{1}$) and (1$\bar{1}$1)/(1$\bar{1}\bar{1}$) planes (blue arrows and yellow dislocations in Figs. 4.6c-d, respectively). The

lengths of these pile-ups, *i.e.*, the distance between the outermost pile-up of dislocations and the center of the remnant nanoindents, are ~0.68 μm and ~0.63 μm, respectively.

The nanoindentation test in subgrain B yielded the same microstructural evolution as in subgrain A (Figs. 4.7). However, the pile-up lengths on the (111)/(11$\bar{1}$) planes were longer (0.73 μm) than that in subgrain A. Also, as opposed to subgrain A, the mean length of the pile-ups on the (1$\bar{1}$1)/(1$\bar{1}\bar{1}$) planes were shorter (0.55 μm), and these pile-ups are located on the opposite side of the nanoindent compared to subgrain A, *i.e.*, top left corner in Fig. 4.6c for subgrain A and bottom right corner in Fig. 7c for subgrain B. The reasons for this difference may be related to the small misorientation between subgrains A and B.

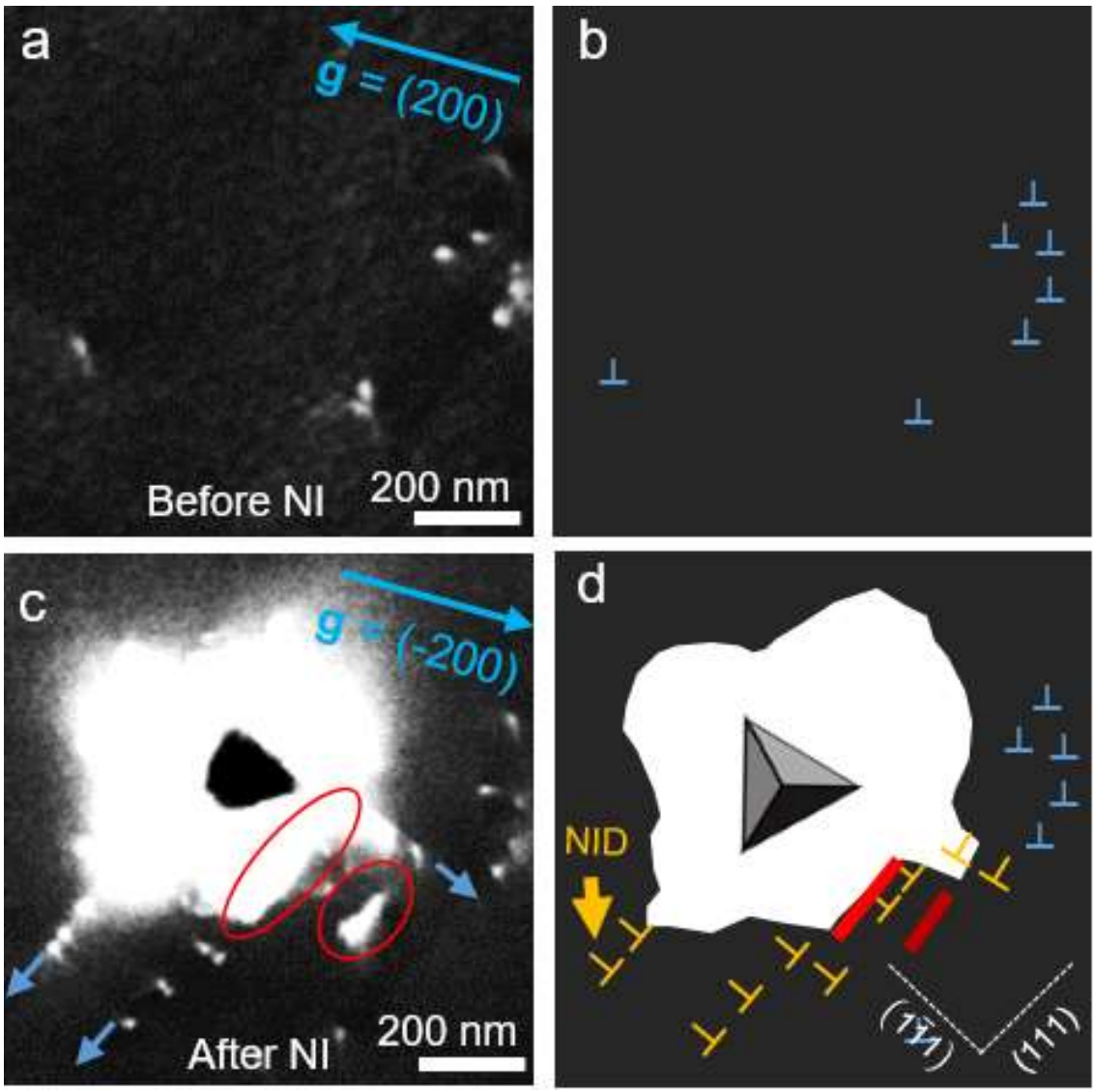

Fig. 4.7. (a) and (c) ECC micrographs before and after nanoindentation within subgrain B (nanoindent #2). (b) and (d) are schematics of (a) and (c), respectively. The meanings of features are the same as in Fig. 4.6 [167].

4.3.2. Micromechanical response and microstructure evolution on the LAGB

When a nanoindentation test is done on the LAGB (Fig. 4.8), the P-h curve deviates from the Hertzian fit early on and does not show a noticeable pop-in (see the black curve in Fig. 4.8b). This micromechanical response probably reflects that, compared to homogeneous nucleation of dislocations inside the subgrains, much lower stress is necessary to activate the gliding of LAGB dislocations [139]. The ECC micrograph around the residual nanoindent supports such interpretation (see Fig. 4.8c). The NIDs around the nanoindent (yellow dislocations in Fig. 4.8d) are randomly distributed, and only two short dislocation pile-ups are observed on one edge of the top left corner of the residual nanoindent. The absence of pop-in on the P-h curve suggests that the plastic deformation occurred suddenly by the motion of the LAGB dislocations.

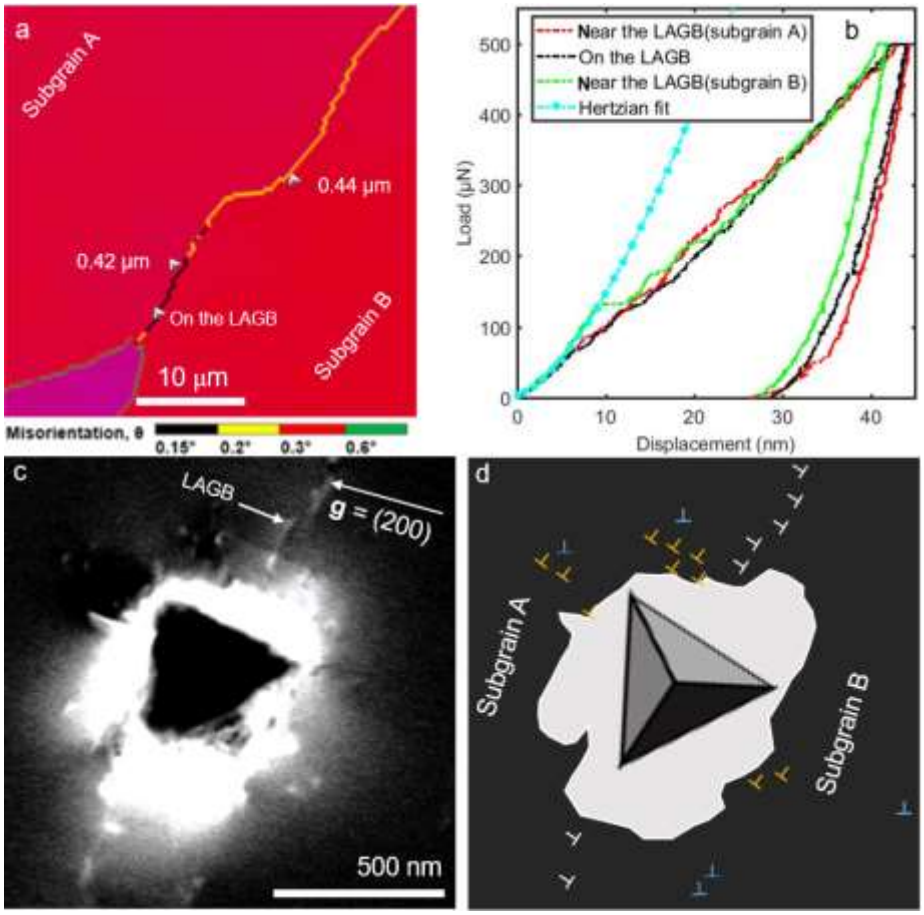

Fig. 4.8. (a) Positions of the nanoindents superimposed on the subgrain orientation map. (b) Load-displacement curves of nanoindentation tests performed at the LAGB (#5), 0.42 µm (R_d = 0.84) from the LAGB in subgrain A (#4), and 0.44 µm (R_d = 0.88) in subgrain B (#3). The initial elastic loading follows the Hertz contact theory (light blue curve). (c) ECC micrograph of nanoindent #5 performed at the LAGB and (d) corresponding schematic. The meanings of features are the same as in Fig. 4.6.

4.3.3. Micromechanical response and microstructure evolution near the LAGB

Nanoindentation tests were performed at ~0.42 µm (R_d = 0.84) from the LAGB in the subgrain A ($\rho = 4.02 \times 10^{12}$ m^{-2}) and at ~0.44 µm (R_d = 0.88) from the LAGB in the subgrain B ($\rho = 4.08 \times 10^{12}$ m^{-2}) to examine the NID-LAGB interactions (see Fig. 4.8a). It should be recalled here that the length of the pile-ups on the $(1\bar{1}1)/(1\bar{1}\bar{1})$ planes in subgrains A and B are over 0.63 µm (Fig. 4.6c) and 0.55 µm (Fig. 4.7c) far away from the LAGB, respectively. Consequently, nanoindentation tests at distances lower than 0.5 µm (R_d < 1) from the LAGB (corresponding to nanoindents #3 and #4) are expected to generate NID pile-ups that will strongly interact with the LAGB. Additionally, a significant micromechanical response is expected. Interestingly, the red P-h curve (Fig. 4.8b), corresponding to the nanoindenter performed in the subgrain A at R_d = 0.84, does not present an initial pop-in and behaves mechanically as the nanoindentation made on the LAGB. On the other hand, the green P-h curve in Fig. 4.8b, corresponding to the nanoindentation in the subgrain B at R_d = 0.88, shows an initial pop-in at 132 µN, which is well below the average value found in Fig. 4.4b.

The ECC micrographs before and after nanoindentation in the subgrain A at R_d = 0.84 are presented in Figs. 4.9a-d. Note that the resolution in Fig. 4.9b is higher than in Fig. 4.9a due to the following reason: a large area near the LAGB (25 × 30 µm^2) was imaged with a reasonable resolution since it is challenging to perform nanoindentation at a specific location with precision. Such imaging is undertaken to reduce acquisition time and avoid severe contamination of the area of interest by the electron beam, *i.e.*, a trade-off between scan time and resolution had to be found. After nanoindentation, smaller areas can be imaged with an enhanced resolution to visualize the deformed microstructure better. The arrangement of the dislocation pile-ups and the presence of SFs were the same as the microstructures obtained for nanoindents performed far away from the LAGB (compare Figs. 4.9b and 4.6c). The pile-up lengths (yellow NIDs in Fig. 4.9d) are ~0.57 µm on both traces of the {111} planes and are 10-16% shorter than those for nanoindents performed within the subgrains (away from the LAGB). A localized change of the LAGB structure is observed between LAGB dislocations 1 and 3 (dashed blue arrows in Figs. 4.9a-d) adjacent to the residual nanoindent. Prior to nanoindentation, the LAGB dislocations 1 and 2 are aligned along the green line depicted in Fig. 4.9c.

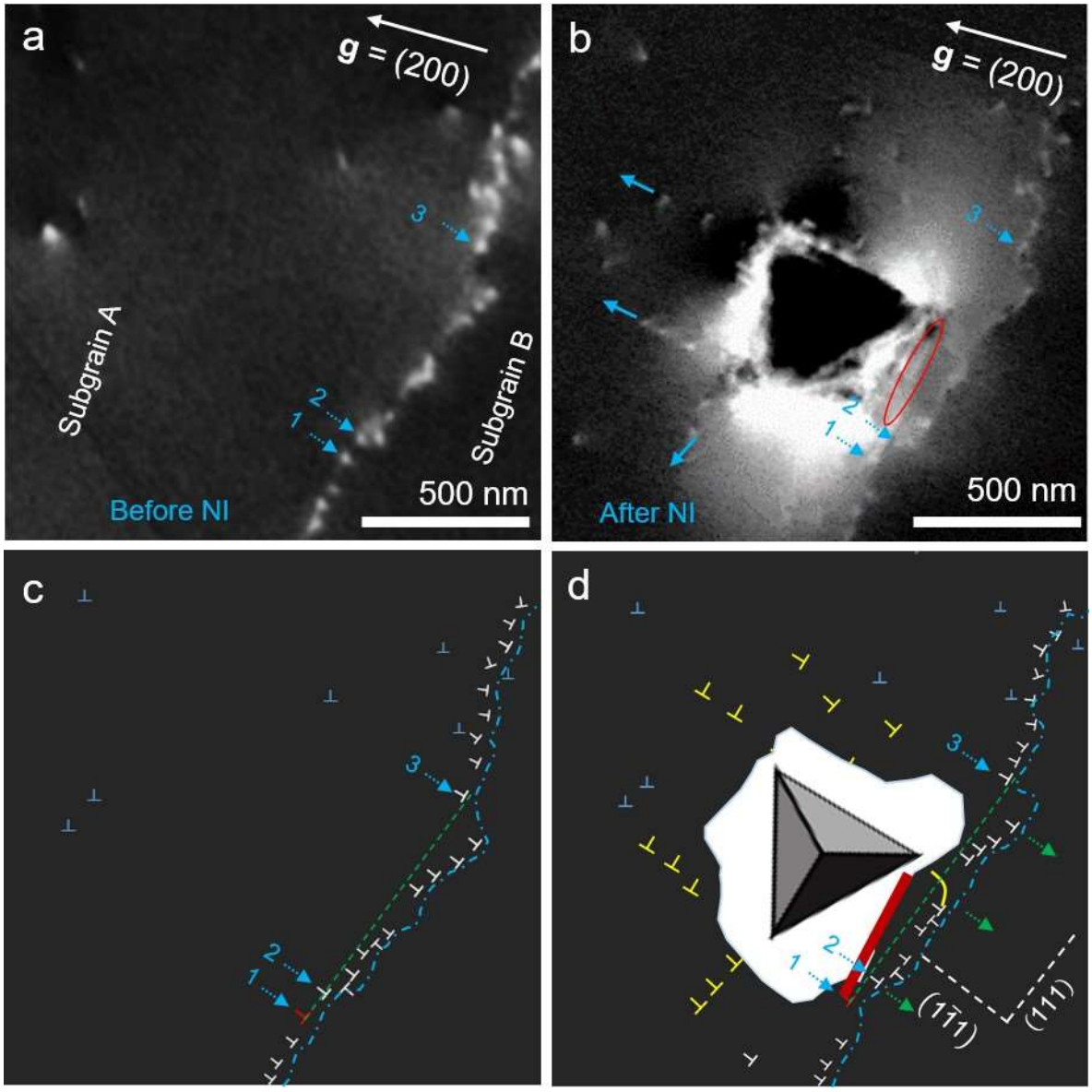

Fig. 4.9. (a) and (b) ECC micrographs before and after nanoindentation, respectively, showing the evolution of dislocation scale microstructure in the subgrain A at 0.42 µm from the LAGB (nanoindent #4 in Fig. 4.4a). (c) and d) are schematics of (a) and (b). The blue dashed lines in (c) and (d) show the trace of the LAGB before and after deformation. The green dashed straight lines allow comparing the positions of the LAGB dislocations 1, 2, and 3 before and after nanoindentation, while the green arrows show the direction of the slight motion of LAGB dislocations. The meanings of the rest of the features are the same as in Fig. 4.6 [167].

After nanoindentation, LAGB dislocation 1 is now at the end of a nanoindentation-induced SF while LAGB dislocation 2 shifted slightly to the right along with other LAGB dislocations between 2 and 3 as illustrated in Fig. 4.9d. In summary, the LAGB adapts to plastic deformation by the glide of its dislocations, and this observation is consistent with the fact that no pop-ins were observed on the P-h curve (red in Fig. 4.8b). Even though the pile-ups of NIDs were not visible on the side adjacent to the LAGB, a new curved dislocation is found between the LAGB

and the nanoindent (see yellow line in Fig. 4.9d). This dislocation may have been stopped by the LAGB or dragged by the LAGB during its movement.

Correspondingly, Figs. 4.10a-b depicts the evolution of dislocation scale microstructure before and after nanoindentation for the nanoindent performed in subgrain B at $R_d = 0.88$. It reveals that the pile-ups of NIDs (blue arrows in Fig. 4.10b) and two SFs (red ellipses in Fig. 4.10b) form on {111} planes. The lengths of the pile-ups are 0.63 µm and 0.57 µm on the traces of $(111)/(11\bar{1})$ and $(1\bar{1}1)/(1\bar{1}\bar{1})$ planes, respectively. The NID on $(1\bar{1}1)/(1\bar{1}\bar{1})$ planes interacted with the LAGB, showing that nanoindentation tests modified, indeed, the dislocation structure of the LAGB. High-resolution ECC micrographs were acquired prior to and following nanoindentation at the location marked with a blue frame (Figs. 4.10a-b) to better observe these developments. Fig. 4.10c-d and their respective schematics in Figs. 4.10e-f indicates positions of individual dislocations where they are numbered from one to nine. As previously mentioned, the resolution of Figs. 4.10b,d is higher than that used for Figs. 4.10a,c. Following nanoindentation, NIDs, illustrated by yellow dislocations in Fig. 4.10f, can be spotted at ~40 nm from the LAGB. The rearrangement and the collective motion of the pre-existing dislocations were due to these NIDs. The rearrangement is evident, particularly between the LAGB dislocations 5 and 8. In this region, the dislocations form a ">" like shape before nanoindentation that widened after nanoindentation (compare ellipses in Figs. 4.10c and 4.10d).

A slight and local collective motion of the LAGB dislocations was observed between dislocation number 1 and 9 away from the residual nanoindent (toward the subgrain A) after nanoindentation (Fig. 4.10d). Moreover, a new NID (highlighted by a red arrow in Fig. 4.10d) was observed in subgrain A (compare Figs. 4.10c-d and 4.6c, 4.7c). Slip mechanisms of decomposition, transmission, absorption, combination, or reflection of NID are not responsible for generating the dislocation above because the number of dislocations remained unchanged in the LAGB [65-67]. The nanoindent at ~0.45 µm from the LAGB had a pile-up length of >0.5 µm. Consequently, the stress at the leading NID of the pile-up was high enough to activate a Frank-Read source in the subgrain A (note that this source cannot be resolved because it is probably smaller than the resolution limit of the A-ECCI method) or its position is more profound than the 100 nm that A-ECCI can image. Alternatively, the new dislocation could have been emitted from the LAGB. It is a noteworthy fact that the low misorientation angle (~0.24°) between the two subgrains ensured that the geometrical criteria for dislocation emission were satisfied [65-67].

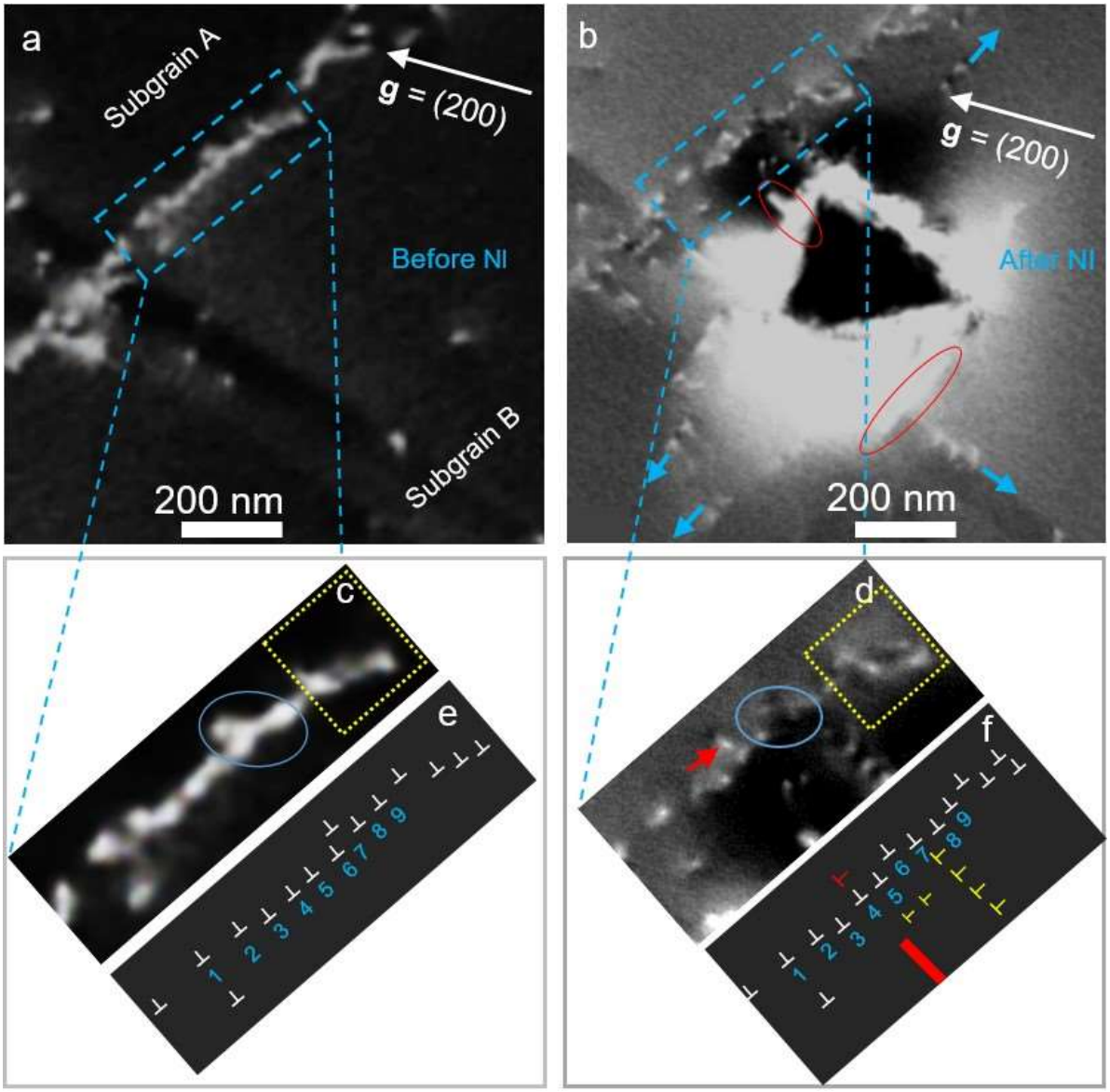

Fig. 4.10. Interactions between NIDs and the dislocations constituting the LAGB. (a) and (b) ECC micrographs before and after nanoindentation, respectively (nanoindent #3 in Fig. 4.4a). (c-d) Enlargement ECC micrograph of a portion of the LAGB before and after nanoindentation and (e-f) are their corresponding schematics. Blue ellipses show dislocations that form a ">"-like shape. The meaning of the rest of the features is the same as in Fig. 4.6 [167].

4.4. Discussion

Through a comparative analysis of P-h curves, the initial pop-in loads, and microstructures for nanoindent performed inside subgrains, near a LAGB, and on the LAGB, it is apparent that the examined LAGB impacts the micromechanical response and basic deformation mechanisms

underlying it. Micromechanical responses underneath a nanoindenter in most situations are dependent on the local microstructure such as defects, phases, and so forth [163], [195]. At the LAGB, which is composed of a distinctive arrangement of dislocations, the incipient plasticity is triggered upon contact by the motion of its dislocations because there is no need to nucleate new ones. This observation explains the absence of an initial pop-in on the load-displacement curve of nanoindent #5 in Fig. 4.8b. On the other hand, nucleation of new dislocations is necessary to initiate plasticity far away from the LAGB, and a sharp pop-in thus marks the elastic-to-plastic transition on the P-h curve.

For the two nanoindents at $R_d < 1$ in both subgrains A and B, their micromechanical responses are significantly different, although they are approximately at the same distance from the LAGB and have been placed in areas with similar dislocation densities before nanoindentation. This discrepancy is due to; first, the local organization (discrete nature, character, and position of dislocations) and local curvature of the LAGB are different for nanoindents #3 and #4, see Fig. 4.4a. Second, both nanoindent are not symmetrical to the LAGB plane, *i.e.*, the tip of the Berkovich nanoindenter was not rotated around its axis between the nanoindentations. Third, deformation mechanisms are also different, as evidenced by the different microstructures around the residual imprints.

It is interesting to note that the nanoindents #5 and #4 (Fig. 4.4a) performed on the LAGB and at $R_d = 0.84$ in subgrain A, respectively, do not present pop-ins (see Fig. 4.8b) and deviate at low loads from the Hertz law early on, even though they show different microstructure evolutions during nanoindentation. For nanoindent #4 at $R_d = 0.84$, the absence of pop-in may be related to the sub-surface structure of the LAGB dislocations. After all, the LAGB may be inclined towards the nanoindentation axis below the sample surface and at a depth higher than the extinction depth of ECCI (~100nm). In this scenario, the stress field below the nanoindenter may have interacted with the inclined dislocations of the LAGB, and plastic deformation may have been accommodated by the motion or multiplication of these pre-existing LAGB dislocations.

The dendritic microstructure of single crystals resulting from different processing routes and parameters has been proposed as one of the factors causing the significant dispersion observed for the macro-mechanical CRSS of HEA and MEA [101], [181]. Our study found that even a LAGB with a misorientation as low as 0.24° hinders the movement of dislocations, alters the local micromechanical response and the associated deformation mechanisms. Therefore, crystal

mosaicity, related to the presence of heterogeneously distributed LAGBs, which induce different misorientation angles within single crystals, is likely one of the factors responsible for scattering macro-mechanical CRSS values reported in the literature.

4.5. Conclusions of the chapter

Both A-ECCI and EBSD analyses revealed that the LAGB of interest has an average $\theta \sim 0.24°$ and is constituted of dislocations aligned along the [001] direction with an average D ~ 60 nm. When nanoindentation tests are performed within subgrains with a maximum load of 500 µN, pile-ups of NIDs form on {111} planes around the nanoindents, and these pile-ups extend at least over ~0.45 µm. Therefore, when nanoindentation tests are performed at ≤ 0.5 µm ($R \leq 1$) away from the LAGB, it is expected that the leading dislocations of the pile-ups interact with the LAGB and the following interactions occurred:

- Incoming lattice nanoindentation-induced dislocations were blocked by the LAGB.
- Incoming lattice nanoindentation-induced dislocations were absorbed into the LAGB plane.
- Incoming lattice nanoindentation-induced dislocations induce the collective and local rearrangement of LAGB.
- Dislocations may have been transmitted across the LAGB, as evidenced by the new dislocation observed following nanoindentation on the other side of the LAGB.

In terms of micromechanical response, the following conclusions are drawn:

- The absence and low pop-in load for nanoindents on or close to the LAGB imply that the pre-existing LAGB dislocations control plasticity.
- The presence of a significant pop-in for nanoindents away from the LAGB at the onset of plasticity depends on local defects' density and configuration.

The LAGB affects the local micromechanical response and fundamental deformation mechanisms, evidenced by pop-ins and microstructural evolutions. The results of this work bring new insights into dislocation/LAGB interactions and their respective micromechanical responses in metallic materials, specifically in HEA and MEA.

5. Experimental and atomistic simulation study of the interactions of dislocations with a twin boundary in the polycrystalline CrCoNi medium entropy alloy.

Abstract

Twin boundaries play an important role in the strengthening of the CrCoNi medium entropy alloy. The experimental study was carried out using a combination of ECCI and nanoindentation. Atomistic simulations employed a combination of ATOMSK, LAMMPS, and OVITO. Experiment observation showed that the twin boundaries accommodated plastic deformation by absorption of dislocations as well as their transmission across it, as proven by geometrical slip transmission criteria. It also showed that, for the same distance of the nanoindents to the twin boundary, mechanisms of dislocation and twin boundary interactions differ from one-twin boundary to another. Such differences have been associated with the orientation of the twin boundary plane. Since the experiment is ex-situ, it is not possible to know what is happening at each stage during nanoindentation. Thus, atomistic simulation has been carried out to dynamically track the interactions of nanoindentation-induced dislocations with a twin boundary. It revealed that interaction mechanisms appeared as force drops on the force-penetration depth (or force-displacement) curve because they were energetically favorable mechanisms. The nucleation of the perfect dislocation appears as an initial force drop and is followed by subsequent force drops that correspond to the formation of stable dislocations structures, absorption of the dislocations into the twin boundary as well as their transmission across the twin boundary.

Résumé

Les macles jouent un rôle considérable dans le renforcement de l'alliage à moyenne entropie de CrCoNi . L'étude expérimentale a été réalisée en utilisant une combinaison d'ECCI et de nanoindentation. Les simulations atomiques ont utilisé une combinaison d'ATOMSK, LAMMPS, et OVITO. L'observation expérimentale a montré que les macles ont accommodé la déformation plastique par l'absorption des dislocations ainsi que leur transmission à travers eux, comme le prouvent les critères géométriques de transmission du glissement. Elle a également montré que, pour une même distance entre l'nanoindentation et la macle, les mécanismes d'interactions sont différentes d'une macle à une autre. Ces différences ont été associées à l'orientation du plan de la macle. L'étude expérimental était ex-situ. Donc, il n'est pas possible de savoir ce qui se passe à chaque étape de la nanoindentation. Ainsi, une simulation atomique a été réalisée pour suivre dynamiquement les interactions des dislocations induites par la nanoindentation avec le joint de macle bien défini. Elle a révélé que les mécanismes d'interaction apparaissaient comme des chutes de force sur la courbe force-profondeur de pénétration (ou déplacement) car ce sont des mécanismes énergétiquement favorables. La nucléation de la dislocation parfaite apparaît comme une chute de force initiale et est suivie de chutes de force ultérieures qui correspondent à la formation de structures de dislocations stables, à l'absorption des dislocations dans le TB ainsi qu'à leur transmission à travers la macle.

5.1. Introduction

TBs play an important role in the strengthening of FCC materials with a low stacking fault energy such as CrCoNi MEA [21]. It was postulated that TB may have a strengthening effect similar to the general GBs [21]. A wide range of studies using diverse experimental methods and atomistic simulations has been performed to investigate lattice dislocation-TB interactions in conventional FCC metals and alloys [2], [66], [158]. Lim *et al.* [59] observed the direct transmission slip across coherent twin boundaries due to cross slipping of screw dislocations in Ni at 587 K. Lee *et al.* [66] proposed that such direct transmission occurs when slip systems in grains 1 and 2 across a TB share a common line of intersection. Moreover, the dislocation should have a screw character and the dislocation line should be parallel with the interaction line. Couzinié *et al.* [6] also observed the integration of the Shockley partial dislocations within the TB by either their separate reaction or recombination involving a constriction in the deformed pure single crystal of Cu using TEM and the contrast simulation technique.

Atomistic simulations provide additional parameters that govern slip or dislocation transmission across TBs. Zhu *et al.* [196] observed that energy barrier, orientation and magnitude of the applied stress, and stacking fault energy control dislocations reactions at the TB. They ascertain that partial dislocations are easily nucleated and can cross slip into the TB with small energy barriers in low stacking fault energy materials. In these materials, the leading partial is transmitted across the TB leaving the trailing partial in the initial grain. Wang *et al.* [197] also found that the atomic structure of the twin boundary can control the passage of dislocations across an asymmetrical coherent twin boundary. Moreover, the details of the atomic potentials used for the simulations can also affect the slip transfer, as found by Chassagne *et al.* [67] while studying non-screw lattice dislocations-coherent twin boundaries interactions in FCC materials. They found that dislocations are absorbed into the TB when the resolved shear stress is below a certain value. Additionally, dislocations cross the TB when the resolved shear stress is above the critical value. Such critical shear stress was independent of the atomic potential.

It has been postulated that twins provide strengthening as much as other general HAGBs in the strengthening of the CrCoNi MEA [21]. However, little has been done to investigate plasticity transmission across the twin boundaries in this alloy. Consequently, this study examines the interactions between lattice dislocation and annealed TBs in a CrCoNi MEA using nanoindentation and ECCI. Moreover, atomistic simulations using MD were used, to

dynamically track the evolution of dislocations over time and their interactions with the TB. Additionally, distinct micromechanical responses associated with each interaction mechanism are explored.

5.2. Experimental study

A sample of polycrystalline CrCoNi MEA that has been thermomechanically processed followed by recrystallization has been used in this study (see section 2.2.1).

5.2.1. Microstructure

The BSE micrograph of the polycrystalline CrCoNi MEA highlights randomly oriented grains, grain boundaries, and twin boundaries (Fig. 5.1a). Two to Four annealing twins are, on average, in each grain, if it is assumed that the grains are surrounded by HAGBs ($\theta > 10°$). Laplanche et al. [19] density found that around 2.5 ± 0.1 twins per grain. Moreover, analysis of the GB distribution revealed that ~50% of the GBs are TBs if LAGBs ($\theta < 10°$) are omitted (Fig. 5.1b). The average grain size obtained using the linear intercept method was 33.5 μm without considering annealing TBs and 13 μm with annealing TBs. Slone et al. [89] obtained a fraction of annealing twins of 30% and an average grain size of 24 μm (excluding annealing TBs) for a sample of CrCoNI MEA that have been cold rolling to a reduction of 70% followed by recrystallization. Miao et al. [88] also found that 32% of boundaries are annealing twins and an average grain diameter of 13 μm(excluding TBs) for a cold-rolled (19.1mm to 1.8mm) and annealed (1198K for 1h) sample.

EDS spectra obtained from the sample revealed that the alloy comprises Co, Ni, and Cr elements. EDS CrCoNi, Co, Cr, and Ni maps (Fig. 5.2b-e) reveal the distribution of chemical elements in a SE micrograph in Fig. 5.2a. All maps show a uniform and homogeneous Cr, Co, and Ni elements distribution. The EDS line also analysis showed no segregation of elements at any particular boundaries (Fig. 5.2f). The composition of the alloy was 31.81Cr-34.33Co-33.85Ni (at. %) and was measured using the map in Fig. 5.2b.

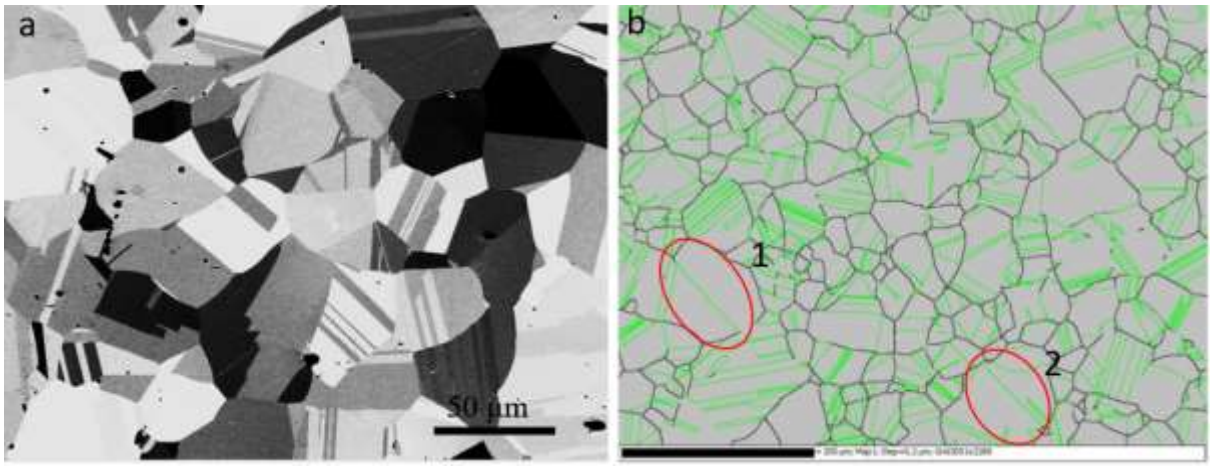

Fig. 5.1. CrCoNi MEA (a) BSE micrograph and (b) misorientation map (black lines are grain boundaries, and the green line is Σ3 twin TB. Two red ellipses highlight the two TB chosen for the study.

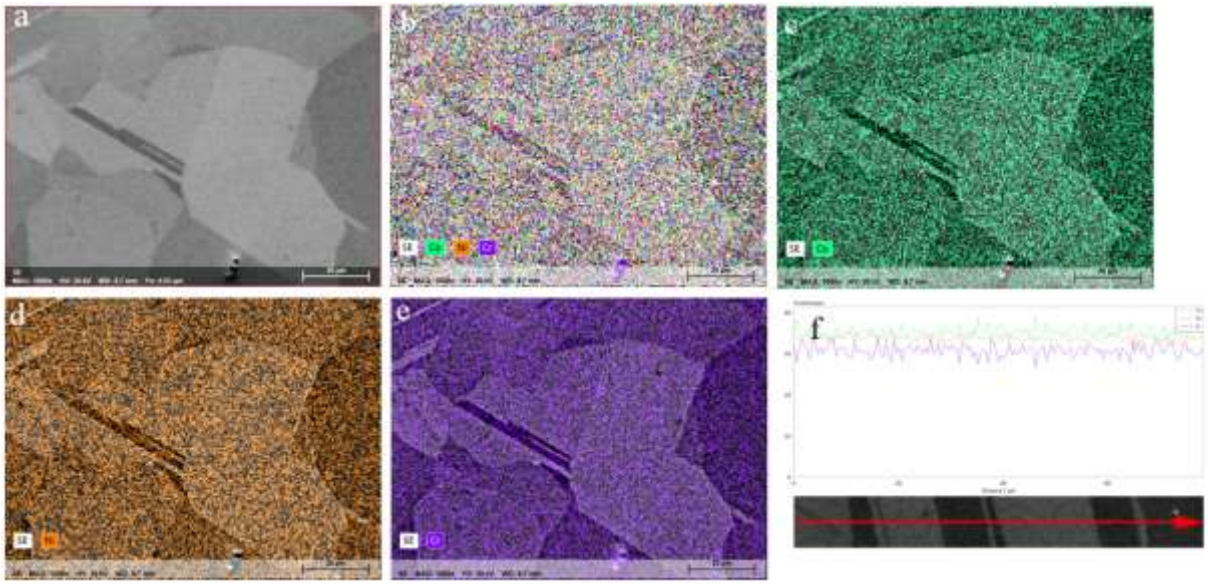

Fig. 5.2 (a) SE micrograph of CrCoNi, (b-e) Correponsiding EDS map of CrCONi, Co, Cr, and Ni elements, (f) EDS line analysis.

5.2.2. Twin boundaries of interest and nanoindentation

Almost 50% of boundaries in recrystallized CrCoNi MEA are TBs. The number of TBs in each of the grains is in the range of 2-10. Two TBs were chosen for this study and shown by the two large red ellipses in Fig. 5.1b. The reasons for choosing these two TBs were that they were in large grains and they were no other TBs close to them.

5.2.3. Nanoindentation in the grain.

The dislocation density in the sample was very low. Thus, nanoindentation was carried out inside the grain to induce dislocation with aim of characterizing it. During nanoindentation, the maximum achievable load was 2 mN using the Berkovich nanoindenter tip. The loading and unloading rate was 4 mN/min with a hold of 5s at the peak load. Fig. 5.3a displays four **g** used for acquiring ECC micrographs (Figs. 5.3b-e). The latter shows dislocations and stacking faults due to nanoindentation lying along specific traces of slip planes that correspond to FCC structure. The longest pile-up of dislocations in Figs. 5.3b-e occurred along (1-11) slip trace, and its length is 2.51 µm. Due to high deformation near the center of the nanoindent, dislocations are randomly distributed.

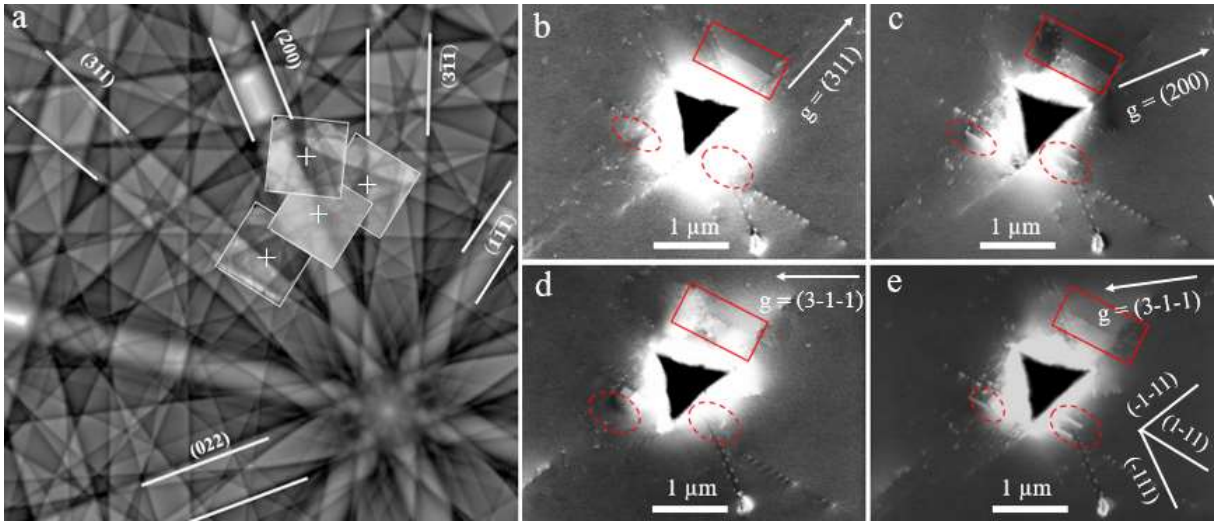

Fig. 5.3. (a) High resolution selected area channeling patterns (HR-SACP) acquired in the region of interest overlaid on the dynamically simulated pattern, (b-e) ECC micrographs acquired using four diffraction vectors, **g** (their respective HR-SACPs are shown 5.3a).

In Figs. 5.3b and e, stacking faults occurred along (1-11) slip traces. The extinction criterion for the stacking fault is **g. R** = 0 where **R** is 1/6<121> for Shockley partials. Given that (1-11), they may have resulted from the dissociation of 1/2 <011> dislocations. Thus, **R** = 1/6 <-112> for **g** = (311) or **R** = 1/6 [121] for **g** = (3-1-1). The two **R** correspond to partial dislocations that make perfect dislocations on (1-11) planes as follow: 1/6 [-121] + 1/6 [112] = ½ [011].

5.2.4. Slip transmission across a TB and a step

5.2.4.1. Procedure for slip transfer analysis

EBSD map of the region of interest was acquired to obtain the approximate orientation of the TB of interest and adjacent grains, *i.e.*, its Euler angles of the grains and the TB plane. ATEX

software [119] was used to obtain the orientation of theoretical slip traces from an EBSD map in each grain. Experimental possible slip traces were obtained by ECC micrographs. They are given by pile-ups of NIDs. ATEX's theoretical slip traces and pile-ups on the ECC micrographs are overlaid to predict which are the few possible slip systems interacted with the TB or the step. The TB was reconstructed using STABIX built-in Matlab program using grain and TB orientations [44]. The trace of the TB is segmented into various small segments depending on the local orientation. At each segment, incoming and outgoing slip traces are extracted. Each slip trace is assigned a number, as shown in Table 1.1. Various incoming and outgoing slip systems are used to calculate slip transfer parameters: m' Luster-Morris parameter, N-factor, and Schmidt factor (M).

5.2.4.2. Slip transfer across a twin boundary or a step (Region 1)

Figure 5.4a shows the EBSD map with a TB and a step of interest. From the EBSD map, theoretical slip plane traces can be extracted with the help of the ATEX software [119]. It is should be noted that the grain interior analysis by the ATEX software does not provide an orientation of the slip direction. Using EBSD orientation data, the Matlab-based STABIX using used to reconstruct the TB by segmenting it into small segments. 40 segments numbered from 1 through 40 were obtained as shown on Fig. 5.4b. Nanoindents were positioned at 0.2 µm, 0.4 µm, and 0.5 µm from 17, 16, and 8 segments, respectively. Segment 17 is a step and is a white broken ellipsis in Fig. 5.4a.

The SE micrograph (Fig. 5.5a) and its schematic depiction (Fig. 5.5c) display slip traces due to nanoindentation close to the trace of the step (segment 17) and the trace of TB (segment 16). The pile-ups of dislocations along the incoming and outgoing slip planes are represented by the ECC micrograph (Fig.5.5b) and its schematic representation (Fig. 5.5d). There are few outgoing pile-ups, although there are many pile-ups of incoming dislocations, meaning that the TB interacted with the incoming dislocations.

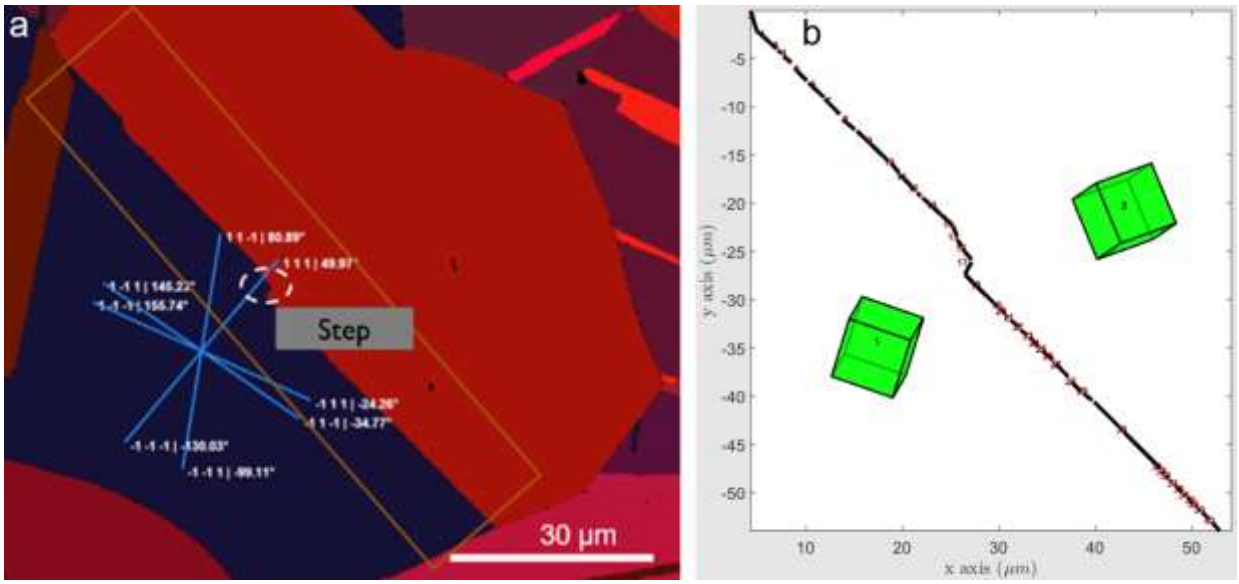

Fig. 5.4. (a) EBSD map of the TB with step and slip traces in grain 1. (b) Segmentation of the TB into a different segment. The white ellipse encloses a step.

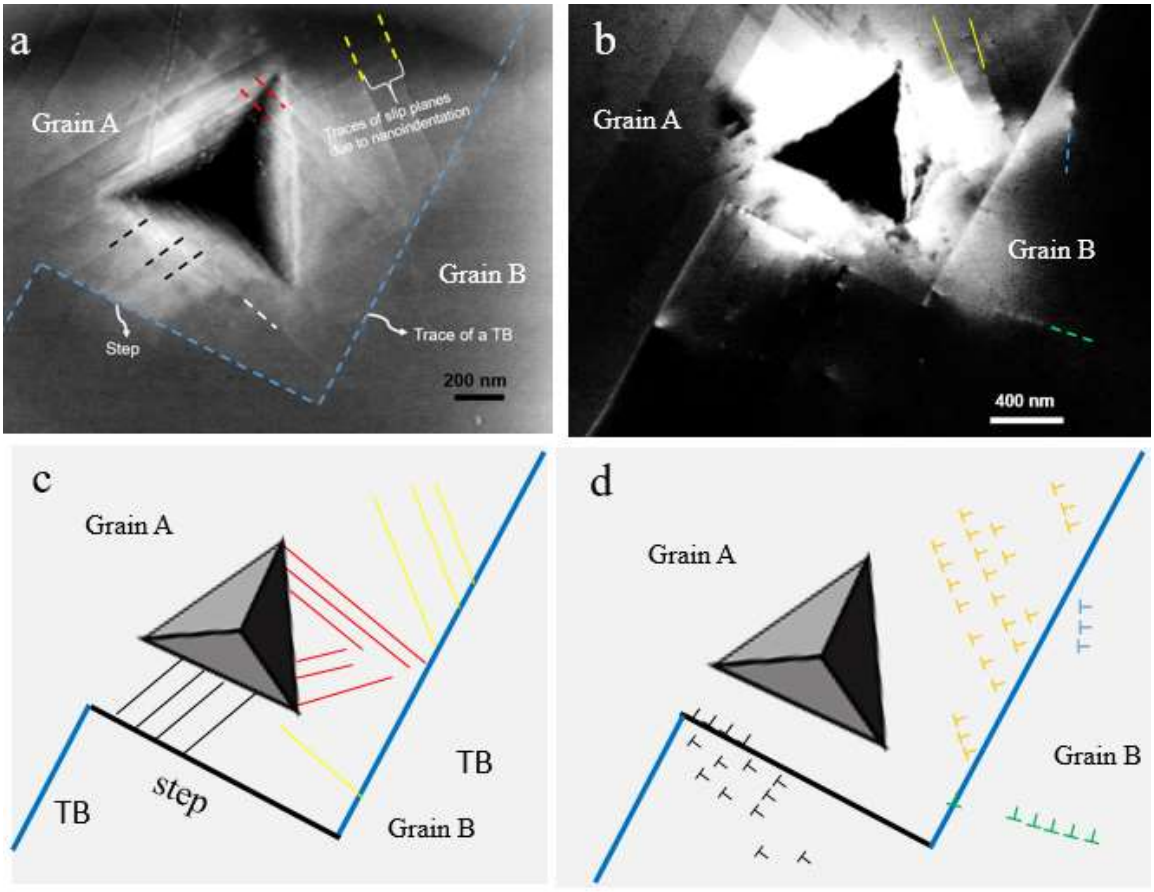

Fig. 5.5. (a) and (c) SE and ECC micrographs of the nanoindent near a step on a TB, (c) and (d) the schematic representations of (a) and (b). Note that the symbol ⊥ is used to mark the positions of dislocations and does not refer to their character.

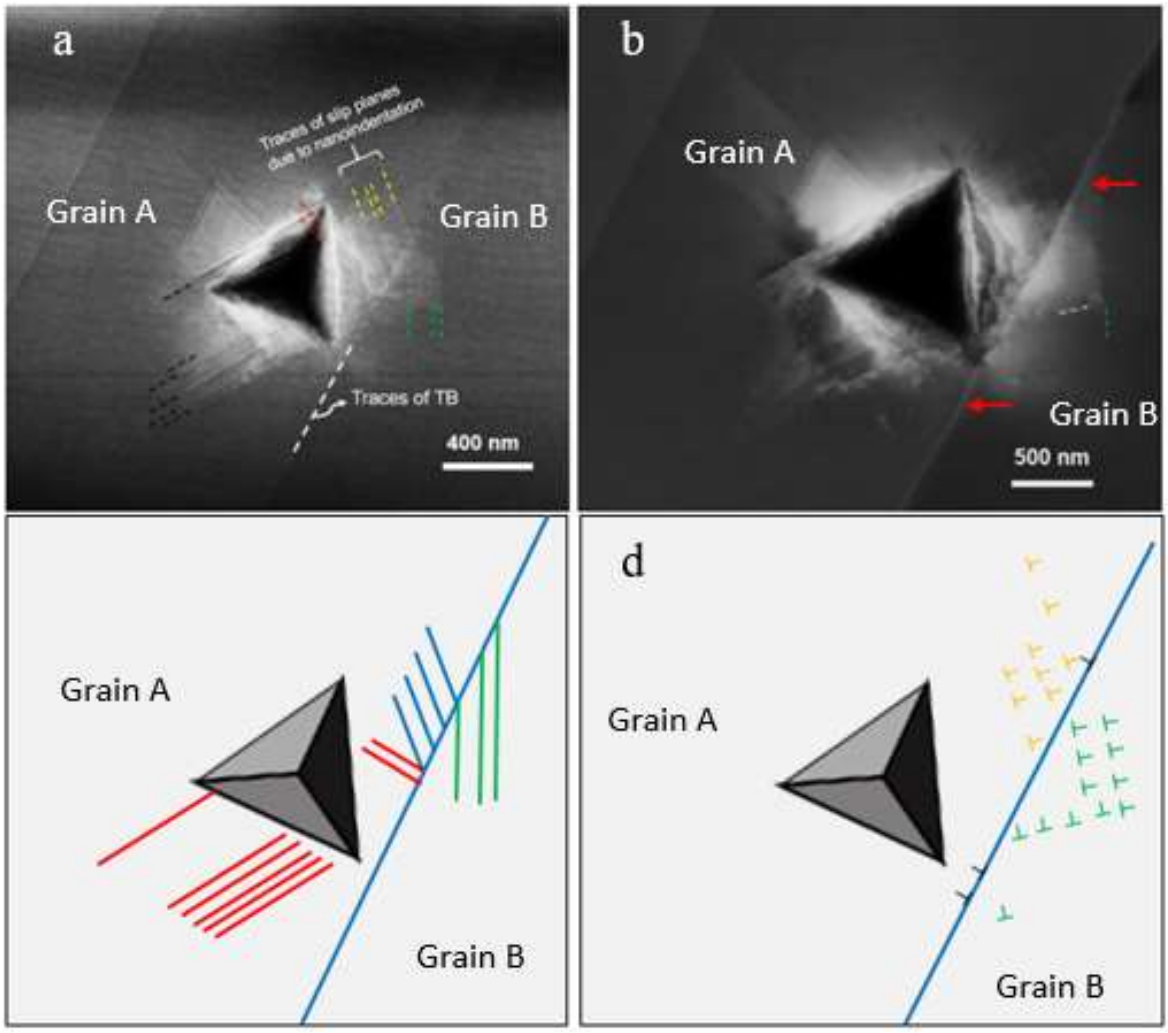

Fig. 5.6. (a) SE and ECC micrograph of a nanoindent at 0.5 µm from the TB (near segment 8 of Fig. 5.4b), (c) and (d) are micrographs (a) and (b), respectively.

Similarly, the SE micrograph (Fig. 5.6a) and its schematic depiction (Fig. 5.6c) indicate slip traces in both grain A and grain B while the ECC micrograph (Fig. 5.6b) and its schematic depiction (Fig. 5.6d) display pile-ups along the slip traces. Distortion of the traces of TB is observed between the two red arrows. The ECC micrographs are overlaid on the EBSD map with slip traces generated by ATEX to obtain the slip plane associated with each pile-up. However, the slip direction remains unknown. In FCC materials, each slip plane has three possible slip directions [29], *i.e.*, each incoming or outgoing slip plane has three possible directions. Nine combinations of incoming and outgoing slip planes are used in each case if the incoming and outgoing slip traces are known to determine the slip direction. The latter is obtained as the combination of incoming and outgoing slip systems with the maximum N and m' values calculated using STABIX code. The results of the calculation for three combinations with the highest values of geometrical slip transmission criteria are tabulated in Table 5.1.

Based on the latter, the best combination of incoming and outgoing slip systems are (11, 7) or ((111)[-110], (111)[-101]) for the segment 17 and (6, 11) or ((-1-11)[101], (111)[-110],) for the segment 16 and (4,5) or (-111)[0-11], (-111)[101] for segment 8 .The differences between outgoing and incoming **b** are non-zero, i.e., there are slip transfers with residual burgers vector into the TB (indirect slip transfer).

Table 5.1. Calculated slip transmission parameters for nanoindenter near a TB with a step (the numbers for n_{α}^{A} and n_{β}^{B} have been extracted from Table 1.1 for slip systems in FCC as incorporated in STABIX).

	n_{α}^{A}	n_{β}^{B}	Abs (m')	Abs (N)	Abs (M)
Segment 17	11	7	0.7777	0.7777	0.4279
	10	8	0.6482	0.3521	0.0416
	12	9	0.6480	0.3513	0.3863
Segment 16	6	11	0.7791	0.7791	0.2330
	5	12	0.6501	0.3556	0.2191
	4	10	0.6499	0.3548	0.0139
Segment 8	4	4	0.4631	0.3163	0.0139
	4	5	0.4627	0.5368	0.0139
	5	5	0.4620	0.3123	0.2191

5.2.4.3. Slip transfer across a TB (region 2)

A series of nanoindents was placed around a straight TB in region 2 (Fig. 5.1b). Interactions between nanoindents and TB in grain 1 were different from those in grain 2. A representative nanoindent within grain 1 at 660 nm from the trace of TB on the surface and its schematic are representative in Fig. 5.7. For this nanoindent, one edge of the residual imprint is within ~0.1μm of TB. The ECC micrograph does not show pile-ups of dislocations that have interacted with the TB. Instead, the pile-ups of dislocations were found in grain 2 because of the nanoindentation in grain 1. The NIDs were along (11-1) slip traces in grain 2 and white arrows in Fig. 5.7a show directions of their motion. A schematic representation in Fig. 5.7b displays one of the possible orientations of the TB to the nanoindent.

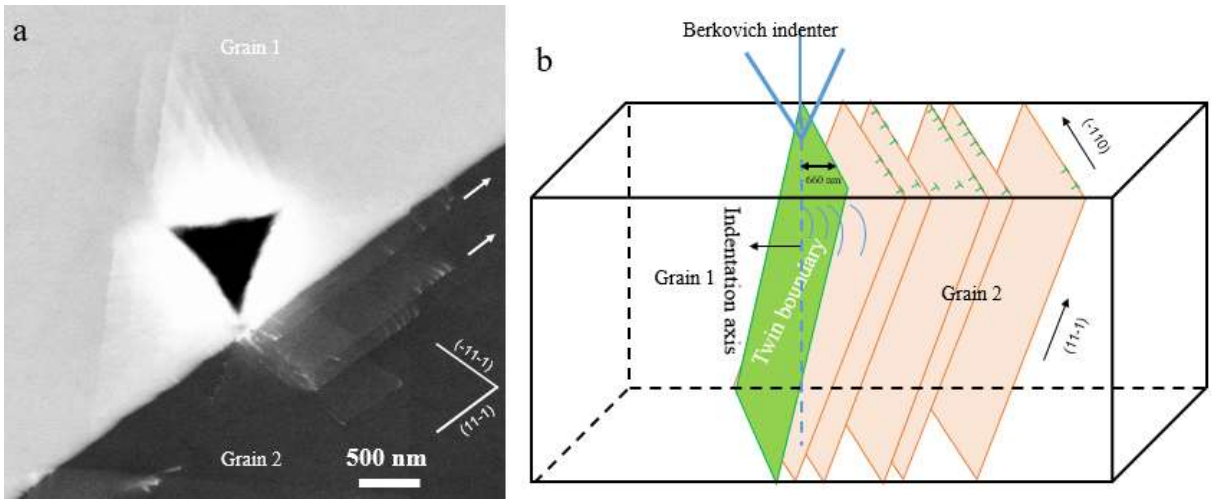

Fig. 5.7. (a) A nanoindent placed at 0.6 µm from the twin boundary, (b) one of the possible schematic representations of (a).

The nanoindents in grain 2 also interacted with the TB to induce dislocations in grain 1. For a nanoindent at 2.5 µm from the TB, the longest pile-up of NIDs is parallel to the TB (see the yellow arrows in Fig. 5.8a). Thus, there is no interaction of dislocations with TB. For the nanoindent at 0.9 µm and 1µm from the TB (Figs. 5.8b-c), some pile-up NID were stopped at the TB which is shown by a slight variation of the contrast of the TB near the residual imprint compared to other regions of the TB. The nanoindent at ~0.6 µm from the TB in grain 2 (Fig. 5.8d) induced pile-ups of dislocations and stacking faults on different slip traces as well as spatially random dislocations closer to the center of the nanoindenter. A pile-up of dislocations is observed in grain 2 as highlighted by the magnified micrograph in Fig. 5.8di. However, it is not clear which pile up in grain 2 is responsible for inducing pile up in grain 1. Moreover, the contrast of the TB is also similar to the one for nanoindent at 0.9 and 1 µm from the TB implying the absorption of dislocations into the TB.

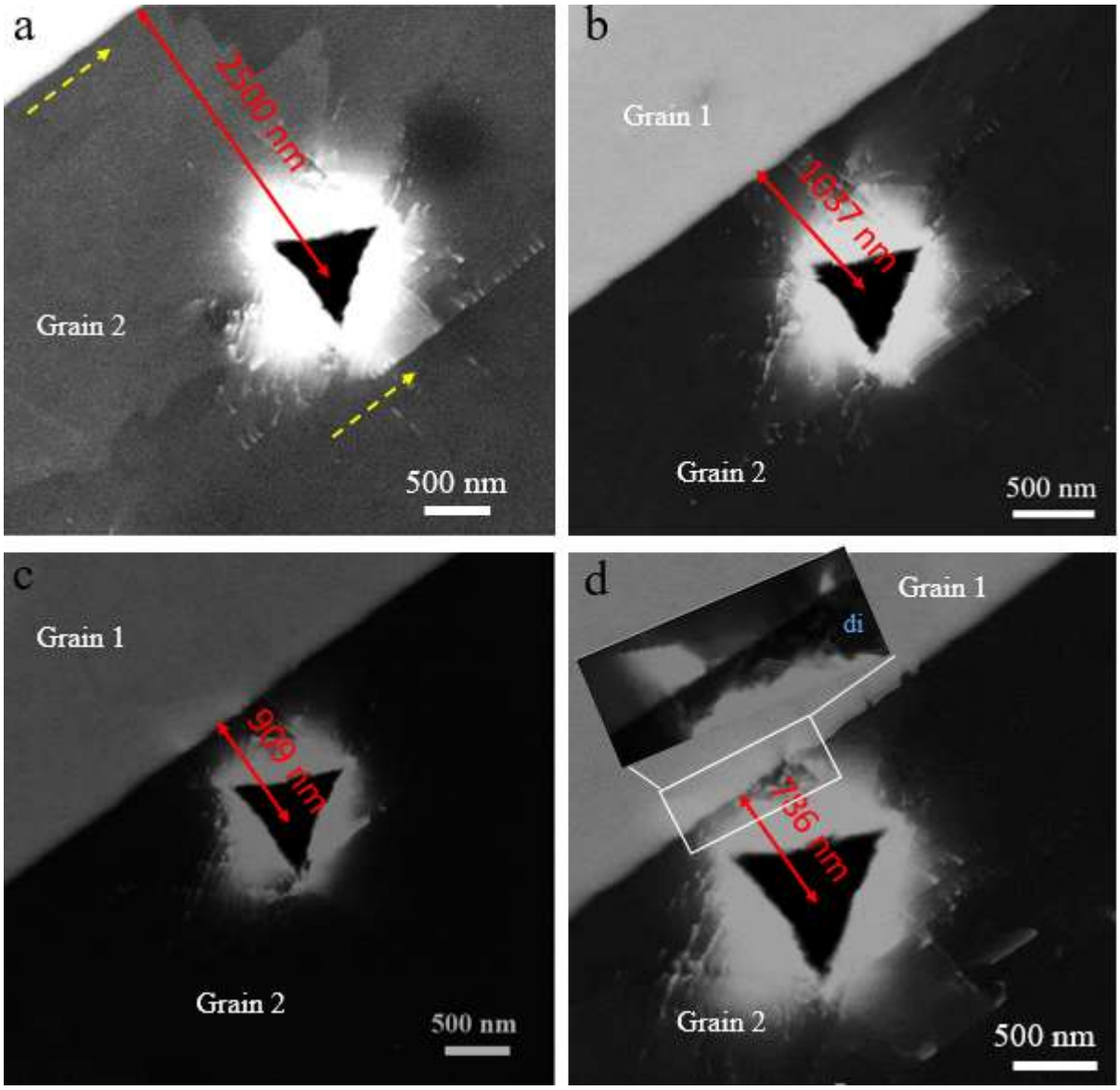

Fig. 5.8. (a) Nanoindent at various distances from the TB showcasing pile up interacting with the TB.

5.3. Atomistic simulation study

The above *ex-situ* ECCI provided microstructures before and after nanoindentation. However, it fails to provide the evolution of the microstructure over time. To account for the latter, atomistic simulations have been used in the literature to dynamically investigate the mechanisms of formation of defects and their subsequent interactions with different boundaries [74]. In this context, atomistic simulation was used in this study to examine the mechanisms of formations of lattice dislocations and their interactions with well-defined twin boundaries in the CrCoNi MEA.

5.3.1. Generating atomistic data

Simulation cells (digital atomic samples) have been built using open-source software called "Atom, Molecule, and Material Software Kit" (ATOMSK). ATOMSK is a multipurpose command-like program used to create, manipulate, and convert atomic data files. It can be run on local computers or remote clusters to generate input files or convert data files produced by a simulation [198].

Experimental EDS analysis has revealed that the CrCoNi alloy is made of a quasi equiatomic percentage of Cr, Co, and Ni elements (see chapter 3).To achieve that, ATOMSK is initially used to build a structure with only Ni atoms (Fig. 5.9a) because it is FCC. Once the size and number of atoms in the simulation cell's required size are achieved, one-third of Ni atoms are replaced by Cr atoms and another one-third by Co atoms to produce a multicomponent structure (Fig. 5.9b). The atoms of Ni, Cr, and Co of equal ratios of 33.33% are randomly distributed over the lattice points of an FCC structure. For a small number of atoms, *i.e.*, less than 100 000, the conversion from Ni structure to CrCoNi structure took a reasonable time (5-30min). However, it took a couple of hours when the number of atoms was higher than 1000 000. Thus, a LAMMPS script was written to replace two-thirds of Ni atoms with an equal number of atoms of Cr and Co. Such a script allows the creation of a structure of 4000 000 atoms in 15 min instead of 3 hours on a local computer.

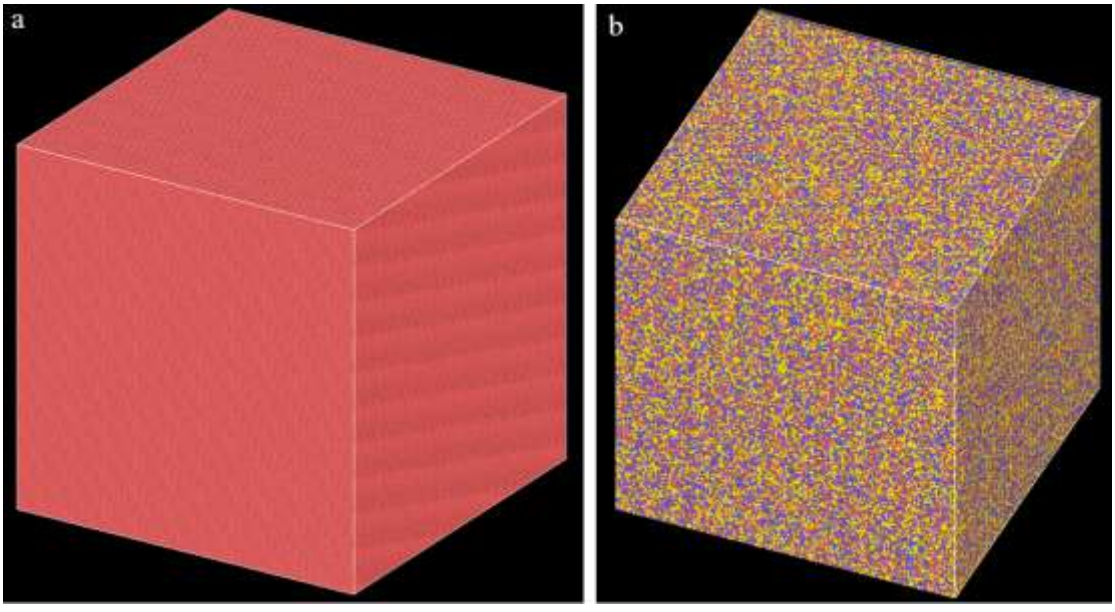

Fig. 5.9. (a) structure with only Ni atoms, (b) A structure of an equal number of atoms of Cr, Co, and Ni making a multicomponent CrCoNi medium entropy alloy. These structures were built using ATOMSK.

To validate the structure of the multicomponent CrCoNi alloy, cohesive energy, and a lattice parameter were determined and compared with the literature. Cohesive energy (E_{coh}) is the amount of energy required to break atoms of a solid into its constituent isolated atomic species. It is calculated from the relation:

$$E_{coh} = E_{solid} - \sum_i E_i^{isolated} \quad (5.1)$$

where E_{solid} is the energy of a solid and $E_i^{isolated}$ is the energy of an isolated atom I [199]. Using ATOMISK and LAMMPS, four simulation cells were created with periodic boundary conditions in all three directions. Two simulation cells with the same number of atoms differ only from the random seed, resulting in different arrangements of atoms in the simulation box. The sample was minimized using the conjugate gradient algorithm to obtain the minimum energy of the system. The average cohesive energy per atom for this allow was calculated and is equivalent to – 4.32 eV/atom. This value is in the range of E_{coh} obtained by ref. [200] for CrCoNi FCC solid solution (SS) (Fig. 5.10). The calculated lattice parameter was 3.56 A°. The values of the experimental lattice parameter of CrCoNi MEA have been reported to be between 0.356 and 0.357A° [19], [84], [85].

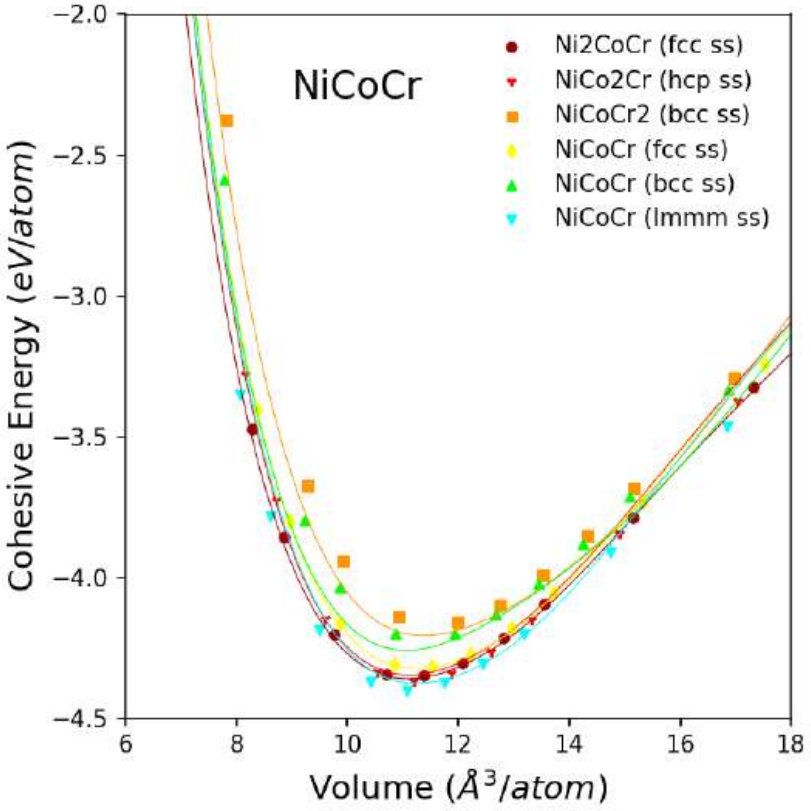

Fig. 5.10. The cohesive energies of selected CrCoNi solid solutions as a function of volume [200].

The TB of interest was extracted from the experiment. Grains 1 and 2 (region 2 in Fig. 5.1b) adjacent to the TB have (194.81°, 30.76°, 189.5°) and (82.73°, 28.22°, 257.3°) as orientations in Bunge notation, respectively. The miller indices of each grain are obtained from these Euler angles and the orientation matrix function. The first and third columns of Miller indices of each grain represent vectors parallel to the rolling and normal directions (RD and ND, respectively), as shown in Fig. 5.11a. It is possible to determine the two-dimensional twin boundary trace orientation from the angle α. In this case, the normal to the TB is calculated using RD and TD of either grain 1 or grain 2 (TB is assumed to be perpendicular to the observation surface). Using grain 2, the normal of the traces of the TB is [1-11] in the crystal coordinate frame and is obtained using the transformation matrix below:

$$\begin{pmatrix} \cos\alpha & \sin\alpha & 0 \\ -\sin\alpha & \cos\alpha & 0 \\ 0 & 0 & 1 \end{pmatrix}$$

Where α is 45°, the direction of the trace of TB is [-112]. The perpendicular direction to the above two directions is obtained using a cross product and is equal to [-1-10]. Thus, simulation cells with orientation in X= [-112], Y= [1-11], and Z= [-1-10] containing a TB were built using ATOMSK. Fig. 5.11b shows the simulation cell containing a TB with three-dimensional periodic boundary conditions. The simulation cells were large enough to avoid the interactions between two TBs. The energies of the TBs were determined using a LAMMPS script that generates the total energy of a minimized structure (E_{TB}). They are calculated using the following relation:

$$E_{TB} = (E_T - NE_c)\ (\frac{1}{2A_{TB}}) \tag{5.2}$$

E_T is the total energy, E_c is the cohesive energy, N is the number of atoms and A_{TB} is the area of the TB. The number two means two TB in the simulation cell, as shown on Fig. 5.11b. Based on the relation in Eq. 5.2, the energy of the bulk without a TB is zero. However, the energy in the area of TB is non-zero. Results for TB revealed that the TB in CrCoNi MEA has an energy of 3487 mJ/m^2. Such energy is higher than 500 mJ/m^2 obtained in Ni or Al. However, to the best of our knowledge, there are no other studies on TB energy in CrCoNi MEA to compare with ours.

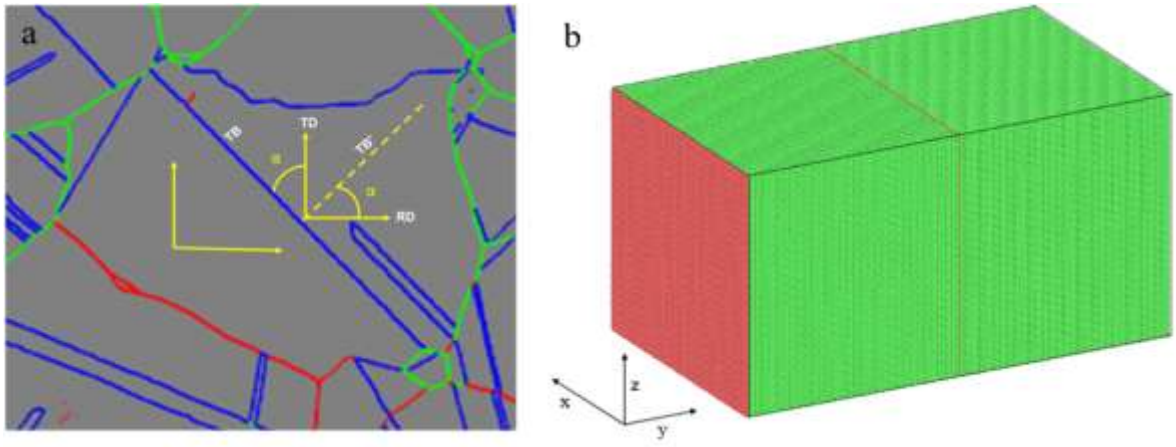

Fig. 5.11 (a) The orientation of the TB from the experiment used in the simulation. (b) Simulation box with two twin boundaries.

5.3.2. Virtual nanoindentation

A virtual nanoindentation test was performed on a simulation cell with 1400 000 atoms and a dimension of 21.5 nm x 36.5 nm x 20.3 nm. The energy minimization was performed on the simulation cell before nanoindentation using periodic boundary conditions in the X and Y directions and a non-periodic boundary condition in the Z direction. The normal to the TB plane is parallel to X and is at a half distance (Fig. 5.12). The nanoindenter is spherical with a radius of 3.5 nm. The spherical nanoindenter was displacement-controlled, and the maximum depth that the nanoindenter reached was 3.2 nm over a period of 350 ps. Thus, the rate of nanoindentation during loading of nanoindentation test was 10m/s. Only the loading curve was generated because the main objective of this test was plastic deformation near the TB, and unloading would not provide helpful information despite taking the same computing time as the loading curve. The dynamics of simulation cells were evaluated by integrating the Newtonian equations of motion using the Verlet with a time step of 0.001ps.

The bottom of the simulation box was fixed, *i.e.*, the thickness equivalent to 2 atomic layers (1.5 nm) to prevent Z from moving down under stress due to nanoindentation. The nanoindentations were placed at 9 nm, 4.5 nm, 3 nm, and 1 nm from the TB along the Y-axis for a fixed distance X equivalent to X/2.

Force-displacement curves were generated by plotting the force exerted by the nanoindenter against the distance traveled by the nanoindenter during nanoindentation at 0.001 nm intervals. The extracted force from the simulation is in eV/nm. Consequently, it is converted into nN by multiplying the result from the simulation by 16.0217733 (1ev = 1.60217733 x 10^{-19} N m and 1 nm= 10^{-9}m)

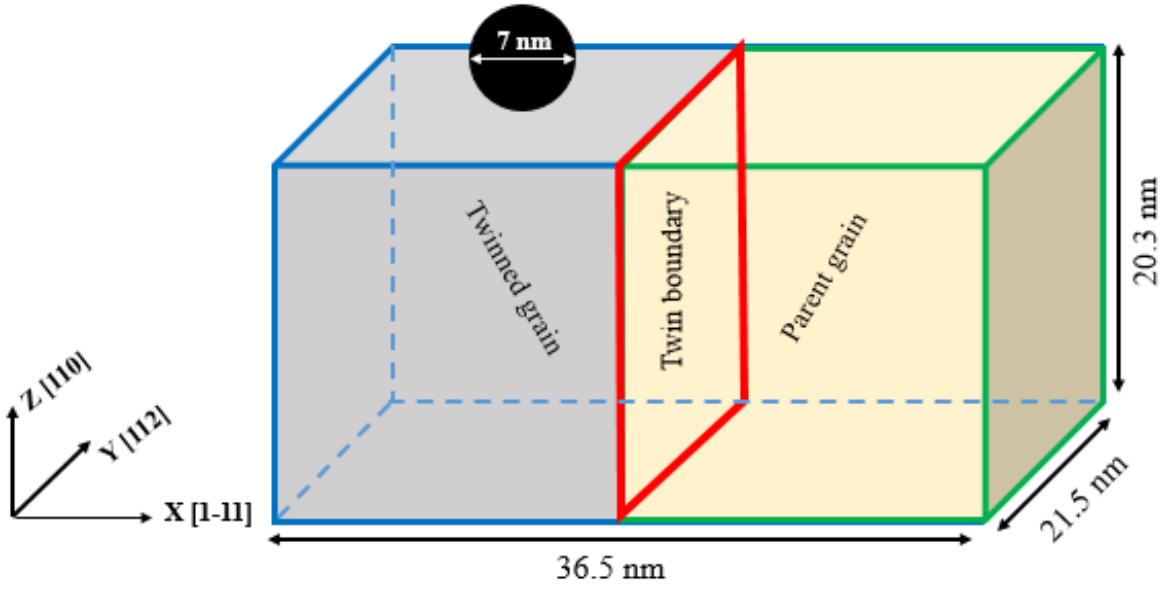

Figure 5.12 (a). A schematic of the structure used for nanoindentation. The orientation of the TB is mimicked with the experimental one.

5.3.3. Virtual nanoindentation inside the grain

To assess the physical mechanisms responsible for plastic deformation in CrCoNi MEA, atomistic simulations were used because they are sensitive and can detect the nucleation of defects and their subsequent multiplication, motion, and interactions with other defects. Such events appear in nanoindentation experiments as pop-ins. However, they appear as force drops on the force-displacement curve from the nanoindentation using molecular dynamic simulation.

To the above end, a virtual nanoindenter was continuously introduced into the sample while recording both forces against displacement and sample snapshots at an interval of 2000 steps. A nanoindent was initially positioned at 9 nm from the TB. Its force-displacement curve shows the first force drop at a depth of 0.303 nm (see ellipsis m in Fig. 5.13a). Before the force drop, deformation occurred elastically following Hertz's Law (see Eq. 2.7). The snapshots in this region revealed that all the atoms below the nanoindent had an FCC crystal structure. At the end of this elastic region, atoms below the nanoindent deviated from the initial FCC and rearranged into a body-centered cubic (BCC) lattice structure. Similar results had been observed by Hua et al. [152] who observed changes of atoms from FCC structure to BCC structure at a depth of 0.42nm in CrCoNi MEA. At the end of the force drop, the snapshot (Fig. 5.13b) revealed the formation of a single curved partial dislocation which ends at free surfaces formed below the nanoindenter with **b** = 1/6 [1-21] (green colored). It is worth noting that various modifiers in the open visualization software (OVITO) have been used to produce Fig. 5.13b and subsequent figures in this chapter. Select and delete modifiers were used to remove atoms

with FCC and unknown crystal structures. A defect mesh modifier was applied to the simulation cell for better visualization. CNA and DXA modifiers were used to extract dislocations. The force drop was also observed in (111) Al because of the nucleation of an initial defect beneath the tip [150]. Moreover, It was argued that nucleation of dislocations starts from a nano-cluster of BCC-like defects, which are transformed into an HCP structure and become the nucleus of the initial partial dislocations bounding a stacking fault [152]. Nanoscale elemental analysis has also revealed that the nanoscale BCC clusters are rich in Cr [152].

Subsequent significant force drops (see ellipses such as n and o in Fig. 5.13a) are associated with forming a structure of dislocations with minimum energy. For example, the force drop at the ellipsis in blue (see Fig. 5.13a) corresponds to the formation of 50 dislocations with 36 1/6<112> partial dislocations and 14 non-identified dislocations (Fig. 5.13c). Prior to the drop, *i.e.*, there were 33 dislocations at the maximum with 16 1/6 <112> partial dislocations and 17 non-identified dislocations. Thus, non-identified dislocations induce high energy into the system, and FCC dislocations' formation minimizes such energy. Hua et al. [152] also proposed that subsequent force drop on a force-displacement curve correspond to multiplication and reaction of dislocations, which produce networks of dislocations. Moreover, the final dislocations structure revealed that dislocations around the nanoindent are more or less symmetric (Fig. 5.13d). The distance from the nanoindentation axis and the farthest dislocation in the x-y plane is ~8 nm along X-axis and 5 nm along Y-axis, while the dislocation loop traveled as deep as 9.4 nm along the Z-axis.

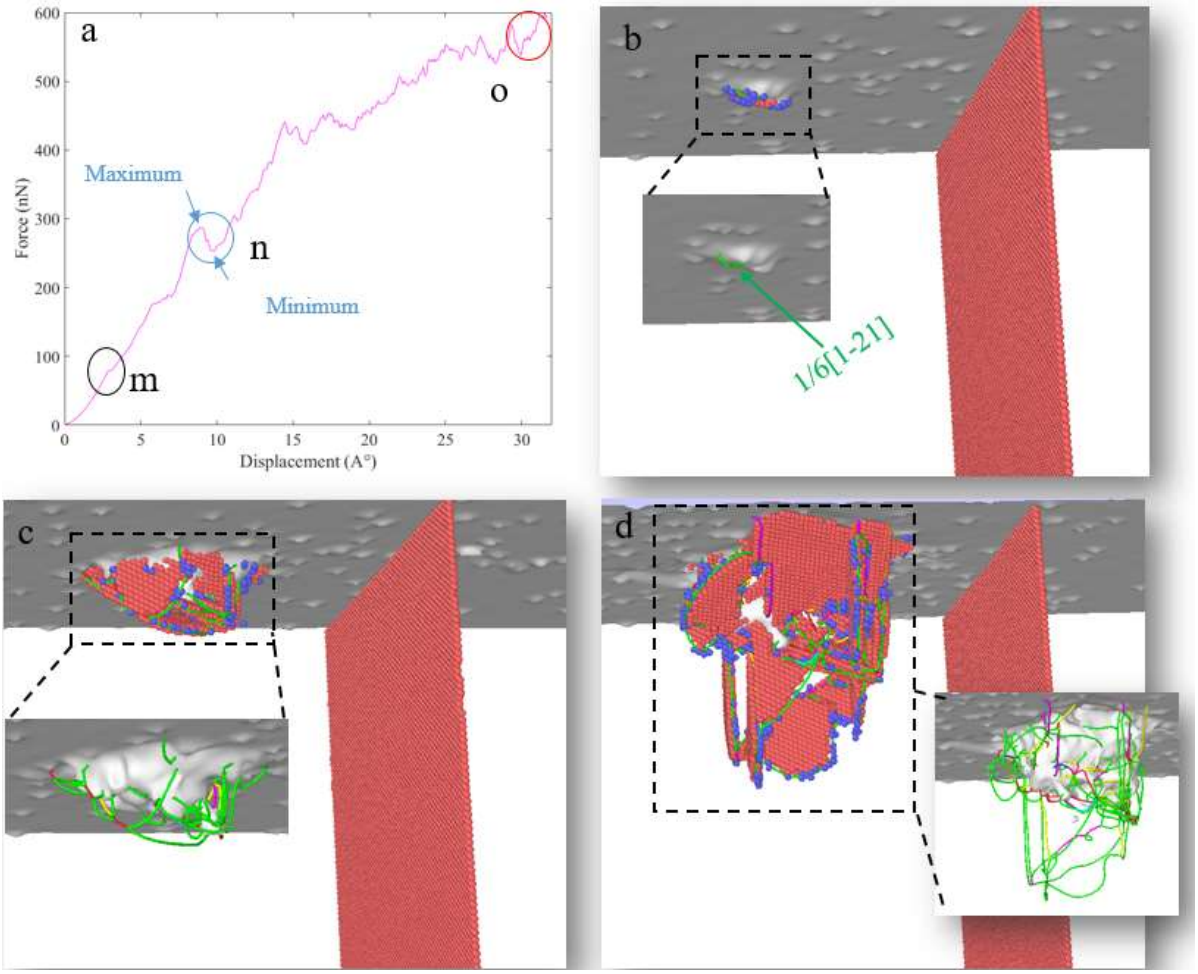

Fig. 5.13. (a) Force-displacement curve for a nanoindent at 9 nm from the TB, (b-d) snapshots for black, blue, and red ellipses m, n, and o, respectively. (bi), (ci), and (di) are structures of dislocations inside each enclosed broken rectangle.

5.3.4. Virtual Nanoindentation at 4.5 nm from the TB

Similar to the nanoindent at 9 nm, the nanoindentation at 4.5 nm from the TB starts with nucleating of 1/6<112> partial dislocations, depicted as a force drop at a depth of 2.82 Å (see ellipsis m in Fig. 5.14a). Continuous nanoindentation induced many non-identifiable dislocations, which increased the energy, and thus a second force drop occurred to reduce the system's energy (see ellipsis n on Fig. 5.14a). Unlike the curve in Fig. 5.13a with small force drops after the second force drop, a significant force drop occurred at a depth of 17.85 Å (see ellipsis o in Fig. 5.14a). Its corresponding snapshot revealed that it is due to the absorption of partial dislocations into the TB. The dislocations line was found in the TB plane (see magnified snapshot Figs. 5.14bi-ii). A further force drop occurred at a depth of 22.09 Å (see ellipsis p in Fig. 5.14a), corresponding to the partial dislocations' passage across the TB. Such an event is depicted in Fig. 5.14c and 5.14ci where a perfect dislocation (blue) crossed the boundary and

immediately dissociated into partial dislocations. Figure 5.14d shows traces of dislocations on the surfaces. The farthest dislocation on the side adjacent to the TB is the single dislocation that crossed the TB at a distance of ~4.5 nm. The farthest dislocation is at ~6 nm from the center to the opposite side of the nanoindent. These two observations imply that the TB blocks the expansion of the dislocation loops and the motion of dislocations because the expansion was higher for the side opposite to the TB.

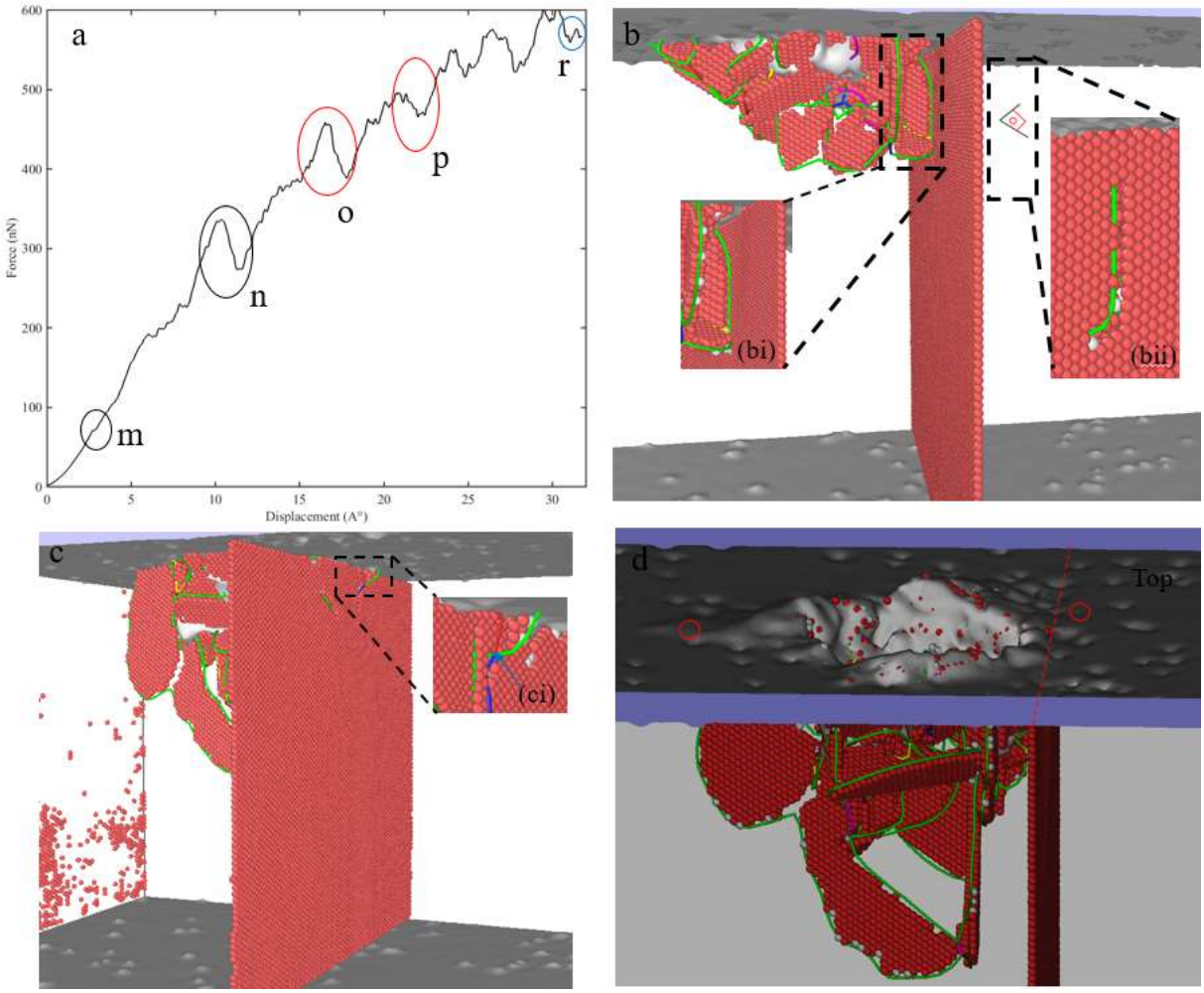

Fig. 5.14 (a) Force-displacement curve of the nanoindent at 4.5 nm from the TB. (b-d) Snapshots of simulation at force drop o, p, and r, respectively. (bi) and (bii) are magnified images of the dislocation in the TB. (ci) magnified image of crossed dislocation.

5.3.5. Virtual nanoindentation at 3 nm from the TB

Similar to the nanoindent at 9 nm and 4.5 nm from the TB, the initial force drop occurred at a slightly higher depth of 3.56 Å and corresponds to the nucleation of a curved partial dislocation with both ends intersecting the surface. Moreover, the second and third force drops (see ellipses

m and o in Fig. 5.15a) correspond to the formation of the low energy dislocation structures from the high-energy non-identifiable dislocation structures.

A significant force drop was observed at a depth of 13.62 Å (ellipsis p in Fig. 5.15a). Thus, it happened a little earlier than the nanoindenter at 4.5 nm from the TB, which occurred at a depth of 17.85Å. The snapshot at this drop corresponds to the absorption of 1/6<112> straight partial and 1/2 <011> type perfect dislocations (green and blue colored) into the TB (see Fig. 5.15b).

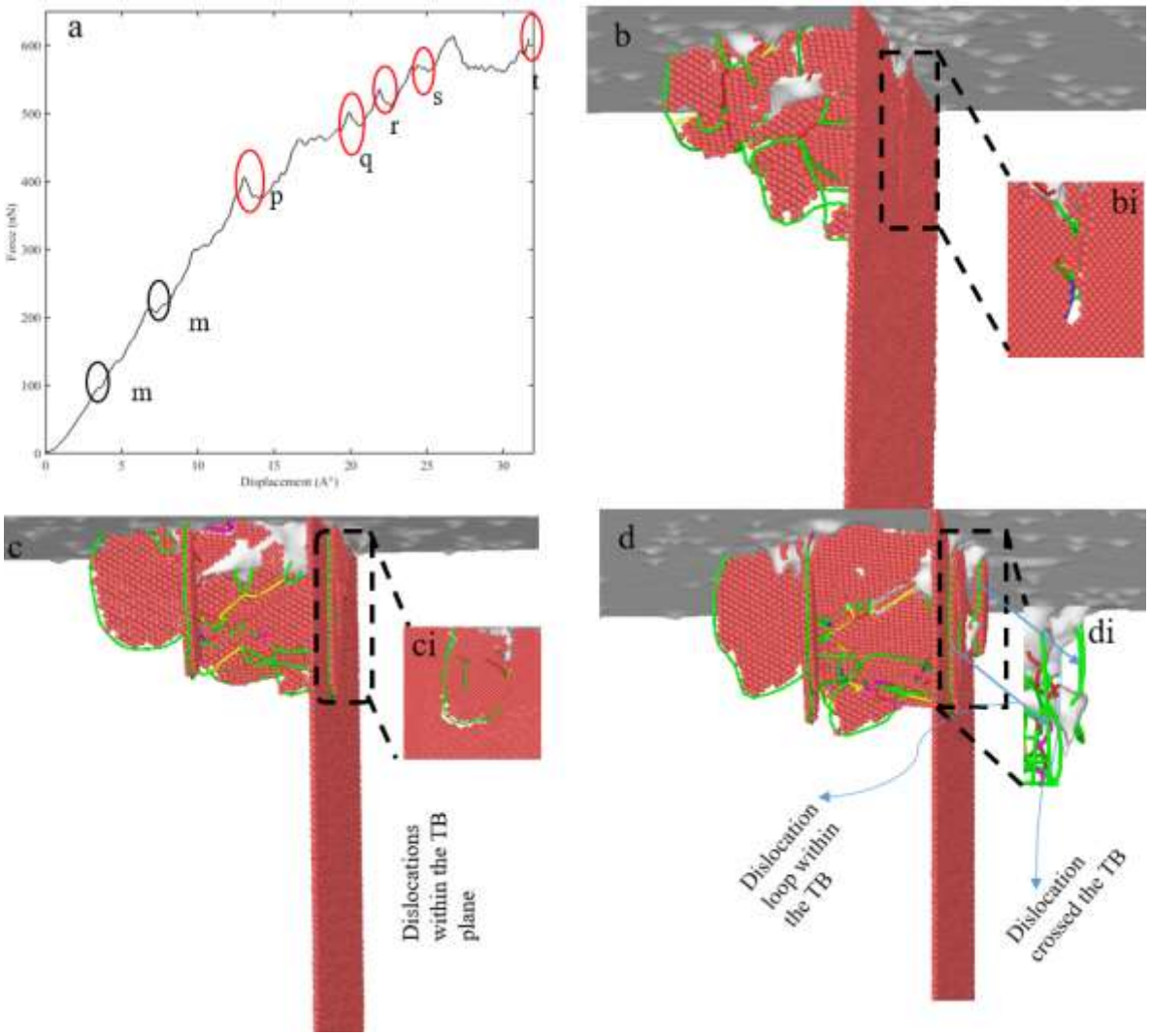

Fig. 5.15. (d) Force-displacement curve of the nanoindent at 3 nm from the TB. (b-d) Snapshots of simulation at force drop p, q, and r, respectively. (bi-ci) magnified images of (b-c) where dislocation is absorbed in the TB as viewed from the right. (di) is the magnified dislocation structure showing the TB dislocation loop and emitted dislocations.

A magnified image of the dislocations in the TB observed from the right is shown in Fig. 5.15bi. Continuous nanoindentation generated a dislocation loop within the TB (see Fig. 5.15c). It is clearly shown by a magnified image as viewed from the right-hand side of the TB (Fig. 5.15ci).

Such an event is depicted as a force drop at a depth of 17.10 Å (see ellipsis q in Fig. 5.15a). The passage of two partial dislocations to the other side of the TB is marked by a force drop at a depth of 20.57 Å (see ellipsis r in Fig. 5.15a). The two partial dislocations are along a plane parallel to the TB, *i.e.*, (1-11) plane, as shown by a snapshot in Fig. 5.15d. Additional two partial dislocations crossed the TB and resulted in the force drop at a depth of 22.7 Å (see ellipsis in s in Fig.5.15a). Further force drops correspond to the passage of additional dislocations across the TB.

5.3.6. Virtual nanoindent at 1 nm from the TB

Similar to the other nanoindents, the onset of plasticity occurred by nucleating of partial dislocation at a depth of 3.27A° inside the grain with one end in the TB. Further dislocations nucleated from the TB and multiple force drops are due to the formation of equilibrium dislocation structures, as is the case with the nanoindent in the grain.

5.4. Discussion

The experimental studies revealed that TBs examined respond differently to the incoming lattice dislocations. Nanoindents at the same position in different grains adjacent to the TB have different mechanical responses. The reason for these differences is due to the inclination of the TB plane to the surface. Thus, its inclination as suggested by the schematic in Fig. 5.7b plays a critical role in the study of dislocation-TB interactions. If a nanoindent is placed at the same surface distances from the TB plane, the dislocation-TB interactions will be different. Indirect transmission of dislocations has been observed in Fig. 5.5-6. and the incoming and outgoing slip systems were determined using geometric criteria. Similarly, geometric and shear stress criteria have been used by Shen et al. [12] to precisely predict the slip stem emitted on the other side of the TB. Chassagne et al.[67] also observed pile up and crossing of dislocation across a TB. However, he argued that it is indirect transmission since direct transmission does not require pile-up [67].

The MD simulations revealed that the position of the nanoindent from TBs has a significant impact on the deformation mechanism in CrCoNi. In all the four nanoindents analyzed, the incipient plasticity was due to the nucleation of a single partial dislocation characterized by a force drop on the force-displacement curve. The force drop is similar to pop-in on the P-h curve from the experimental nanoindentation test. Both nanoindentations inside and near the TB exhibited multiple force drops. The force drops have been associated with the formation of

equilibrium FCC dislocations for nanoindentation inside the grain. In contrast, they were associated with miscellaneous interactions of dislocations in the nanoindentation near the TB.

The interactions of dislocation and the TB occurred earlier for a nanoindent at 3 nm than for the nanoindent at 4.5 nm. This is because the expansion of dislocation loops reaches the TB earlier for a nanoindent closer than for the nanoindent far away from the TB. In the early deformation stages, these straight dislocations and dislocation loops form below the nanoindent and expand in all directions. In a TB, dislocations are absorbed, which relaxes the system, and a force drop occurs. The absorption of NIDs has also been observed experimentally as shown by ECC micrographs (Fig.5.6-8). Continuous nanoindentation increases the stress field in the TB, which emits dislocation on the other side. The emitted dislocations are not on the random plane, they are rather on FCC slip planes e.g., emission of partial dislocations on {111}plane parallel to the TB. Similarly, the slip traces induced dislocations are on the same plane as the TB (Fig. 5.7). The same results were observed when lattice dislocations interacted with twin boundaries in FCC simple metals such as Al, Au, Cu, and Ni [67].

5.5. Conclusions of the chapter

The experiments and atomistic simulation investigated plastic deformation mechanisms near a TB and a step in a CrCoNi MEA using ECC and nanoindentation as well as MD, respectively. The results of this study can be summarized as follows:

- Experimental investigation revealed that lattice dislocations pile up against the TB along specific slip traces. They are absorbed by the TB and pass across the TB depending on the position of the nanoindent relative to the TB and the orientation of the TB plane.
- The incipient plasticity is assumed to be caused by nucleation of dislocations since the ECC micrographs were taken during postmortem characterization. MD confirmed that, indeed, it occurs by nucleation of a single dislocation, which appears as a force drop on a force-displacement curve.
- TB initially accommodates plasticity by blocking dislocations, which are later absorbed within it and finally emitted on the other side. All these events generate force drops on the force-displacement curve.

This study proved that the initial force drop on the force-displacement curve from the atomistic simulations (or initial pop-in on the P-h curve during the experimental nanoindentation test) occurs by nucleation of a dislocation in a defect-free zone. Subsequent force drops correspond

to the formation of the stable configuration of dislocations or interaction of dislocations with the TB in this particular case. This differs slightly from the stipulated explanation based on the experimental nanoindentation test that multiple pop-ins were due to multiplication and motion of dislocations. Thus, this study shed light on the onset of plasticity of the CrCoNi MEA and the interaction of nanoindentation-induced dislocations with the TB. However, it opens doors to further studies on the origins and mechanisms of the multiple pop-ins observed during nanoindentation as well as micromechanical response associated with absorption of dislocations during experimental nanoindentation test in metallic materials.

General conclusions and perspectives

General conclusions

This project has examined the intragranular and intergranular mechanisms of plastic deformation in single crystal and polycrystalline CrCoNi MEA. The experimental studies employed instrumented nanoindentation to induce localized plastic deformation near specific microstructural features and SEM-based techniques, especially A-ECCI, to characterize microstructural evolution. Numerical elasticity calculation and atomistic simulations were used to dynamically shed light on some of the complexity of interactions between microstructural features during the experiments and allow access to features that cannot be obtained from the experiments.

The mechanism of the incipient plasticity of CrCoNi alloy was found to be homogeneous nucleation of dislocations in a defect-free zone as proven by experiment, elasticity calculation, and atomistic simulations. The maximum shear stress at incipient plasticity occurred when the maximum shear stress beneath the nanoindenter approaches the theoretical shear stress. However, the maximum shear stress decreased when nanoindentation was placed in the region near a dislocation, a dipole, or a pair of dislocations. The decrease was proportional to the distance from the dislocation configuration to the nanoindentation axis. Such a decrease implies that plastic deformation occurs by heterogeneous nucleation of dislocations in the presence of defects.

The nucleated pile-up of dislocations along specific planes can interact with grain boundaries when the residual indentation imprints are closer to the grain boundary. For the case of a low angle grain boundary with misorientation of 0.24° and dislocation spacing of 60 nm, plasticity is accommodated by blocking the motion of incoming lattice dislocations, the collective motion of its dislocations, and by allowing the activation of a dislocation source on the other side of the boundary. For the case of a twin boundary, different mechanisms occurred and were associated with different orientations of the twin boundary plane. Using a combination of EBSD map, ECC micrograph, and STABIX, slip transmission criteria (N-factor and m' parameter) were calculated and used to predict possible activated slip on the other side of the TB. Moreover, some lattice dislocations were absorbed in the trace of the TB. The atomistic simulations revealed micromechanical responses associated with different interactions of

dislocations with twin boundaries. Such responses are force drops that appear on the force-displacement curve from the virtual nanoindentation test.

Following the results of this project, an attempt is made here to provide answers to the questions asked at the end of chapter 1:

- **How do dislocation-based mechanisms control the incipient plasticity of CrCoNi MEA?**

The initial pop-in on the P-h curve during the nanoindentation test was associated with the nucleation of dislocations. This was clearly observed using atomistic simulation where the force drop was observed after the homogeneous nucleation of a 1/6 <112> partial dislocation in a dislocation-free zone. In addition, both experiment and elasticity calculation revealed that the configurations of pre-existing dislocations and their positions with respect to the nanoindentation axis decrease the maximum shear stress, *i.e.*, plasticity occurred by heterogeneous nucleation of dislocations.

- **How do incoming lattice dislocations interact with constituent intrinsic LAGB dislocations in a single crystalline CrCoNi MEA?**

EBSD map of the single crystalline CrCoNi MEA revealed that the alloy is made of dendrites separated by low-angle grain boundaries. The low angle boundary of interest was made of dislocations with a spacing of 60 nm. The incoming lattice dislocations were blocked and absorbed in the LAGB. The LAGB also accommodated a pile-up of the incoming lattice dislocations by collective motion of its dislocations. Moreover, lattice dislocations have been transmitted across the LAGB, as evidenced by new dislocations observed following nanoindentation on the other side of the LAGB.

- **How do incoming lattice dislocations interact at both TB and step in polycrystalline CrCoNi MEA?**

The polycrystalline CrCoNi medium entropy alloy exhibit almost 50% of annealing twins among its boundaries, *i.e.*, twin boundaries play a critical role in grain boundary strengthening of this alloy. Nanoindentation-induced dislocations pile-up against a twin boundary until the stress at the end of the pile-up induces the transfer of slip on the other side. Slip transfer criteria were used to predict the activated slip system on the other side of twin boundaries. Thus, twin boundaries initially block and absorb the incoming lattice dislocations. Furthermore, they accommodate plasticity by transfer of slip on the other side of the twin boundaries.

Perspectives

In this thesis, the influence of the dislocations on the P_p and τ_{max} employed the simplest cases of single edge dislocation, dipole, and dislocation pair. Thus, further calculations that look at complex cases such as walls of dislocations and arrays of dislocations are needed to fully comprehend the causes and mechanisms of the initial pop-in.

TBs have been found to influence the mechanical properties of the CrCoNi MEA through the interaction with lattice dislocations. Further studies should look at the interactions with other special high-angle grain boundaries.

Conclusions générales et perspectives

General Conclusions

Cette thèse a examiné les mécanismes intragranulaires et granulaires de la déformation plastique dans deux échantillons de CrCoNi monocristallin avec des dendrites faiblement désorientées et polycristallin. Pour l'étude expérimentale, la nanoindentation instrumentée a été utilisée pour induire une déformation plastique localisée, les caractéristiques microstructurales spécifiques et des techniques basées sur le MEB, en particulier A-ECCI, ont été utilisée pour caractériser l'évolution microstructurale. Le calcul numérique de l'élasticité et les simulations atomistiques ont été utilisés pour éclairer de manière dynamique une partie de la complexité des interactions entre les caractéristiques microstructuralles pendant les expériences mais également permettre l'accès à des caractéristiques qui ne sont pas réalisables par les expériences.

Le mécanisme de la plasticité naissante s'est avéré être une nucléation homogène de dislocations dans une zone sans défaut, comme le prouvent l'expérience, le calcul d'élasticité et les simulations atomistiques. La contrainte de cisaillement maximale au niveau de cette plasticité naissante est proche de la contrainte de cisaillement théorique. Cependant, la contrainte de cisaillement maximale a diminué lorsque la nanoindentation était placée dans la région proche d'une dislocation, d'un dipôle ou d'une paire de dislocation. Cette diminution était proportionnelle à la distance entre le défaut et l'axe d'nanoindentation. Cette diminution implique que la déformation plastique se produit par nucléation hétérogène des dislocations en présence de défauts.

Les dislocations nucléées s'empilent le long de plans spécifiques et peuvent interagir avec les joints de grains lorsque les empreintes résiduelles sont plus proches d'eux. Dans le cas d'un joint de grain à angle faible désorientation (~0.24°) et un espacement des dislocations de 60 nm, la plasticité est prise en compte en bloquant le mouvement des dislocations de réseau entrantes, par le mouvement collectif de ses dislocations, et en permettant l'activation de la source de dislocation de l'autre côté du sous-joint de grain. Dans le cas de la macle, différents mécanismes se sont produits et ont été associés aux différentes orientations du plan de la macle. En utilisant une combinaison de la carte EBSD, de la micrographie d'ECCI et de STABIX, les critères de transmission du glissement (« N-factor et m' parameter ») ont été utilisés pour prédire un

éventuel glissement activé de l'autre côté du joint de macle. De plus, certaines dislocations du réseau ont été absorbées dans la trace par le joint. Les simulations atomistiques ont révélé les réponses micromécaniques associées aux différentes interactions des dislocations avec les joints de macle. Ces réponses sont des petits pics de force qui apparaissent sur la courbe force-déplacement de l'essai de nanoindentation virtuelle.

Perspectives

Dans cette thèse, l'influence des dislocations sur la contrainte de cisaillement maximale a été etudié pour le cas d'un dislocation, d'un dipôle et de paire de dislocations. Ainsi, d'autres calculs portant sur des cas complexes tels que des murs de dislocations et des réseaux de dislocations sont nécessaires pour comprendre pleinement les causes et les mécanismes du « pop-in ».

On a constaté que les macles influaient sur les propriétés mécaniques de l'alliage de CrCoNi en interagissant avec les dislocations. D'autres études devraient porter sur les interactions de entre dislocation et les autres joints de grain.

.

References

[1] R. Z. Valiev, V. Y. Gertsman, and O. A. Kaibyshev, “Grain boundary structure and properties under external influences,” *Phys. Status Solidi*, vol. 97, no. 1, pp. 11–56, 1986.

[2] Y. Mishin, M. Asta, and J. Li, “Atomistic modeling of interfaces and their impact on microstructure and properties,” *Acta Mater.*, vol. 58, no. 4, pp. 1117–1151, 2010.

[3] J. P. Hirth, “On dislocation interactions in the fcc lattice,” *J. Appl. Phys.*, vol. 32, no. 4, pp. 700–706, 1961.

[4] K. D. Ralston, D. Fabijanic, and N. Birbilis, “Effect of grain size on corrosion of high purity aluminium,” *Electrochim. Acta*, vol. 56, no. 4, pp. 1729–1736, 2011.

[5] L. Rémy, “The interaction between lip and twinning systems and the influence of twinning on the mechanical behavior of fcc metals and alloys,” *Metall. Trans. A, Phys. Metall. Mater. Sci.*, vol. 12 A, no. 3, pp. 387–408, 1981.

[6] J. P. Couzinié, B. Décamps, and L. Priester, “Interaction of dissociated lattice dislocations with a $\sum = 3$ grain boundary in copper,” *Int. J. Plast.*, vol. 21, no. 4, pp. 759–775, 2005.

[7] B. Chalmers and P. R. S. L. A, “Some crystal-boundary phenomena in metals,” *Proc. R. Soc. London. Ser. A. Math. Phys. Sci.*, vol. 196, no. 1044, pp. 64–73, 1949.

[8] N. Hansen, “Hall-petch relation and boundary strengthening,” *Scr. Mater.*, vol. 51, no. 8

SPEC. ISS., pp. 801–806, 2004.

[9] W. A. Soer and J. T. M. De Hosson, “Detection of grain-boundary resistance to slip transfer using nanoindentation,” *Mater. Lett.*, vol. 59, no. 24–25, pp. 3192–3195, 2005.

[10] R. W. Armstrong, “The influence of polycrystal grain size on several mechanical properties of materials,” *Metall. Mater. Trans.*, vol. 1, no. 5, pp. 1169–1176, 1970.

[11] A. A. Johnson, “The effect of grain size on the tensile properties of high-purity molybdenum at room temperature,” *Philos. Mag.*, vol. 4, no. 38, pp. 194–199, 1959.

[12] Z. Shen, R. H. Wagoner, and W. A. T. Clark, “Dislocation and grain boundary interactions in metals,” *Acta Metall.*, vol. 36, no. 12, pp. 3231–3242, 1988.

[13] R. C. Pond and D. A. Smith, “On the absorption of dislocations by grain boundaries,” *Philos. Mag.*, vol. 36, no. 2, pp. 353–366, 1977.

[14] D. J. Dingley and R. C. Pond, “On the interaction of crystal dislocations with grain boundaries,” *Acta Metall.*, vol. 27, no. 4, pp. 667–682, 1979.

[15] S. J. Vachhani, R. D. Doherty, and S. R. Kalidindi, “Studies of grain boundary regions in deformed polycrystalline aluminum using spherical nanoindentation,” *Int. J. Plast.*, vol. 81, pp. 87–101, 2016.

[16] V. Randle, “Mechanism of twinning-induced grain boundary engineering in low stacking-fault energy materials,” *Acta Mater.*, vol. 47, no. 15, pp. 4187–4196, 1999.

[17] P. Lin, G. Palumbo, U. Erb, and K. T. Aust, “Influence of grain boundary character distribution on sensitization and intergranular corrosion of alloy 600,” *Scr. Metall. Mater.*, vol. 33, no. 9, pp. 1387–1392, 1995.

[18] N. L. Okamoto, K. Yuge, K. Tanaka, H. Inui, and E. P. George, “Atomic displacement in the CrMnFeCoNi high-entropy alloy - A scaling factor to predict solid solution strengthening,” *AIP Adv.*, vol. 6, no. 12, 2016.

[19] G. Laplanche, A. Kostka, C. Reinhart, J. Hunfeld, G. Eggeler, and E. P. George, “Reasons for the superior mechanical properties of medium-entropy CrCoNi compared to high-entropy CrMnFeCoNi,” *Acta Mater.*, vol. 128, pp. 292–303, 2017.

[20] G. Laplanche, A. Kostka, O. M. Horst, G. Eggeler, and E. P. George, “Microstructure evolution and critical stress for twinning in the CrMnFeCoNi high-entropy alloy,” *Acta Mater.*, vol. 118, pp. 152–163, 2016.

[21] M. Schneider *et al.*, “Analysis of strengthening due to grain boundaries and annealing twin boundaries in the CrCoNi medium-entropy alloy,” *Int. J. Plast.*, vol. 124, no. August 2019, pp. 155–169, 2019.

[22] D. F. Bahr and D. J. Morris, “Nanoindentation: Localized Probes of Mechanical Behaviour of Materials,” in *Handbook of Experimental Solid Mechanics*, S. W.S., Ed. Springer US, 2008, pp. 389–408.

[23] H. Mansour, J. Guyon, M. A. Crimp, N. Gey, B. Beausir, and N. Maloufi, “Accurate electron channeling contrast analysis of dislocations in fine grained bulk materials,” *Scr. Mater.*, vol. 84–85, pp. 11–14, 2014.

[24] A. Guitton, H. Kriaa, E. Bouzy, J. Guyon, and N. Maloufi, “A dislocation-scale characterization of the evolution of deformation microstructures around nanoindentation imprints in a TiAl alloy,” *Materials (Basel).*, vol. 11, no. 2, 2018.

[25] H. Kriaa, A. Guitton, and N. Maloufi, “Modeling dislocation contrasts obtained by accurate-electron channeling contrast imaging for characterizing deformation mechanisms in bulk materials,” *Materials (Basel).*, vol. 12, no. 1587, 2019.

[26] H. Mansour, M. A. Crimp, N. Gey, and N. Maloufi, “Accurate electron channeling contrast analysis of a low angle sub-grain boundary,” *Scr. Mater.*, vol. 109, pp. 76–79, 2015.

[27] H. Kriaa, A. Guitton, and N. Maloufi, “Fundamental and experimental aspects of diffraction for characterizing dislocations by electron channeling contrast imaging in scanning electron microscope,” *Sci. Rep.*, vol. 7, no. 1, pp. 1–8, 2017.

[28] J.P. Hirth; J. Lothe, *Theory of dislocations*, Second edi. John Wiley & Sons, Inc, Hoboken, USA, 1982.

[29] J. Hull, D.; Bacon, “Introduction to Dislocations.” Butterworth-Heinman, Oxford, UK, 2001.

[30] F. Seitz, “On the generation of vacancies by moving dislocations,” *Adv. Phys.*, vol. 1, no. 1, pp. 43–90, 1952.

[31] R. C. Bullough, R; New man, “The Interaction of vacancies with dislocations,” *Philos. Mag. A J. Theor. Exp. Appl. Phys.*, vol. 7, no. 75, pp. 529–531, 1962.

[32] Y. K. Dou, H. Cao, X. F. He, J. Gao, J. li Cao, and W. Yang, “Interaction mechanism of an edge dislocation with a void in Fe–Ni–Cr concentrated solid-solution alloy,” *J. Alloys Compd.*, vol. 857, no. xxxx, p. 157556, 2021.

[33] H. Wei and Y. Wei, “Interaction between a screw dislocation and stacking faults in FCC metals,” *Mater. Sci. Eng. A*, vol. 541, pp. 38–44, 2012.

[34] R. Su *et al.*, “The influence of stacking faults on mechanical behavior of advanced materials,” *Mater. Sci. Eng. A*, vol. 803, no. December 2020, p. 140696, 2021.

[35] H. Pan, Y. He, and X. Zhang, “Interactions between dislocations and boundaries during deformation,” *Materials (Basel).*, vol. 14, no. 4, pp. 1–48, 2021.

[36] R. B. Nicholson, G. Thomas, and J. Nutting, “The interaction of dislocations and precipitates,” *Acta Metall.*, vol. 8, no. 3, pp. 172–176, 1960.

[37] A. Takahashi and N. M. Ghoniem, “A computational method for dislocation-precipitate interaction,” *J. Mech. Phys. Solids*, vol. 56, no. 4, pp. 1534–1553, 2008.

[38] C. Y. Wang, C. M. Cepeda-Jiménez, and M. T. Pérez-Prado, “Dislocation-particle interactions in magnesium alloys,” *Acta Mater.*, vol. 194, pp. 190–206, 2020.

[39] M. Kato, “Hallpetch relationship and dislocation model for deformation of ultrafine-grained and nanocrystalline metals,” *Mater. Trans.*, vol. 55, no. 1, pp. 19–24, 2014.

[40] S. Yoshida, T. Bhattacharjee, Y. Bai, and N. Tsuji, “Friction stress and Hall-Petch relationship in CoCrNi equi-atomic medium entropy alloy processed by severe plastic

deformation and subsequent annealing," *Scr. Mater.*, vol. 134, pp. 33–36, 2017.

[41] B. R. Kuhr and K. E. Aifantis, "Interpreting the inverse Hall-Petch relationship and capturing segregation hardening by measuring the grain boundary yield stress through MD indentation," *Mater. Sci. Eng. A*, vol. 745, no. July 2018, pp. 107–114, 2019.

[42] W. Lu, X. Luo, Y. Yang, and B. Huang, "Hall-petch relationship and heterogeneous strength of CrCoNi medium-entropy alloy," *Mater. Chem. Phys.*, vol. 251, no. April, p. 123073, 2020.

[43] W. D. Callister and J. Wiley, *Materials Science and Engineering: an Introduction*. Newyork, USA: John Wiley & sons, Inc, 2007.

[44] D. Mercier, C. Zambaldi, and T. R. Bieler, "A Matlab toolbox to analyze slip transfer through grain boundaries," *IOP Conf. Ser. Mater. Sci. Eng.*, vol. 82, no. 1, pp. 1–4, 2015.

[45] M. A. ;Krisha. K. C. Meyers, "Imperfections: Point and line defects," in *Mechanical Behaviour of materials*, Cambridge, UK: Cambridge University Press, 2009.

[46] Z. Li, S. Zhao, R. O. Ritchie, and M. A. Meyers, "Mechanical properties of high-entropy alloys with emphasis on face-centered cubic alloys," *Prog. Mater. Sci.*, vol. 102, pp. 296–345, 2019.

[47] A. W. Ruff, "Measurement of stacking fault energy from dislocation interactions," *Metall. Trans.*, vol. 1, no. 9, pp. 2391–2413, 1970.

[48] V. Randle, "Grain boundary engineering: An overview after 25 years," *Mater. Sci.*

Technol., vol. 26, no. 3, pp. 253–261, 2010.

[49] V. Randle and G. Owen, "Mechanisms of grain boundary engineering," *Acta Mater.*, vol. 54, no. 7, pp. 1777–1783, 2006.

[50] G. S. Rohrer, "Grain boundary energy anisotropy: A review," *J. Mater. Sci.*, vol. 46, no. 18, pp. 5881–5895, 2011.

[51] V. Randle, "An investigation of grain-boundary plane crystallography in polycrystalline nickel," *J. Mater. Sci.*, vol. 30, pp. 3983–3988, 1995.

[52] T. B. Britton *et al.*, "Tutorial: Crystal orientations and EBSD - Or which way is up?," *Mater. Charact.*, vol. 117, pp. 113–126, 2016.

[53] V. Randle, "A methodology for grain boundary plane assessment by single-section trace analysis," vol. 44, pp. 2789–2794, 2001.

[54] L. Priester, *Grain boundaries and Crystalline Plasticity*. John Wiley & Sons, Inc, Hoboken, USA, 2011.

[55] T. W. Read and W. Shockley, "Dislocation Models of Crystal Grain Boundaries," *Phys. Rev.*, vol. 78, no. 3, p. 275, 1950.

[56] M. Ben Saada, N. Gey, B. Beausir, X. Iltis, H. Mansour, and N. Maloufi, "Sub-boundaries induced by dislocational creep in uranium dioxide analyzed by advanced diffraction and channeling electron microscopy," *Mater. Charact.*, vol. 133, no. September, pp. 112–121, 2017.

[57] S. Ratanaphan, T. Boonkird, R. Sarochawikasit, H. Beladi, K. Barmak, and G. S. Rohrer, “Atomistic simulations of grain boundary energies in tungsten,” *Mater. Lett.*, vol. 186, no. September 2016, pp. 116–118, 2017.

[58] G. Bollmann, *Crystal Defects and crystalline interfaces*. Springer-Verlag, Berlin,Heidelberg, Germany, 1970.

[59] L. C. . Lim, “Slip-twin interactions in nickel at 537K at large strains,” *Scr. Metall.*, vol. 18, pp. 1139–1142, 1984.

[60] H. Miura, M. Kato, and T. Mori, “Temperature dependence of the energy of Cu [110] symmetrical tilt grain boundaries,” *J. Mater. Sci. Lett.*, vol. 13, no. 1, pp. 46–48, 1994.

[61] M. A. Tschopp, S. P. Coleman, and D. L. McDowell, “Symmetric and asymmetric tilt grain boundary structure and energy in Cu and Al (and transferability to other fcc metals),” *Integr. Mater. Manuf. Innov.*, vol. 4, no. 1, pp. 176–189, 2015.

[62] P. B. . H. R. W. Whelan, M. J.; Hirsch, “Dislocations and stacking faults in stainless steel,” *Proc. R. Soc. London, Ser. A*, vol. 165, p. 372, 1957.

[63] S. Chandra, M. K. Samal, V. M. Chavan, and R. J. Patel, “Atomistic simulations of interaction of edge dislocation with twist grain boundaries in Al-effect of temperature and boundary misorientation,” *Mater. Sci. Eng. A*, vol. 646, pp. 25–32, 2015.

[64] W. A. . Shen Z.; Wagoner R.H.; Clark, “Dislocation pile-up and Grain boundary interaction in 304 stainless steel,” *Scr. Metall.*, vol. 20, no. c, pp. 921–926, 1986.

[65] S. Kondo, T. Mitsuma, N. Shibata, and Y. Ikuhara, "Direct observation of individual dislocation interaction processes with grain boundaries," *Sci. Adv.*, vol. 2, no. 11, pp. 1–8, 2016.

[66] T. C. Lee, I. M. Robertson, and H. K. Birnbaum, "TEM in situ deformation study of the interaction of lattice dislocations with grain boundaries in metals," vol. 62, no. 1, pp. 131–153, 1990.

[67] M. Chassagne, M. Legros, and D. Rodney, "Atomic-scale simulation of screw dislocation/coherent twin boundary interaction in Al, Au, Cu and Ni," *Acta Mater.*, vol. 59, no. 4, pp. 1456–1463, 2011.

[68] E. Bayerschen, A. T. McBride, B. D. Reddy, and T. Böhlke, "Review on slip transmission criteria in experiments and crystal plasticity models," *J. Mater. Sci.*, vol. 51, no. 5, pp. 2243–2258, 2016.

[69] B. Livingston J.D.; Chalmers, "Slip in bicrystal," *Acta Metall.*, vol. 5, pp. 322–327, 1957.

[70] J. Kacher and I. M. Robertson, "Quasi-four-dimensional analysis of dislocation interactions with grain boundaries in 304 stainless steel," *Acta Mater.*, vol. 60, no. 19, pp. 6657–6672, 2012.

[71] J. Luster and M. A. Morris, "Compatibility of Deformation in Two-Phase Ti-AI Alloys : Dependence on Microstructure and Orientation Relationships," *Metall. Trans. A*, vol. 26, no. July, pp. 1745–1756, 1995.

[72] T. R. Bieler, R. Alizadeh, M. Peña-Ortega, and J. Llorca, "An analysis of (the lack of) slip transfer between near-cube oriented grains in pure Al," *Int. J. Plast.*, vol. 118, no.

February, pp. 269–290, 2019.

[73] T. C. Lee, I. M. Robertson, and H. K. Birnbaum, “Interaction of dislocations with grain boundaries in Ni3Al,” *Acta Metall.*, vol. 40, no. 10, 1992.

[74] D. W. Adams, D. T. Fullwood, R. H. Wagoner, and E. R. Homer, “Atomistic survey of grain boundary-dislocation interactions in FCC nickel,” *Comput. Mater. Sci.*, vol. 164, no. December 2018, pp. 171–185, 2019.

[75] B. Gludovatz *et al.*, “Exceptional damage-tolerance of a medium-entropy alloy CrCoNi at cryogenic temperatures,” *Nat. Commun.*, vol. 7, pp. 1–8, 2016.

[76] P. Sathiyamoorthi, J. Moon, J. W. Bae, P. Asghari-Rad, and H. S. Kim, “Superior cryogenic tensile properties of ultrafine-grained CoCrNi medium-entropy alloy produced by high-pressure torsion and annealing,” *Scr. Mater.*, vol. 163, pp. 152–156, 2019.

[77] J. W. Yeh *et al.*, “Nanostructured high-entropy alloys with multiple principal elements: Novel alloy design concepts and outcomes,” *Adv. Eng. Mater.*, vol. 6, no. 5, pp. 299-303+274, 2004.

[78] J. W. Yeh, Y. L. Chen, S. J. Lin, and S. K. Chen, “High-entropy alloys - A new era of exploitation,” *Mater. Sci. Forum*, vol. 560, pp. 1–9, 2007.

[79] S. Ranganathan, “Alloyed pleasures: Multimetallic cocktails,” *Curr. Sci.*, vol. 85, no. 10, pp. 1404–1406, 2003.

[80] B. Cantor, “Multicomponent and high entropy alloys,” *Entropy*, vol. 16, no. 9, pp. 4749–4768, 2014.

[81] S. Gorsse, J. P. Couzinié, and D. B. Miracle, “From high-entropy alloys to complex concentrated alloys,” *Comptes Rendus Phys.*, vol. 19, no. 8, pp. 721–736, 2018.

[82] D. B. Miracle and O. N. Senkov, “A critical review of high entropy alloys and related concepts,” *Acta Mater.*, vol. 122, pp. 448–511, 2017.

[83] G. Laplanche *et al.*, “Elastic moduli and thermal expansion coefficients of medium-entropy subsystems of the CrMnFeCoNi high-entropy alloy,” *J. Alloys Compd.*, vol. 746, pp. 244–255, 2018.

[84] H. W. Deng *et al.*, “Tailoring mechanical properties of a CoCrNi medium-entropy alloy by controlling nanotwin-HCP lamellae and annealing twins,” *Mater. Sci. Eng. A*, vol. 744, no. October 2018, pp. 241–246, 2019.

[85] B. Uzer *et al.*, “On the mechanical response and microstructure evolution of NiCoCr single crystalline medium entropy alloys,” *Mater. Res. Lett.*, vol. 6, no. 8, pp. 442–449, 2018.

[86] Z. Wu, H. Bei, F. Otto, G. M. Pharr, and E. P. George, “Recovery, recrystallization, grain growth and phase stability of a family of FCC-structured multi-component equiatomic solid solution alloys,” *Intermetallics*, vol. 46, pp. 131–140, 2014.

[87] S. Praveen, J. W. Bae, P. Asghari-Rad, J. M. Park, and H. S. Kim, “Annealing-induced hardening in high-pressure torsion processed CoCrNi medium entropy alloy,” *Mater. Sci. Eng. A*, vol. 734, pp. 338–340, 2018.

[88] J. Miao *et al.*, "The evolution of the deformation substructure in a Ni-Co-Cr equiatomic solid solution alloy," *Acta Mater.*, vol. 132, pp. 35–48, 2017.

[89] C. E. Slone, S. Chakraborty, J. Miao, E. P. George, M. J. Mills, and S. R. Niezgoda, "Influence of deformation induced nanoscale twinning and FCC-HCP transformation on hardening and texture development in medium-entropy CrCoNi alloy," *Acta Mater.*, vol. 158, pp. 38–52, 2018.

[90] M. Shih, J. Miao, M. Mills, and M. Ghazisaeidi, "Stacking fault energy in concentrated alloys," *Nat. Commun.*, vol. 12, no. 1, pp. 1–10, 2021.

[91] J. Miao *et al.*, "The evolution of the deformation substructure in a Ni-Co-Cr equiatomic solid solution alloy," *Acta Mater.*, vol. 132, pp. 35–48, 2017.

[92] G. Laplanche, O. Horst, F. Otto, G. Eggeler, and E. P. George, "Microstructural evolution of a CoCrFeMnNi high-entropy alloy after swaging and annealing," *J. Alloys Compd.*, vol. 647, pp. 548–557, 2015.

[93] M. S. Daw *et al.*, "Local lattice distortion in NiCoCr, FeCoNiCr and FeCoNiCrMn concentrated alloys investigated by synchrotron X-ray diffraction," *Acta Mater.*, vol. 186, no. 1, pp. 176–189, 2019.

[94] R. Zhang, S. Zhao, J. Ding, Y. Chong, T. Jia, and C. Ophus, "Short-range order and its impact on the CrCoNi medium-entropy alloy," *Nature*, vol. 581, no. May, 2020.

[95] A. Weidner, S. Martin, V. Klemm, U. Martin, and H. Biermann, "Stacking faults in high-alloyed metastable austenitic cast steel observed by electron channelling contrast imaging," *Scr. Mater.*, vol. 64, no. 6, pp. 513–516, 2011.

[96] J. Lu *et al.*, "Stacking fault energies in austenitic stainless steels," *Acta Mater.*, vol. 111, pp. 39–46, 2016.

[97] D. Canadinc, H. Sehitoglu, H. J. Maier, D. Niklasch, and Y. I. Chumlyakov, "Orientation evolution in Hadfield steel single crystals under combined slip and twinning," *Int. J. Solids Struct.*, vol. 44, no. 1, pp. 34–50, 2007.

[98] C. Niu, C. R. LaRosa, J. Miao, M. J. Mills, and M. Ghazisaeidi, "Magnetically-driven phase transformation strengthening in high entropy alloys," *Nat. Commun.*, vol. 9, no. 1, pp. 1–9, 2018.

[99] Y. X. Liang, X. F. Yang, K. S. Ming, S. H. Xiang, and Q. Liu, "In situ observation of transmission and reflection of dislocations at twin boundary in CoCrNi alloys," *Sci. China Technol. Sci.*, vol. 64, no. 2, pp. 407–413, 2021.

[100] L. Patriarca, A. Ojha, H. Sehitoglu, and Y. I. Chumlyakov, "Slip nucleation in single crystal FeNiCoCrMn high entropy alloy," *Scr. Mater.*, vol. 112, pp. 54–57, 2016.

[101] M. Kawamura, M. Asakura, N. L. Okamoto, K. Kishida, H. Inui, and E. P. George, "Plastic deformation of single crystals of the equiatomic Cr−Mn−Fe−Co−Ni high-entropy alloy in tension and compression from 10 K to 1273 K," *Acta Mater.*, vol. 203, 2021.

[102] M. A. Crimp, "Scanning electron microscopy imaging of dislocations in bulk materials, using electron channeling contrast," *Microsc. Res. Tech.*, vol. 69, no. 5, pp. 374–381, May 2006.

[103] H. Kriaa, A. Guitton, N. Maloufi, D. Mécanique, M. Lem, and U. M. R. Cnrs, "Electron

channelling contrast imaging : influence of diffraction conditions on the dislocation contrast Experimental observations and characterization of individual dislocation Single dislocations," pp. 1–2.

[104] J. Guyon, H. Mansour, N. Gey, M. A. Crimp, S. Chalal, and N. Maloufi, "Sub-micron resolution selected area electron channeling patterns," *Ultramicroscopy*, vol. 149, pp. 34–44, 2015.

[105] D. F. Bahr, D. E. Kramer, and W. W. Gerberich, "Non-linear deformation mechanisms during nanoindentation," *Acta Mater.*, vol. 46, no. 10, pp. 3605–3617, 1998.

[106] K. L. Johnson, *Contact Mechanics*. Cambridge University Press, 1985.

[107] G. Laplanche, M. Schneider, F. Scholz, J. Frenzel, G. Eggeler, and J. Schreuer, "Processing of a single-crystalline CrCoNi medium-entropy alloy and evolution of its thermal expansion and elastic stiffness coefficients with temperature," *Scr. Mater.*, vol. 177, pp. 44–48, 2020.

[108] U. Brückner, A. Epishin, and T. Link, "Local x-ray diffraction analysis of the structure of dendrites in single-crystal nickel-base superalloys," *Acta Mater.*, vol. 45, no. 12, pp. 5223–5231, 1997.

[109] A. B. Parsa *et al.*, "Advanced scale bridging microstructure analysis of single crystal Ni-base superalloys," *Adv. Eng. Mater.*, vol. 17, no. 2, pp. 216–230, 2015.

[110] P. Hallensleben *et al.*, "On the evolution of cast microstructures during processing of single crystal Ni-base superalloys using a Bridgman seed technique," *Mater. Des.*, 2017.

[111] L. Reimer, *Scanning Electron Microscopy: Physics of image formation and microanalysis*. Springer-Verlag, Berlin,Heidelberg, Germany, 1998.

[112] T. Oikawa, "Energy dispersive X-ray spectroscopy," *Japanese J. Tribol.*, vol. 51, no. 1, pp. 33–38, 2006.

[113] V. D. Hodoroaba, *Energy-dispersive X-ray spectroscopy (EDS)*, no. X. Elsevier Inc., 2019.

[114] D. J. Dingley and D. P. Field, "Electron backscatter diffraction and orientation imaging microscopy," *Mater. Sci. Technol.*, vol. 13, no. 1, pp. 69–78, 1997.

[115] V. Randle, *The Measurement of Grain Boundary Geometry*. Bristol: Institute of Physics Publishing, 1993.

[116] V. Randle, "Application of electron backscatter diffraction to grain boundaries," *Solid State Phenom.*, vol. 160, no. 1, pp. 39–46, 2010.

[117] A. J. Wilkinson and P. B. Hirsch, "Electron diffraction based techniques in scanning electron microscopy of bulk materials," *Micron*, vol. 28, no. 4, pp. 279–308, Aug. 1997.

[118] A. L. Marshall, J. Holzer, P. Stejskal, C. J. Stephens, T. Vystavěl, and M. J. Whiting, "The EBSD spatial resolution of a Timepix-based detector in a tilt-free geometry," *Ultramicroscopy*, vol. 226, no. March, pp. 11–13, 2021.

[119] J. J. F. B. Beausir, "ATEX- analysis tools for orientation maps, http://www.atex-software.eu/," *Univ. Lorraine - Metz*, p. 2015, 2015.

[120] D. G. Coates, “Kikuchi-like reflection patterns obtained with the scanning electron microscope,” *Philos. Mag.*, vol. 16, no. 144, pp. 1179–1184, 1967.

[121] G. R. Booker, A. M. B. Shaw, M. J. Whelan, and P. B. Hirsch, “Some comments on the interpretation of the ‘kikuchi-like reflection patterns’ observed by scanning electron microscopy,” *Philos. Mag.*, vol. 16, no. 144, pp. 1185–1191, 1967.

[122] R. M. Stern, T. Ichinokawa, S. Takashima, H. Hashimoto, and S. Kimoto, “Dislocation images in the high resolution scanning electron microscope,” *Philos. Mag.*, vol. 26, no. 6, pp. 1495–1499, 1972.

[123] D. R. Clarke, “Observation of crystal defects using the scanning electron microscope,” *Philos. Mag.*, vol. 24, no. 190, pp. 973–979, 1971.

[124] G. L’hôte *et al.*, “Rotational-Electron Channeling Contrast Imaging analysis of dislocation structure in fatigued copper single crystal,” *Scr. Mater.*, vol. 162, pp. 103–107, 2019.

[125] G. . Oliver, W.C.; Pharr, “An improved technique for determining hardness and elastic modulus using load and displacement sensing experiments,” *J. Mater. Res.*, vol. 7, no. 6, pp. 1564–1583, 1992.

[126] W. C. Oliver and G. M. Pharr, “Measurement of hardness and elastic modulus by instrumented indentation: Advances in understanding and refinements to methodology,” *Mater. Res. Soc.*, vol. 19, no. 1, 2004.

[127] D. Doerner, MF; Nix, W, “A method for interpreting the data from depth-sensing indentation instrunments,” *J. Mater. Res.*, vol. 1, no. 4, pp. 601–609, 1986.

[128] J. Woirgard and J. C. Dargenton, “An alternative method for penetration depth determination in nanoindentation measurements,” *J. Mater. Res.*, vol. 12, no. 9, pp. 2455–2458, 1997.

[129] M. V. Field, J.S. ; Swain, “A Simple Predictive Model for El Niño,” *J. Mater. Res.*, vol. 8, no. 2, pp. 297–306, 1993.

[130] P. Sudharshan Phani and W. C. Oliver, “Critical examination of experimental data on strain bursts (pop-in) during spherical indentation,” *J. Mater. Res.*, vol. 35, no. 8, pp. 1028–1036, 2020.

[131] L. Zhang and T. Ohmura, “Plasticity initiation and evolution during nanoindentation of an iron-3% silicon crystal,” *Phys. Rev. Lett.*, vol. 112, no. 14, pp. 1–5, 2014.

[132] A. Barnoush, “Correlation between dislocation density and nanomechanical response during nanoindentation,” *Acta Mater.*, vol. 60, no. 3, pp. 1268–1277, 2012.

[133] S. Shim, H. Bei, E. P. George, and G. M. Pharr, “A different type of indentation size effect,” *Scr. Mater.*, vol. 59, no. 10, pp. 1095–1098, 2008.

[134] T. H. Ahn, C. S. Oh, K. Lee, E. P. George, and H. N. Han, “Relationship between yield point phenomena and the nanoindentation pop-in behavior of steel,” *J. Mater. Res.*, vol. 27, no. 1, pp. 39–44, 2012.

[135] A. Barnoush, M. T. Welsch, and H. Vehoff, “Correlation between dislocation density and pop-in phenomena in aluminum studied by nanoindentation and electron channeling contrast imaging,” *Scr. Mater.*, vol. 63, no. 5, pp. 465–468, 2010.

[136] A. Montagne, V. Audurier, and C. Tromas, “Influence of pre-existing dislocations on the pop-in phenomenon during nanoindentation in MgO,” *Acta Mater.*, vol. 61, no. 13, pp. 4778–4786, 2013.

[137] A. Barnoush and H. Vehoff, “In situ electrochemical nanoindentation of a nickel (111) single crystal: hydrogen effect on pop-in behaviour,” *Zeitschrift fuer Met. Res. Adv. Tech.*, vol. 97, no. 9, pp. 1224–1229, 2006.

[138] K. Sekido, T. Ohmura, T. Hara, and K. Tsuzaki, “Effect of dislocation density on the initiation of plastic deformation on Fe-C steels,” *Mater. Trans.*, vol. 53, no. 5, pp. 907–912, 2012.

[139] F. Pöhl, “Pop-in behavior and elastic-to-plastic transition of polycrystalline pure iron during sharp nanoindentation,” *Sci. Rep.*, vol. 9, no. 1, pp. 1–12, 2019.

[140] N. Zhou, K. I. Elkhodary, X. Huang, S. Tang, and Y. Li, “Dislocation structure and dynamics govern pop-in modes of nanoindentation on single-crystal metals,” *Philos. Mag.*, vol. 100, no. 12, pp. 1585–1606, 2020.

[141] Y. Xia, Y. Gao, G. M. Pharr, and H. Bei, “Single versus successive pop-in modes in nanoindentation tests of single crystals,” *J. Mater. Res.*, vol. 31, no. 14, pp. 2065–2075, 2016.

[142] F. Javaid, H. Pouriayevali, and K. Durst, “Dislocation–grain boundary interactions: recent advances on the underlying mechanisms studied via nanoindentation testing,” *J. Mater. Res.*, no. 0123456789, 2021.

[143] F. Javaid, Y. Xu, and K. Durst, “Local analysis on dislocation structure and hardening

during grain boundary pop-ins in tungsten," *J. Mater. Sci.*, vol. 55, no. 22, pp. 9597–9607, 2020.

[144] S. Lu *et al.*, "Grain boundary effect on nanoindentation: A multiscale discrete dislocation dynamics model," *J. Mech. Phys. Solids*, vol. 126, pp. 117–135, 2019.

[145] T. Ohmura and K. Tsuzaki, "Plasticity initiation and subsequent deformation behavior in the vicinity of S Single grain boundary investigated through nanoindentation technique," *J. Mater. Sci.*, vol. 42, no. 5, pp. 1728–1732, 2007.

[146] C. Caër, E. Patoor, S. Berbenni, and J. S. Lecomte, "Stress induced pop-in and pop-out nanoindentation events in CuAlBe shape memory alloys," *Mater. Sci. Eng. A*, vol. 587, pp. 304–312, 2013.

[147] V. Brázdová and D. R. Bowler, *Atomistic Computer Simulations: A practical guide*. WILEY-VCHVerlag GmbH& Co. KGaA, Boschstr. 12, 69469 Weinheim, Germany, 2013.

[148] M. Griebel, S. Knapek, and G. Zumbusch, *Numerical Simulation in Molecular Dynamics: Numerics, Algorithms, Parallelization, Applications*. Springer Berlin Heidelberg, 2007.

[149] E. Polak and G. Ribiière, "Note Surla Convergence des methods de directions conjugate," *Rev. Fr. infr, Rech Oper.*, vol. 16, pp. 35–43, 1969.

[150] Y. Lee, J. Y. Park, S. Y. Kim, S. Jun, and S. Im, "Atomistic simulations of incipient plasticity under Al(1 1 1) nanoindentation," *Mech. Mater.*, vol. 37, no. 10, pp. 1035–1048, 2005.

[151] T. H. Fang, W. Y. Chang, and J. J. Huang, “Dynamic characteristics of nanoindentation using atomistic simulation,” *Acta Mater.*, vol. 57, no. 11, pp. 3341–3348, 2009.

[152] D. Hua *et al.*, “Atomistic insights into the deformation mechanism of a CoCrNi medium entropy alloy under nanoindentation,” *Int. J. Plast.*, vol. 142, no. April, p. 102997, 2021.

[153] J. D. Haile, *Molecular dynamics simulation, elementary methods*. John Wiley & sons, Inc, 1992.

[154] M. S. Daw and M. I. Baskes, “Embedded-atom method: Derivation and application to impurities, surfaces, and other defects in metals,” *Phys. Rev. B*, vol. 29, no. 12, pp. 6443–6453, 1984.

[155] Q. J. Li, H. Sheng, and E. Ma, “Strengthening in multi-principal element alloys with local-chemical-order roughened dislocation pathways,” *Nat. Commun.*, vol. 10, no. 1, pp. 1–11, 2019.

[156] D. Faken and H. Jónsson, “Systematic analysis of local atomic structure combined with 3D computer graphics,” *Comput. Mater. Sci.*, vol. 2, no. 2, pp. 279–286, 1994.

[157] J. D. H. . Honeycut, “On the application of Reynolds’ analogy and the heat-exchange factor to the design of heat exchangers II and III,” *J. Phys. Chem.*, vol. 91, no. 1, pp. 4950–4963, 1987.

[158] A. Stukowski, V. V. Bulatov, and A. Arsenlis, “Automated identification and indexing of dislocations in crystal interfaces,” *Model. Simul. Mater. Sci. Eng.*, vol. 20, no. 8, 2012.

[159] D. Lorenz, A. Zeckzer, U. Hilpert, P. Grau, H. Johansen, and H. S. Leipner, “Pop-in effect as homogeneous nucleation of dislocations during nanoindentation,” *Phys. Rev. B - Condens. Matter Mater. Phys.*, vol. 67, no. 17, pp. 1–4, 2003.

[160] A. M. Minor, E. T. Lilleodden, E. A. Stach, and J. W. Morris, “Direct observations of incipient plasticity during nanoindentation of Al,” *J. Mater. Res.*, vol. 19, no. 1, pp. 176–182, 2004.

[161] H. Bei, Y. F. Gao, S. Shim, E. P. George, and G. M. Pharr, “Strength differences arising from homogeneous versus heterogeneous dislocation nucleation,” *Phys. Rev. B - Condens. Matter Mater. Phys.*, vol. 77, no. 6, pp. 2–5, 2008.

[162] M. Bagheripoor and R. Klassen, “The effect of crystal anisotropy and pre-existing defects on the incipient plasticity of FCC single crystals during nanoindentation,” *Mech. Mater.*, vol. 143, no. September 2019, p. 103311, 2020.

[163] A. A. Zbib and D. F. Bahr, “Dislocation nucleation and source activation during nanoindentation yield points,” *Metall. Mater. Trans. A Phys. Metall. Mater. Sci.*, vol. 38 A, no. 13, pp. 2249–2255, 2007.

[164] Y. Wang, X. Xiong, and C. Zhu, “Dependence of pop-in behavior of a high-entropy alloy FeCoCrMnNi on tip radius,” *Appl. Phys. A Mater. Sci. Process.*, vol. 125, no. 2, p. 0, 2019.

[165] C. Zhu, Z. P. Lu, and T. G. Nieh, “Incipient plasticity and dislocation nucleation of FeCoCrNiMn high-entropy alloy,” *Acta Mater.*, vol. 61, no. 8, pp. 2993–3001, 2013.

[166] P. Hallensleben *et al.*, “On crystal mosaicity in single crystal Ni-based superalloys,”

Crystals, vol. 9, no. 3, pp. 15–20, 2019.

[167] F. Habiyaremye *et al.*, "A Plasticity induced by nanoindentation in a CrCoNi medium-entropy alloy studied by accurate electron channeling contrast imaging revealing dislocation-low angle grain boundary interactions," *Mater. Sci. Eng. A*, vol. 817, no. January, 2021.

[168] H. Kriaa, A. Guitton, and N. Maloufi, "Modelling Electron Channeling Contrast Intensity of Stacking Fault and Twin Boundary Using Crystal Thickness Effect," *Materials (Basel).*, vol. 14, no. 1696, pp. 1–10, 2021.

[169] W. W. Gerberich, J. C. Nelson, E. T. Lilleodden, P. Anderson, and J. T. Wyrobek, "Indentation induced dislocation nucleation: The initial yield point," *Acta Mater.*, vol. 44, no. 9, pp. 3585–3598, 1996.

[170] J. C. Crone, L. B. Munday, J. J. Ramsey, and J. Knap, "Modeling the effect of dislocation density on the strength statistics in nanoindentation," *Model. Simul. Mater. Sci. Eng.*, vol. 26, no. 1, 2018.

[171] T. A. Michalske and J. E. Houston, "Dislocation nucleation at nano-scale mechanical contacts," *Acta Mater.*, vol. 46, no. 2, pp. 391–396, 1998.

[172] Y. L. Chiu and A. H. W. Ngan, "Time-dependent characteristics of incipient plasticity in nanoindentation of a Ni3Al single crystal," *Acta Mater.*, vol. 50, no. 6, pp. 1599–1611, 2002.

[173] R. J. Wagner, L. Ma, F. Tavazza, and L. E. Levine, "Dislocation nucleation during nanoindentation of aluminum," *J. Appl. Phys.*, vol. 104, no. 11, 2008.

[174] T. Zhu, J. Li, A. Samanta, A. Leach, and K. Gall, “Temperature and strain-rate dependence of surface dislocation nucleation,” *Phys. Rev. Lett.*, vol. 100, no. 2, pp. 1–4, 2008.

[175] D. F. Bahr, S. L. Jennerjohn, and D. J. Morris, “Dislocation nucleation and multiplication in small volumes: The onset of plasticity during indentation testing,” *Jom*, vol. 61, no. 2, pp. 56–60, 2009.

[176] J. K. Mason, A. C. Lund, and C. A. Schuh, “Determining the activation energy and volume for the onset of plasticity during nanoindentation,” *Phys. Rev. B - Condens. Matter Mater. Phys.*, vol. 73, no. 5, pp. 1–14, 2006.

[177] S. P. Wang and J. Xu, “Incipient plasticity and activation volume of dislocation nucleation for TiZrNbTaMo high-entropy alloys characterized by nanoindentation,” *J. Mater. Sci. Technol.*, vol. 35, no. 5, pp. 812–816, 2019.

[178] M. A. Lodes, A. Hartmaier, M. Göken, and K. Durst, “Influence of dislocation density on the pop-in behavior and indentation size effect in CaF2 single crystals: Experiments and molecular dynamics simulations,” *Acta Mater.*, vol. 59, no. 11, pp. 4264–4273, 2011.

[179] M. D. Sangid, T. Ezaz, H. Sehitoglu, and I. M. Robertson, “Energy of slip transmission and nucleation at grain boundaries,” *Acta Mater.*, vol. 59, no. 1, pp. 283–296, 2011.

[180] P. Chowdhury, H. Sehitoglu, H. J. Maier, and R. Rateick, “Strength Prediction in NiCo Alloys - The Role of Composition and Nanotwins,” *Int. J. Plast.*, 2015.

[181] I. V. Kireeva, Y. I. Chumlyakov, Z. V. Pobedennaya, I. V. Kuksgausen, and I. Karaman,

"Orientation dependence of twinning in single crystalline CoCrFeMnNi high-entropy alloy," *Mater. Sci. Eng. A*, vol. 705, pp. 176–181, 2017.

[182] W. Z. Abuzaid, M. D. Sangid, J. D. Carroll, H. Sehitoglu, and J. Lambros, "Journal of the Mechanics and Physics of Solids Slip transfer and plastic strain accumulation across grain boundaries in Hastelloy X," *J. Mech. Phys. Solids*, vol. 60, no. 6, pp. 1201–1220, 2012.

[183] R. Kapoor and N. Verdhan, "Interaction of dislocation pile-up with a low-angle tilt boundary : a discrete dislocation dynamics study," *Philos. Mag.*, vol. 6435, no. December, pp. 1–24, 2016.

[184] Y. Gao and Z. Jin, "Interactions between lattice dislocation and Lomer -type low-angle grain boundary in nickel," *Comput. Mater. Sci.*, vol. 138, pp. 225–235, 2017.

[185] B. Liu, D. Raabe, P. Eisenlohr, F. Roters, A. Arsenlis, and G. Hommes, "Dislocation interactions and low-angle grain boundary strengthening," *Acta Mater.*, vol. 59, no. 19, pp. 7125–7134, 2011.

[186] N. Verdhan and R. Kapoor, "Interaction of dislocations with low angle tilt boundaries in fcc crystals," *Comput. Mater. Sci.*, vol. 98, pp. 149–157, 2015.

[187] B. Liu, P. Eisenlohr, F. Roters, and D. Raabe, "Simulation of dislocation penetration through a general low-angle grain boundary," *Acta Mater.*, vol. 60, no. 13–14, pp. 5380–5390, 2012.

[188] S. Kondo, T. Mitsuma, N. Shibata, and Y. Ikuhara, "Direct observation of individual dislocation interaction processes with grain boundaries," *Sci. Adv.*, vol. 2, no. 11, pp. 1–

8, 2016.

[189] T. Ohmura, A. M. Minor, E. A. Stach, and J. W. Morris, “Dislocation-grain boundary interactions in martensitic steel observed through in situ nanoindentation in a transmission electron microscope,” *J. Mater. Res.*, vol. 19, no. 12, pp. 3626–3632, 2004.

[190] Y. M. Soifer, A. Verdyan, M. Kazakevich, and E. Rabkin, “Nanohardness of copper in the vicinity of grain boundaries,” *Scr. Mater.*, vol. 47, no. 12, pp. 799–804, 2002.

[191] W. A. Soer, J. T. M. De Hosson, A. M. Minor, J. W. Morris, and E. A. Stach, “Effects of solute Mg on grain boundary and dislocation dynamics during nanoindentation of Al-Mg thin films,” *Acta Mater.*, vol. 52, no. 20, pp. 5783–5790, 2004.

[192] M. G. Wang and A. H. W. Ngan, “Indentation strain burst phenomenon induced by grain boundaries in niobium,” *J. Mater. Res.*, vol. 19, no. 8, pp. 2478–2486, 2004.

[193] A. Gouldstone, H. J. Koh, K. Y. Zeng, A. E. Giannakopoulos, and S. Suresh, “Discrete and continuous deformation during nanoindentation of thin films,” *Acta Mater.*, vol. 48, no. 9, pp. 2277–2295, 2000.

[194] J. T. M. De Hosson *et al.*, “In situ TEM nanoindentation and dislocation-grain boundary interactions: a tribute to David Brandon,” *J. Mater. Sci.*, vol. 41, no. 23, pp. 7704–7719, 2006.

[195] B. Yang and H. Vehoff, “Dependence of nanohardness upon indentation size and grain size - A local examination of the interaction between dislocations and grain boundaries,” *Acta Mater.*, vol. 55, no. 3, pp. 849–856, 2007.

[196] Y. T. Zhu, X. L. Wu, X. Z. Liao, J. Narayan, L. J. Kecskés, and S. N. Mathaudhu, "Dislocation-twin interactions in nanocrystalline fcc metals," *Acta Mater.*, vol. 59, no. 2, pp. 812–821, 2011.

[197] J. Wang, "Atomistic Simulations of Dislocation Pileup : Grain Boundaries Interaction," *JOM*, vol. 67, no. 7, pp. 1515–1525, 2015.

[198] P. Hirel, "Atomsk: A tool for manipulating and converting atomic data files," *Comput. Phys. Commun.*, vol. 197, pp. 212–219, 2015.

[199] A. Movahedi-Rad *et al.*, "Grain Boundary Migration in Metals: Thermodynamics, Kinetics, Applications," *Phys. Rev.*, vol. 05, no. 8, p. 275, 2014.

[200] Q. J. Li, H. Sheng, and E. Ma, "Strengthening in multi-principal element alloys with local-chemical-order roughened dislocation pathways," *Nat. Commun.*, vol. 10, no. 1, pp. 1–31, 2019.